Out-of-Field Dose in Photon Radiotherapy: Models and Measurements

Dissertation
zur
Erlangung der naturwissenschaftlichen Doktorwürde
(Dr. sc. nat.)
vorgelegt der
Mathematisch-naturwissenschaftlichen Fakultät
der
Universität Zürich

von

Pascal Hauri

aus
Hirschthal (AG)

Promotionskommission
Prof. Dr. Uwe Schneider (Vorsitz und Leitung der Dissertation)
Prof. Dr. Jürg Osterwalder
Prof. Dr. Antony John Lomax

Zürich, 2017

Contents

Background and motivation

The intention of radiotherapy is to control and cure local diseases while avoiding late effects caused by radiation. Over the past decades, new treatment modalities have been introduced to deliver the dose in a more conformal manner to the tumor by simultaneously sparing organs at risk which are in close proximity to the target volume. By sparing organs at risk, deterministic effects like acute normal tissue toxicity can be avoided. However, these new treatment modalities were not developed to reduce stochastic effects like induction of second primary cancers. Minimizing these stochastic effects remains challenging in daily clinical practice since the out-of-field dose for an individual patient is not known. This has mainly two reasons: (1) The treatment planning system (TPS) which is used in external beam therapy to generate dose distributions, does not correctly calculate the dose outside the primary beam. (2) Dose measurements of photons, electrons, and neutrons are challenging, especially in the out-of-field region. This thesis deals with the assessment of the individual patient whole-body dose for cancer treatments.

The dose in the treated volume is accurately predicted by the TPS. Furthermore, the estimation of the non-target dose by the TPS for intermediate doses ($>$ 3-30 Gy or $>$ 5-50 % of the prescribed dose) shows an accuracy which is acceptable for risk assessment, compared with measurements. However, for low doses ($<$ 3 Gy or $<$ 5 % of the prescribed dose), the dose is underestimated by orders of magnitude or not calculated at all by commercial TPSs. In chapter 1, a general model is introduced, which calculates the dose distribution outside the treatment volume for 3D-conformal and intensity-modulated treatments. The model utilizes a nominal beam energy of 6 MV to describe two linear accelerator types of one vendor. The out-of-field dose is fused with the TPS-calculated dose, resulting a whole-body dose.

Photon dose measurements outside the primary beam are challenging because the dose is orders of magnitudes lower compared to the dose in the treated volume. Furthermore, the photon energy spectrum changes in the out-of-field region, which can affect the measurement. Lithium fluoride (LiF) thermoluminescence dosimeters (TLDs) are well-suited for out-of-field dose measurements in the patient since they have a small size, a high sensitivity to ionizing radiation, and a tissue-equivalent composition. However, the response of the TLDs with radiation energy leads to a systematic error in dose for off-axis measurements. In chapter 2, we propose a double-TLD unit which automatically corrects for the response of the TLDs with radiation energy by determining the mean energy of the photon spectrum. The double-TLD unit consists of two differently doped LiF TLDs which show different responses with radiation energy. The accuracy in the out-of-field dose and energy measurement of the double-TLD unit is discussed in detail in chapter 2.

With novel treatment techniques, the patient is usually positioned by using imaging. This practice is called image-guided radiation therapy (IGRT). One main advantage of using IGRT is the reduction of the uncertainty margins for the treated volume. This reduces the non-target dose in close proximity to the tumor. However, outside the primary beam, X-ray imaging in IGRT can give a substantial unwanted dose to the patient. Cone beam computer tomography (CBCT) is one of the most frequently used imaging modality for IGRT. For CBCT, different protocols are available to image the patient. Some protocols are considered to reduce the patient exposure at cost of a smaller field-of-view and reduced contrast. In chapter 3, we investigate the dose of two different CBCT protocols applied with the on-board imager mounted on a linear accelerator. The whole-body dose and mean energy are measured for both protocols using the double-TLD unit introduced in chapter 2.

One way to avoid patient exposure caused by imaging is to use non-ionizing modalities like magnetic resonance imaging (MRI). However, the combination of a linear accelerator and an MRI device causes problems since the magnetic field interferes with the accelerated electrons. For a conventional linear accelerator, the primary X-ray beam is produced by deceleration of electrons in a high-Z containing target which is located in the gantry head. A possible solution is to combine a Cobalt machine and an MRI device, since the magnetic field does not interfere with the radioactive decay of $^{60}\mathbf{Co}$. However, Cobalt machines are known to be inferior compared to 6 MV linear accelerators in the peripheral region. In appendix A, the out-of-field dose of an MRI-guided Cobalt treatment is compared to conventional IGRT treatments which use CBCT for patient positioning. The whole-body dose and energy are measured for the IGRT treatments using the double-TLD unit presented in chapter 2.

For deep-seated solid cancers, high nominal X-ray energies ($\geq 10\,\mathrm{MV}$) are needed to achieve a conformal dose to the treated volume. These high energy photons produce secondary particles like photoneutrons, which are an additional source to the out-of-field dose. Neutrons have an increased probability of stochastic radiation effects compared to photons. The beam-on time for high energy treatments is usually shorter compared to low energy treatments. Hence, a reduction in the out-of-field dose can be expected. Furthermore, photons which are interacting in the patient are more forward-scattered for high energy beams compared to the low energy beams. This reduces the out-of-field dose even further for high compared to low nominal X-ray energy treatments. However, this comes with the cost of photoneutron production. In chapter 4, the total whole-body doses of 6 MV and 15 MV IGRT treatments are compared. To accesses the photoneutron dose in the patient, a simple neutron model is developed. The general model for photon stray dose calculation of 6 MV introduced in chapter 1 is improved and, furthermore, adapted for 15 MV nominal X-ray energy. The model predictions are compared to independent TLD measurements. For this, a new method to measure the photoneutron dose for linear accelerators is presented. To measure the photon dose, the TLDs are corrected for the response with radiation energy by calculating the mean photon energy for every off-axis point in the patient. The whole-body dose is discussed in detail to understand the importance of the scatter contributions in IGRT regarding patient protection.

Chapter 1

A general model for stray dose calculation of static and intensity-modulated photon radiation

Pascal Hauri[1,2], Roger A. Hälg[1,2], Jürgen Besserer[1], and Uwe Schneider[1,2]

[1] Institute for Radiotherapy, Radiotherapie Hirslanden AG, Aarau, Switzerland

[2] Department of Physics, University of Zurich, Zurich, Switzerland

This chapter was adapted from the original article:

“A general model for stray dose calculation of static and intensity-modulated photon radiation”

Published in:

Medical Physics 2016, **43(4)**, 1995–1968
doi:10.1118/1.4944421.

Purpose: There is an increasing number of cancer survivors who are at risk of developing late effects caused by ionizing radiation such as induction of second tumors. Hence, the determination of out-of-field dose for a particular treatment plan in the patient's anatomy is of great importance. The purpose of this study was to analytically model the stray dose according to its three major components.

Methods: For patient scatter, a mechanistic model was developed. For collimator scatter and head leakage, an empirical approach was used. The models utilize a nominal beam energy of 6 MV to describe two linear accelerator types of a single vendor. The parameters of the models were adjusted using ionization chamber measurements registering total absorbed dose in simple geometries. Whole-body dose measurements using thermoluminescent dosimeters in an anthropomorphic phantom for static and intensity-modulated treatment plans were compared to the 3D out-of-field dose distributions calculated by a combined model.

Results: The absolute mean difference between the whole-body predicted and the measured out-of-field dose of four different plans was 11 % with a maximum difference below 44 %. Computation time of $36'000$ dose points for one field was around 30 s. By combining the model-calculated stray dose with the treatment planning system dose, the whole-body dose distribution can be viewed in the treatment planning system.

Conclusion: The results suggest that the model is accurate, fast, and can be used for a wide range of treatment modalities to calculate the whole-body dose distribution for clinical analysis. For similar energy spectra, the mechanistic patient scatter model can be used independently of treatment machine or beam orientation.

Keywords: 3D Out-of-Field Dose Distribution, Analytical Stray Dose Model, Mechanistic Patient Scatter Model, IMRT, VMAT

I. INTRODUCTION

The intention of radiation therapy (RT) is to control or cure local diseases while avoiding acute and minimizing late effects caused by radiation. With steadily improving mega-electron volt (MeV) beam modalities [intensity-modulated radiation therapy (IMRT) and volumetric modulated arc therapy (VMAT)], more conformal dose distributions and increased cancer cure rates can be achieved [1]. Hence, there is an increasing number of long-term survivors who are at risk of late effects, such as second cancers [2]. As a consequence, it is important to model the out-of-field dose not only for open static fields [e.g. 3D conformal radiation therapy (3DCRT)] as it has been described by several authors [3–10], but also for treatment plans applying intensity modulation.

Several treatment planning systems (TPSs) have been investigated with regard to out-of-field dose estimation, for instance, the Varian (Eclipse) TPS (Varian, Palo Alto, CA, USA) [11] or the Tomotherapy (TomoTherapy) and CyberKnife (MultiPlan) TPSs from Accuray (Accuray, Sunnyvale, CA, USA) [12]. These studies claim that the stray dose is underestimated by orders of magnitude by the TPS exceeding a certain distance to the field edge. Hence, out-of-field dose predicted from commercial TPS should not be used for modeling second cancer induction [12].

Many scientists have studied analytical models or Monte Carlo (MC) simulations to predict out-of-field dose [3–10, 13, 14]. Taddei et al. [13] presented an empirical double Gaussian model which was optimized with and compared to measurements in an anthropomorphic phantom using thermoluminescent dosimeters (TLDs). MC simulations for static open fields in simple geometries were done by Kry et al. [3], as well as Bednarz and Xu [10] and in an anthropomorphic phantom for IMRT plans by Kry et al. [14]. An analytical method to calculate the in- and out-of-field dose was introduced by Jagetic an Newhauser [9]. This model was tested with promising results in simple geometries for open fields, but is not yet suitable for IMRT. In addition, patient scatter, representing the major component of the stray dose close to the field edge [5, 9, 15–17], was not mechanistically modeled. To our knowledge, there is no analytical model available to predict stray dose in patients for IMRT or VMAT plans.

The aim of this work was to provide an analytical model to predict the stray dose of different treatment techniques (3DCRT, IMRT, and VMAT) for commercial linear accelerators of one vendor (Varian). The calculated 3D out-of-field dose distribution for a nominal beam energy of 6 MV can be reimported into the TPS for further analysis. The model's stray dose calculation is based on treatment plans and organ structures exported from the TPS following the digital imaging and communications in medicine (DICOM) standard.

The stray dose can be separated into its three major components: patient scatter, head leakage, and collimator scatter [15]. As mentioned before, internal patient scatter is the unavoidable main component of the peripheral dose in photon-beam radiation therapy [5, 9, 15–17]. Diallo et al. [18] found that only nine out of 115 second cancers are located more than 20 cm away from the closest beam. Several authors suggested empirical models for internal scatter [6–9, 13]. However, there is a lack of physics-based models for patient scatter.

In this work, we introduce a highly adaptive mechanistic model for patient scatter which only needs four physics-motivated fit parameters to predict the absolute absorbed out-of-field dose at any point in the patient for a broad range of field sizes and various body proportions. For collimator scatter and head leakage, simple empirical models were introduced. Absolute absorbed dose was measured outside the primary beam for simple geometries and the three stray dose contributions were separated. The parameters of each model were trained separately. The head leakage, collimator, and patient scatter model predictions were tested for real treatment plans in simple geometries. Furthermore, the model-calculated out-of-field dose was compared to previous whole-body measurements in an anthropomorphic phantom using TLDs for three modalities (3DCRT, IMRT, and VMAT) [19].

II. METHODS AND MATERIALS

A. Analytical model for estimation of the out-of-field dose

According to Ruben et al. [15], the total absorbed dose D_{total} outside the radiation field can be described as the sum of three different contributions. $D_{patient}$ is the dose mainly produced by Compton scatter of the primary photon field inside the patient. $D_{collimator}$ is caused by scattering of the primary beam in the gantry head. $D_{leakage}$ is the absorbed dose of photons leaking through the gantry head shielding originating from the target,

$$D_{total} = D_{patient} + D_{collimator} + D_{leakage}. \tag{1}$$

Due to the origin of patient scatter, it is modeled as a function of distance to the field edge z_{edge}. Collimator scatter and head leakage are empirically modeled as a function to the isocenter z_{iso}.

1. Internal patient scatter

For the dose calculations, it is assumed that the source of patient scatter is a disk (in the x, y plane) with radius R_{iso} consisting of infinitely small sources, each of strength d (see Fig. 1). The dose (D) at a distance Z along a line perpendicular to the disc can be calculated analytically. The contribution from an infinitely small source in a medium is attenuated exponentially and is decreasing by the inverse of the distance squared. In polar coordinates this leads to the following integral:

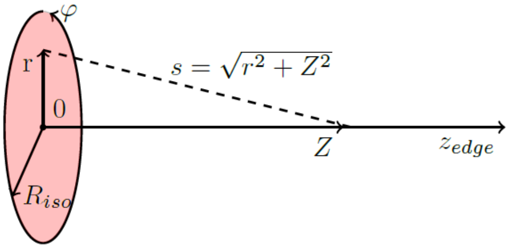

FIG. 1. Sketch of a disk consisting of infinitely small sources of strength d.

$$\begin{aligned}\mathrm{D}(Z) = d \cdot \int_0^{2\pi}\int_0^{R_{iso}} |r| \cdot \frac{\exp(-\mu(E_{patient}) \cdot s)}{s^2} \mathrm{d}r\mathrm{d}\varphi = \\ d \cdot \int_0^{2\pi} \Big\{\mathrm{Ei}\Big(\mu(E_{patient}) \cdot Z\Big) - \mathrm{Ei}\Big(\mu(E_{patient}) \cdot \sqrt{Z^2 + R_{iso}^2}\Big)\Big\}\mathrm{d}\varphi = \\ 2\pi d\Big\{\mathrm{Ei}\Big(\mu(E_{patient}) \cdot Z\Big) - \mathrm{Ei}\Big(\mu(E_{patient}) \cdot \sqrt{Z^2 + R_{iso}^2}\Big)\Big\},\end{aligned} \tag{2}$$

where Ei is the exponential integral function, $\mu(E_{patient})$ the attenuation coefficient of the intermediate medium for the energy $E_{patient}$, and s is the path of the photons through this medium. Note that the integrand is independent of the angle. In reality, radiation fields of finite size are used and as a consequence, the scatter from this disk extends in the negative z-direction (see Fig. 2). To our knowledge, the integration over a cylindrical volume cannot be performed analytically. Therefore, we approximated the integral along the z-direction through a summation,

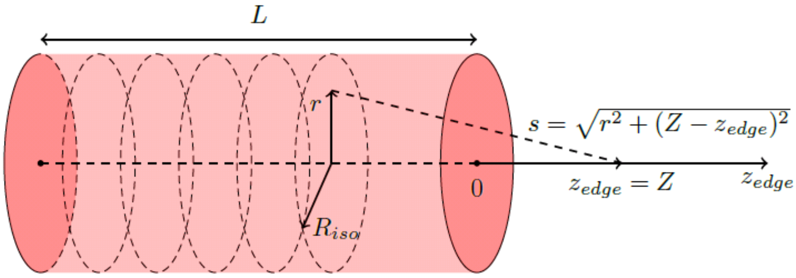

FIG. 2. Sketch of a cylinder consisting of infinitely small sources of strength d.

$$\begin{aligned} \mathrm{D}(Z) = d \cdot \int\limits_{-L}^{0} \int\limits_{0}^{2\pi} \int\limits_{0}^{R_{iso}} |r| \cdot \frac{\exp(-\mu(E_{patient}) \cdot s)}{s^2} \mathrm{d}r \mathrm{d}\varphi \mathrm{d}z_{edge} \approx \\ d \sum_{z'_{edge}=0}^{L} 2\pi \Big\{ \mathrm{Ei}\Big(\mu(E_{patient}) \cdot (Z + z'_{edge})\Big) - \mathrm{Ei}\Big(\mu(E_{patient}) \cdot \sqrt{(Z + z'_{edge})^2 + R_{iso}^2}\Big) \Big\}, \end{aligned} \tag{3}$$

where Z and L are the distance to and the length of the cylinder, respectively.
This model can be applied to a radiation therapy patient by assuming that the irradiated volume is in first approximation a part of a cylindrical volume. In this work, the irradiated volume represents the part of the body volume which is penetrated by the primary field. Furthermore, it is assumed that patient scatter is produced in this irradiated volume with isotropic scattering angles between 0° and 90°. Hence, if a static open field is being applied to the cylinder, the irradiated volume can be approximated by a sector of a cylinder (see Fig. 3).

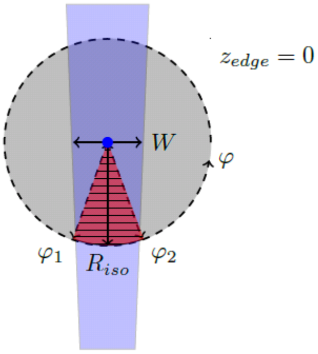

FIG. 3. Application of a static open field onto a cylinder. The patterned area represents the theoretical scatter volume which contributes to patient scatter.

For this irradiated volume, the radius R_{iso} and the length L remain the same but the limits for the angle integration dφ have to be adjusted. These integration limits scale with the field width W as can be seen in Fig. 3. Hence, we can define a function F_p which accounts for the relative change in the out-of-field dose contribution,

$$\mathrm{F}_p(\frac{W}{W_0}) \propto \int\limits_{\varphi(W)} \mathrm{d}\varphi, \tag{4}$$

where W_0 is a reference field width. By fitting F_p (Eq. 4) to experimental data, the patient scatter is modeled including the influence of the scatter from the irradiated volume lying outside the cylinder sector (see Fig. 3).
The energy spectrum of a typical radiation therapy accelerator peaks around 1.5 MeV for a 6 MV nominal beam energy [3]. In the energy range of interest, the Klein-Nishina formula [20] for Compton scattering predicts more forward than back scattering. Hence, in a realistic model, it must be distinguished between these two contributions. Therefore, $\mathrm{R}(x, y, \theta)$ of any coplanar field is defined as the distance from the field entrance to a point in the patient $P(x, y, z_{edge})$, projected on the central-beam-axis (CAX) (see Fig. 4).

To account for the smaller back scatter contribution, the length of the distal part of the irradiated volume $R_b = R_d - \mathrm{R}$ is

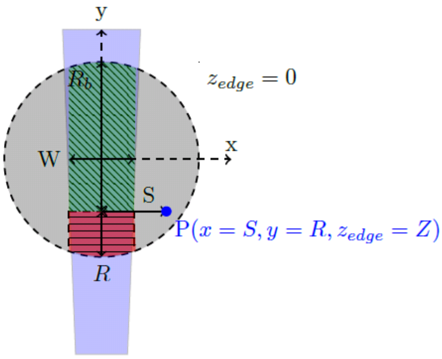

FIG. 4. Application of a static open field onto a cylinder. The horizontal and oblique patterned areas represent forward and back scatter contributions to the patient scatter dose for a point in the patient $P(x, y, z_{edge})$ (lying above the plane), respectively.

scaled by a factor $C_B(E_{field}) \leq 1.0$ and added to R. R_d is the diameter of the patient along the CAX. R is a function of the coordinates (x, y) and the gantry angle θ, as can be seen in Fig. 5. In this paper, $R(x = X_{iso}, y = Y_{iso}, \theta) = R_{iso}(\theta)$ indicates that the projection on to the CAX, lies in the isocenter.

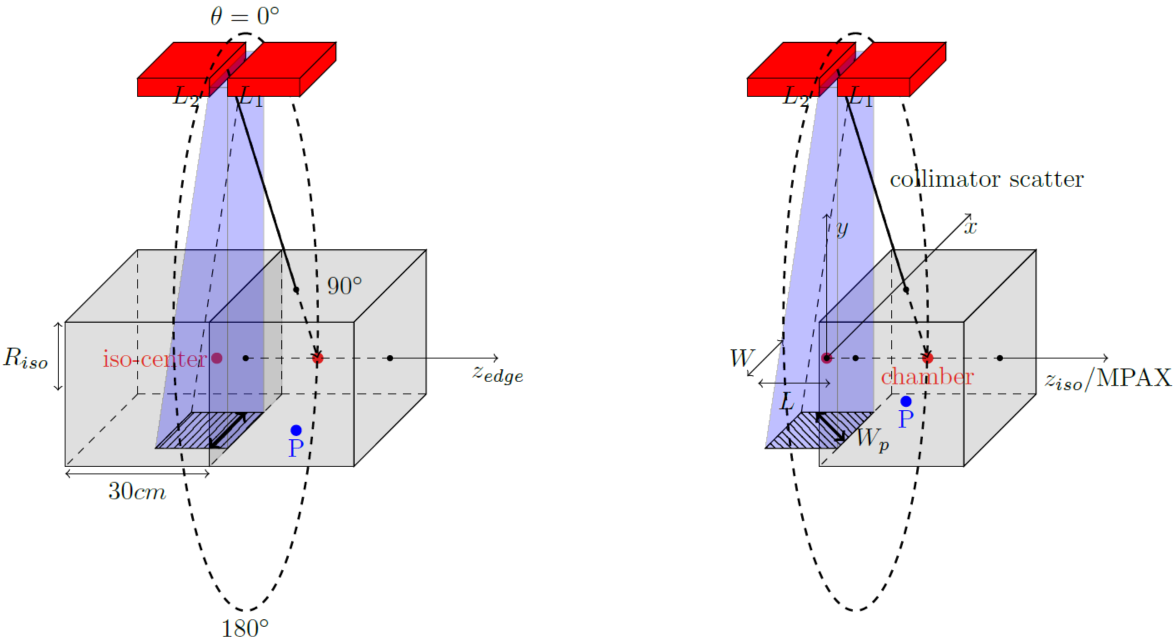

FIG. 5. Sketch of the set up to measure the patient scatter dose. The fields were designed such that they coincide with the phantom's edge and can be rotated 360°. On the right it is shown with a RW3-slab-phantom scatterer and on the left without. z_{edge} and z_{iso}/MPAX correspond to the coordinate system for patient and machine scatter, respectively. The patterns at the bottom of the left phantom represent the perceived field widths (W_p in Eq. 8) for no lateral displacement, corresponding to the point $P(x = 0, y = -R, z_{edge} = Z)$. On the right side W_p, it is shown for a lateral displacement S [$P(x = S, y = -R, z_{edge} = Z)$]

.

The photon fluence ϕ of a divergent radiation field penetrating a patient is proportional to

$$\phi \propto \exp\{-l_{depth} \cdot \mu(\mathrm{E_{field}})\}/l_{source}^2, \tag{5}$$

where $\mu(E_{field})$ is the attenuation coefficient, l_{depth} is the depth in the patient along the CAX, and l_{source} is the distance to the radiation source. It is assumed here that the magnitude of patient scatter for a point in the body with a projection R is proportional to the fluence at a depth of $\frac{1}{2}$R. Therefore, the change of the normalized fluence relative to the isocenter $H(x, y, E_{field}, \theta)$ reads,

$$H(x,y,E_{field},\theta) = \exp\big\{-\tfrac{1}{2}\big(\mathrm{R}(x,y,\theta)-\mathrm{R}_{\mathrm{iso}}(\theta)\big)\mu(E_{field})\big\}\Big(\frac{SSD+\frac{1}{2}\mathrm{R}_{\mathrm{iso}}(\theta)}{SSD+\frac{1}{2}\mathrm{R}(x,y,\theta)}\Big)^2, \tag{6}$$

where SSD is the source surface distance. The attenuation coefficient $\mu(E_{field})$ for the energy of the primary field was taken from published data [21].

The model of the out-of-field patient scatter was normalized at a distance Z_0 from the field edge. The normalization conditions were an isocenter dose of 1 Gy at a depth $R_{iso} = R_0$, a field length L_0, a field width W_0, and a field energy E_{field}. The normalization constant $\mathrm{C_N}(E_{field})$ has the dimension of mGy per treatment Gy. Consequently, patient scatter is proportional to the isocenter dose D_{iso} of the applied field.

The normalization constant $\mathrm{C_N}(E_{field})$ multiplied by the relative fluence change $H(x,y,E_{field},\theta)$ replaces the source strength d of equation (Eq. 3), as to our knowledge the equation is not solvable with variable source strength. Hence, internal scatter for every point in the patient is scaled by its corresponding source strength $\mathrm{d}(x,y,E_{field},\theta)$:

$$\mathrm{d}(x,y,E_{field},\theta) = \mathrm{C_N}(E_{field})\cdot H(x,y,E_{field},\theta). \tag{7}$$

An advantage of the summation instead of an integration along the field length (Eq. 3) is the ability to model changing widths along the field length by including Eq. 4 into the summation over L. For a rectangular field, the perceived width $\mathrm{W_p}$ of a point with a lateral displacement $S(X,Y,\theta)$ proximal to the CAX and z_{edge}-axis changes as indicated in Fig. 5. The distance to a field slice with $\mathrm{W_p}(W,L,Z,S,z'_{edge})$ is calculated by $\sqrt{(Z+z'_{edge})^2+S^2}$.

If all above mentioned changes are applied to Eq. 3, the final form of the patient scatter out-of-field dose $\mathrm{D_{patient}}$ for a point $\mathrm{P}(x=X, y=Y, z_{edge}=Z)$ in the body reads,

$$\begin{aligned}\mathrm{D_{patient}}(W,L,X,Y,Z,E_{field},\theta,D_{iso}) &= D_{iso}\cdot \mathrm{d}(X,Y,E_{field},\theta)\cdot\\ \sum_{z'_{edge}=0}^{L}\mathrm{F_p}\Big(\frac{\mathrm{W_p}(W,L,X,Y,Z,\theta,z'_{edge})}{W_0},E_{field}\Big)&\Bigg\{\mathrm{Ei}\Bigg(\mu\{\mathrm{E_{patient}}(E_{field})\}\sqrt{(Z+z'_{edge})^2+\mathrm{S}(X,Y,\theta)^2}\Bigg)-\\ \mathrm{Ei}\Bigg(\mu\{\mathrm{E_{patient}}(E_{field})\}&\sqrt{(Z+z'_{edge})^2+\mathrm{S}(X,Y,\theta)^2+\Big(\mathrm{R}(X,Y,\theta)+\{\mathrm{R_d}(\theta)-\mathrm{R}(X,Y,\theta)\}\mathrm{C_B}(E_{field})\Big)^2}\Bigg)\Bigg\},\end{aligned} \tag{8}$$

$$\mathrm{F_p}\Big(\frac{\mathrm{W_p}(W,L,X,Y,Z,\theta,z'_{edge})}{W_0},E_{field}\Big) = (\frac{W_p}{W_0})^{\mathrm{C_W}(E_{field})}, W_0 = 100\,\mathrm{mm}, \tag{9}$$

where the field energy dependent exponent $\mathrm{C_W}$ governs how strongly the patient scatter dose varies with changes in field width. Although the Compton scatter photons correspond to various energies, $\mu(E_{patient})$ is assumed to be constant.

The three constants $\mathrm{C_N}(E_{field})$, $\mu\{\mathrm{E_{patient}}(E_{field})\}$, and $\mathrm{C_B}(E_{field})$ as well as the function $\mathrm{F}_p(\frac{W_p}{W_0},E_{field})$ are determined from experiments (see Section II B 1). To apply the model to a real patient, assumptions have to be made for IMRT and VMAT plans concerning field width and length. These assumptions are explained in Section II C.

2. *External collimator scatter and head leakage*

A variety of literature can be found for describing machine scatter [6–9] including sophisticated models, as for example the multi-plane source model from Benadjaoud et al. [6]. By focusing on linear accelerators of one manufacturer, it is possible to use simple functions describing machine scatter, which is assumed to be proportional to the number of applied MUs. Collimator scatter and head leakage along the medial-patient-axis (MPAX, see Fig. 5) can be described each by a function $\mathrm{G}(z_{iso})$. z_{iso} is the distance from the isocenter to the point of calculation. Furthermore, it is assumed that the magnitude of collimator scatter and head leakage in vacuum does not change in a transaxial plane perpendicular to the MPAX. Collimator scatter shows a field size dependence [6] and the source is assumed to be located at the rear L-jaw (L_2 in Fig. 5),

$$\begin{aligned}\mathrm{D_{collimator}}(W,L,W_{mlc},x,y,z_{iso},E_{field},\theta,MUs) &=\\ MUs\cdot\{\mathrm{F_c}(W,L,W_{mlc},E_{field})\cdot\mathrm{G_{collimator}}(z_{iso},E_{field})\}&\mathrm{e}^{-\mathrm{l_{collimator}}(x,y,z_{iso},\theta)\cdot\mu(\mathrm{E_{collimator}}(E_{field}))},\end{aligned} \tag{10}$$

$$\mathrm{F_c}(W,L,W_{mlc}) = \frac{W}{W_G}\cdot\frac{L}{L_G}\cdot(C_1+C_2\cdot\frac{W_{mlc}}{W}), \tag{11}$$

$$\mathrm{G}_{\mathrm{collimator}}(z_{iso}) = C_3 \cdot z_{iso}^{C_4} \cdot \{1 + C_5 \cdot \exp(-(\frac{z_{iso} - C_6}{C_7})^2)\}. \tag{12}$$

Leakage is field size independent [6] and the source is assumed to be at the target location where the primary beam is produced [5, 9]:

$$\mathrm{D}_{\mathrm{leakage}}(x, y, z_{iso}, E_{field}, \theta, MUs) = 100 \cdot \{\mathrm{G}_{\mathrm{leakage}}(z_{iso}, E_{field})\} \mathrm{e}^{-\mathrm{l}_{\mathrm{leakage}}(x,y,z_{iso},\theta) \cdot \mu(\mathrm{E}_{\mathrm{leakage}}(E_{field}))}, \tag{13}$$

$$\mathrm{G}_{leakage}(z_{iso}) = C_8 + C_9 \cdot z_{iso}, \tag{14}$$

where W_{mlc} is the field width defined by the MLC settings and MUs correspond to the applied monitor units. $\mathrm{G}_{\mathrm{collimator/leakage}}(z_{iso})$ were obtained from experiments for a 6 MV nominal beam energy and have the dimensions of mGy/100 MUs. $\mathrm{F}_{\mathrm{c}}(W, L, W_{mlc})$ is dimensionless and accounts for the field size and the width of the MLC opening. W_G and L_G represent the field size at which $\mathrm{G}_{\mathrm{collimator}}(z_{iso})$ was determined. $\mathrm{l}_{\mathrm{collimator}}(x, y, z_{iso}, \theta)$ and $\mathrm{l}_{\mathrm{leakage}}(x, y, z_{iso}, \theta)$ are the trajectories through a medium (e.g. patient) with attenuation coefficient $\mu(E_{collimator})$ and $\mu(E_{leakage})$, respectively (see Fig. 5). The exponential decrease accounts for the attenuation in the patient. For a certain nominal beam energy, $\mu(E_{collimator})$ and $\mu(E_{leakage})$ are assumed to be constant. The beam energy dependent constants C_1-C_9, $\mu(E_{collimator})$ and $\mu(E_{leakage})$ are experimentally determined in Section II B 2.

B. Measurements to determine the model parameters

All measurements were performed using Varian (Varian Medical Systems, Palo Alto, CA, USA) linear accelerator models Clinac iX and TrueBeam for a nominal beam energy of 6 MV. The out-of-field dose was determined with a Farmer Chamber 30013 or a Rigid Stem Chamber 30016 from PTW (PTW, Freiburg, Germany). For measurements in air, the Farmer chamber was used with a build-up cap. Both chambers were placed such that self attenuation caused by the chambers themselves was minimized. Absolute out-of-field dose measurements were normalized to in-field reference measurements.

1. *Measurements of patient scatter*

To experimentally determine the three constants C_N, C_B, and $\mu(E_{patient})$, as well as the function F_p, doses from different field sizes (MLC retracted) were measured with (D_{total}) and without ($D_{machine}$) scatterer. By subtracting the machine scatter from the total scatter, patient scatter could be determined (see Eq. 1). Used as a scatterer, the water-equivalent RW3 slab-phantom (PTW) was combined with a second phantom (slab-phantom or $30 \times 30 \times 30\,\mathrm{cm}^3$ water bath). The primary beam was adjusted ($L_1 = 0$, see Fig. 5) such that it coincided with the border of the second phantom (divergent-free). Hence, fields from various gantry angles could be applied (Fig. 5). Unless otherwise stated, an isocenter dose of 2 Gy was applied.

To experimentally determine F_p (Eq. 4), patient scatter of 4-field plans (0°, 90°, 180°, 270°) consisting of fields with a length (L) of 10 cm and a width (W) reaching from 5 to 20 cm were measured at ($x = X_{iso}, y = Y_{iso}, z_{edge} = 15\,\mathrm{cm}$) (see Fig. 5). A change in the distance parallel to the CAX (R-value) leads to a change in the integration limits for $\mathrm{d}\varphi$, as can be seen in Fig. 3. Hence, the field width dependence F_p will change with R. However, the measurements were done in a $30 \times 30 \times 60\,\mathrm{cm}^3$ RW3-phantom parallel to the CAX at a depth of 15 cm ($\mathrm{R}_{\mathrm{iso}}$-value) and normalized to a field width of $W_0 = 10\,\mathrm{cm}$.

To find the attenuation coefficient $\mu(E_{patient})$, a $20 \times 30 \times 30\,\mathrm{cm}^3$ scatterer was combined with a water phantom. Three fields with dimensions of 5×5, 10×10, and $20 \times 20\,\mathrm{cm}^2$ were applied each with gantry angles 90 and 270°. From 10 to 60 cm along the z_{edge}-axis, the absorbed dose was measured in steps of 5 cm. To measure the dose from 35 to 60 cm, a $30 \times 30 \times 30\,\mathrm{cm}^3$ RW3-phantom was inserted between the scatterer and the water phantom. For the same set up, fields with a width of 10 cm and lengths from 2 up to 20 cm were measured 30 cm away from the field edge. The measurements for various field lengths were preformed to verify the predicted L-dependence of the model (Eq. 8).

To determine C_N, a $10 \times 10\,\mathrm{cm}^2$ field ($W_0 = 10$ and $L_0 = 10\,\mathrm{cm}$) with isocenter dose of 1 Gy was irradiated at gantry angle 0° impinging on a $30 \times 30 \times 60\,\mathrm{cm}^3$ RW3-phantom. The dose was registered at ($x = X_{iso}, y = Y_{iso}, z_{edge} = Z_0 = 15\,\mathrm{cm}$) resulting in an $R_{iso} = R_0$ value of 15 cm.

The dependence of patient scatter on a displacement proximal to the CAX and z_{edge}-axis was measured using a $29 \times 30 \times 60\,\mathrm{cm}^3$ RW3-phantom. Three fields (5×5, 10×10 and $20 \times 20\,\mathrm{cm}^2$) were applied at gantry angle 0°. The out-of-field doses for proximal positions reaching from 0 to 13 cm were measured parallel to the x-axis (15 cm from the field edge and in a phantom depth of 15 cm parallel the CAX, see Fig. 5).

In order to verify the predicted patient scatter on the MPAX, phantoms with sizes of $30 \times T \times 60\,\mathrm{cm}^3$ (T from 15 to 30 cm) were constructed by continuously adding five 1 cm slabs, resulting in R_{iso}-values of 7.5-15 cm. Fields ($10 \times 10\,\mathrm{cm}^2$) with 1 Gy isocenter doses were applied from gantry angle 0° and the doses were conducted at $(x = X_{iso}, y = Y_{iso}, z_{edge} = 15\,\mathrm{cm})$. To determine C_B, patient scatter was registered 15 cm from the field edge parallel to the CAX resulting in R-values between 0.6 to 25.6 cm.

Finally, treatment plans using 2, 3, 4, 5, and 6 equally spaced fields and a 360° rotation plan were prepared such that a volume of around $1000\,\mathrm{cm}^3$ received at least 95 % of the isocenter dose (V_{95}). In the $30 \times 30 \times 60\,\mathrm{cm}^3$ RW3-phantom, the V_{95} was adjusted for each plan by changing the width of the single fields while keeping the length at a constant value of 10 cm.

2. *Measurements of collimator scatter and head leakage*

To determine the functions $\mathrm{F_c}(W, L, W_{mlc})$ (Eq. 11) and $\mathrm{G_{collimator/leakage}}(z_{iso})$ (Eq. 12), as well as the two constants $\mu(E_{collimator/leakage})$, the collimator scatter was extracted by subtracting the head leakage from the machine scatter (see Eq. 1). To measure the machine scatter, 100 MUs were irradiated in air for open fields (jaws defined by the MLCs). With closed MLCs, W- and L-jaws the head leakage could be registered with a chamber. To avoid a gap for the primary beam to leak through, an asymmetric jaw closing ($W_1 = -0.5$, $W_2 = 1\,\mathrm{cm}$) was adjusted. To retain shielding conditions between the machine scatter and head leakage measurements, the L_1-jaw (see Fig. 5) had to be in the same position for the measurement with the jaws closed or open. Therefore, only the L_2-jaw was moved to close the field in the longitudinal direction. All measurement positions were located along the target-gun direction away from the isocenter, once for the TrueBeam and once for the Clinac iX.

To find $\mathrm{G_{collimator/leakage}}(z_{iso})$, the out-of-field dose from 20 to 90 cm in 10 cm steps was measured in air along the MPAX (see Fig. 5). At the same locations, field sizes of 5 to 20 cm in length for constant width (10 cm) and from 5 to 20 cm in width for constant length (10 cm) were measured to determine the field size dependence of $\mathrm{F_c}(W, L, W_{mlc})$. The effect of different MLC openings was measured with a $10 \times 10\,\mathrm{cm}^2$ field with fixed jaw positions and varying MLC positions. The MLC shapes with width- and length-openings of 8, 5, and 3 cm were investigated. These measurements were important to model dynamic MLC movements for treatment plans used in IMRT or VMAT, whereby the jaw openings are considerably different from the MLC positions.

In order to verify the determined parameters of functions $\mathrm{F_c}(W, L, W_{mlc})$ and $\mathrm{G_{collimator/leakage}}(z_{iso})$, a 4-field and an IMRT plan [19] were irradiated with the Clinac iX and measured in air on the MPAX 30 cm from the isocenter.

To determine $\mu(E_{collimator/leakage})$, the chamber was placed once in a $30 \times 30 \times 30\,\mathrm{cm}^3$ water-phantom and once in air. The dose of $10 \times 10\,\mathrm{cm}^2$ field was registered to determine $\mu(E_{collimator})$. For $\mu(E_{leakage})$ head leakage was measured with closed jaws and MLCs. The phantom was placed at different MPAX positions such that the chamber could be moved along the x-axis (Fig. 5). Irradiated at gantry angle 90°, the stray dose was measured at five locations along the x-axis. This resulted in five different l-values for every MPAX position. The measurement in water was divided by the measurement in air to extract the attenuation coefficient,

$$\frac{D_{vacuum} \cdot \exp(-l \cdot \mu_{water})}{D_{vacuum} \cdot \exp(-l \cdot \mu_{air})} = \exp(-l(\mu_{water} - \mu_{air})) \approx \exp(-l \cdot \mu_{water}), \tag{15}$$

where D_{vacuum} is the dose which would be measured in vacuum, l is the path through the phantom, and $\mu_{water/air}$ is the attenuation coefficient in water and air, respectively. l is a straight line trajectory through the water-phantom, connecting the scatter origin and the chamber. The head leakage origin was assumed to be the target where the primary beam is produced. The target is located 100 cm above the isocenter in the gantry's head. The rear L-jaw (L_2 in Fig. 5) was assumed to be the origin of collimator scatter. L_2 is located 67 cm above the isocenter in the gantry's head.

C. Verification of the model with whole-body TLD measurements

The verification of the model's total out-of-field dose estimation for an IMRT, VMAT, and 4-field plan of a rhabdomyosarcoma in the prostate was compared to whole-body dose distribution measurements done by Hälg at al. [19], which were extended for this work. In an adult anthropomorphic Alderson-Rando phantom (RSD Radiology Support Devices, Long Beach, CA, USA), 183 TLDs were distributed and the various plans were applied. The model dose grid ranged from 11-86 cm away from the isocenter and covered 142 of the TLDs. The grid consisted of two million dose voxels with dimensions $2 \times 2 \times 5\,\mathrm{mm}^3$. The irradiation target was located in the prostate and the Alderson-phantom was positioned head first supine. The outline of the Alderson-phantom was imported from the structure set DICOM-file generated by the TPS (Varian Eclipse version 10.0, AAA-algorithm version 10.0.28). The whole-body of the Alderson-phantom was assumed to be water equivalent. All computations were performed using IDL (IDL Exelis Visual Information Solutions, Boulder, CO, USA).

For each field of a therapy plan, the out-of-field dose was calculated separately. The plans were exported from the TPS. For 3DCRT and IMRT plans, the DICOM-file consist of information per field. In case of a VMAT plan, the information is available in form of 177 control points. Patient scatter from a 6-field plan was similar to a rotation plan when the same V_{95} was treated, as can be seen in Fig. 7. Hence, the 177 VMAT control points were combined to six discrete fields.

To calculate the patient scatter, the isocenter dose, the field width, and field length had do be extracted for each field. The isocenter dose for a static- and an IMRT-field was taken from the DICOM-file. The VMAT plan provided control point weights which add up to 1. These weights were combined to six discrete fields and multiplied with the total isocenter dose. For each field, the width and length were calculated according to the beam's eye view. For the static-field plan either the MLCs or the jaws defined the aperture from where the mean width and length were calculated. Hence, the model uses rectangular fields. For the VMAT plan, complex field shapes were approximated by rectangles. For each IMRT-field, the MLC positions at the beginning of treatment were subtracted from the positions at the end and the resulting area was approximated by a rectangle. For every field and dose grid point, the lateral displacement proximal to the CAX and the MPAX (S-value), the displacement parallel to the CAX (R-value), and the distance from the field edge (z_{edge}-value) had to be calculated.

To calculate the collimator scatter, the jaw width and length, the numbers of MUs, and in case of the IMRT and VMAT plans, the mean MLC length opening were determined for every field. Furthermore, each dose grid point in the Alderson-phantom was projected onto the MPAX and z_{iso} was calculated. For the head leakage contribution, the numbers of MUs and z_{iso} must be known. For both collimator scatter and head leakage, the beam path inside the phantom was determined for every dose grid point and gantry angle. For leakage, the calculated trajectories were straight-line connections between the beam producing target and each dose grid point. For collimator scatter, straight-line connections between the rear L-jaw (L_2 see Fig. 5) to each dose grid point. Collimator scatter and head leakage were normalized to one treatment Gy by scaling to the numbers of applied MUs accordingly.

III. RESULTS

Unless otherwise stated, the absolute deviations (Dev) of the predicted ($D_{predicted}$) to the measured doses ($D_{measured}$) are calculated by,

$$Dev = \frac{(|D_{predicted} - D_{measured}|)}{D_{measured}}. \tag{16}$$

A. Analytical model

Repeated out-of-field ionization chamber dose measurements down to 0.05 mGy variated not more than 2 %.

1. Patient scatter

In Fig. 6(a), the measured and predicted patient scatter doses for a 5 × 5, 10 × 10, and 20 × 20 cm^2 field as a function of the distance to the field edge can be seen. The measurements of the 20 × 20 cm^2 field at gantry angle 90° showed two outliers, such that only the 270° measurements were used. The smaller fields showed a maximal variation of 7 % between the chamber measurements at two different angles. The best agreement for all field sizes for measurement points from 10 to 50 cm away from the field edge was reached by setting $\mu(E_{patient})$ to a value of 0.0722 cm^{-1}. This resulted in a mean and a maximum deviation of 4 % and 12 % between measurements and model, respectively.

The measurements for different field widths were fitted best by the power function of Eq. 4 with a maximum deviation of 1 % [Fig. 6(b)].

The normalization constant C_N of the patient scatter model (Eq. 8) was determined to be 0.724 mGy/Gy. Two independent measurements had a difference of 2 %.

The predicted patient scatter for different distances parallel to the CAX (R-values) was minimized to a maximum difference of 3 % from the chamber measurements with $C_B = 0.203$ (Eq. 8). Using the fitted values (Table I), the predicted patient scatter in the middle of the phantom for different body thicknesses (R_{iso}-variation) was plotted versus the measurements. Fig. 6(d) shows that the model is in accordance with the measurements for different R_{iso} values with a maximum deviation of 2 %.

TABLE I. The used parameters of the patient scatter model (Eq. 8) for a 6 MV nominal beam energy.

C_W	C_N	C_B	$\mu(E_{patient})$	$\mu(E_{field,10\times10\,\mathrm{cm}^2})$
0.845	0.724 mGy/Gy	0.203	0.007 22 mm^{-1}	0.005 41 mm^{-1} (from Birgani et al. [21])

All experimentally evaluated field sizes showed a similar dose decrease proximal to the MPAX and CAX (S-value). For smaller fields, this decrease was more pronounced. The average mean difference of the model prediction was 4 % compared

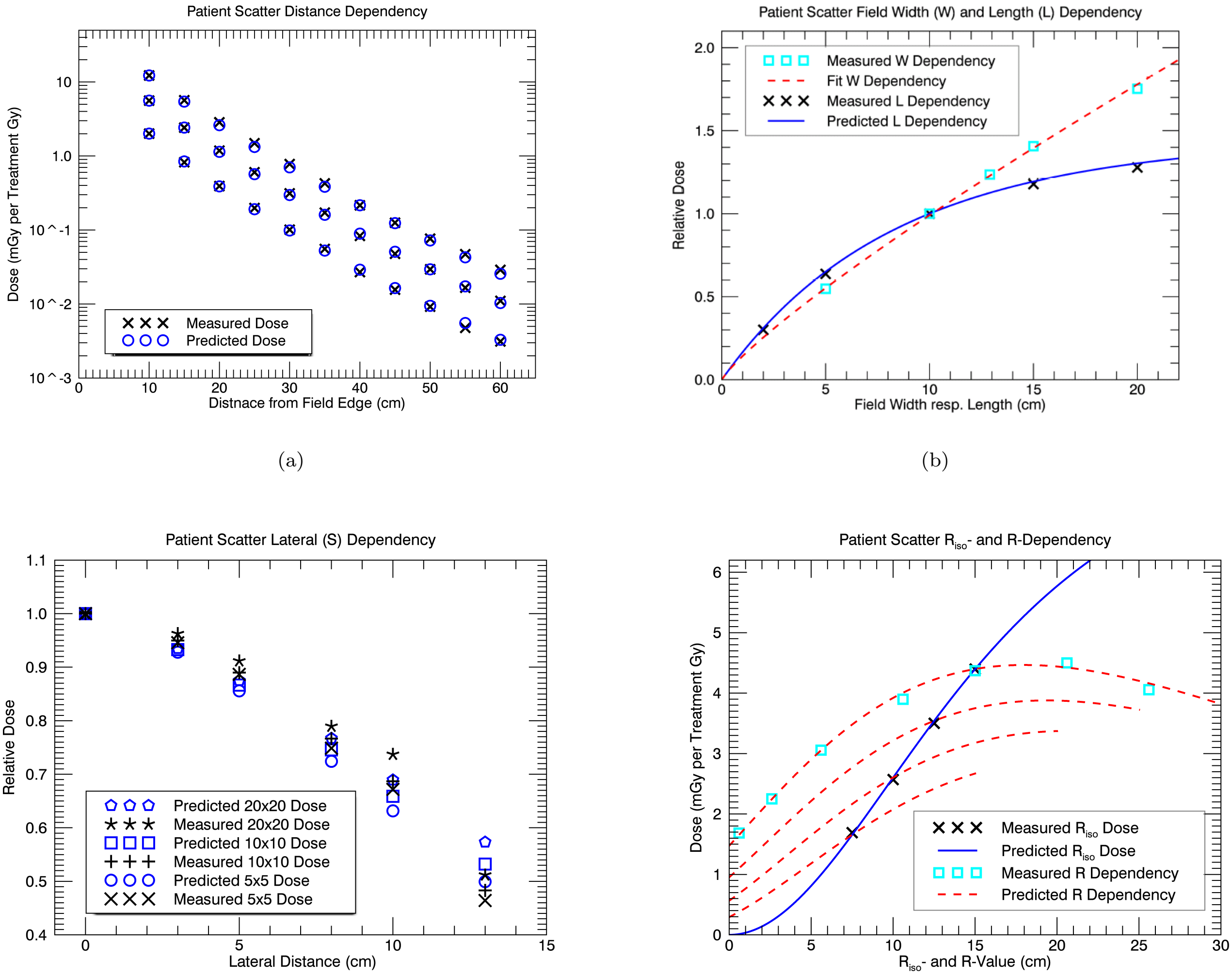

(a)

(b)

(c)

(d)

FIG. 6. Patient scatter (Eq. 8) dependence of (a) the distances to the field edge along the MPAX per treatment Gray. The lower points correspond to a 5×5, the middle to a 10×10, and the upper to a $20 \times 20\,\mathrm{cm}^2$ field. (b) Field width (W) and length (L) dependence of patient scatter normalized to a $10 \times 10\,\mathrm{cm}^2$ field. (c) Lateral (proximal to the CAX and MPAX) decrease of patient scatter normalized to no displacement. (d) Pattient scatter 15 cm from the field edge once on the MPAX (R_{iso}) for different slab-phantom thicknesses (15-30 cm) measured and predicted, and once parallel to the CAX (R-values) measured for a phantom thickness of 30 cm and predicted for thicknesses of 15-30 cm.

to the measured patient scatter. At the biggest S-value of 13 cm, the maximum difference of 12 % corresponding to the $20 \times 20\,\mathrm{cm}^2$ field was found [Fig. 6(c)].
The model prediction of the field lengths (L) behaviour showed a maximum deviation of 4 % compared to the dose measurements [Fig. 6(b)].
The patient scatter measured for various treatment techniques was predicted with a maximum deviation of 4 %. The 2-field technique showed the smallest and the 3-field the highest patient scatter contribution on the MPAX (2.5 times higher, 15 cm from the field edge). For the 4-field plans applied to different slab-phantoms, the dose increased toward larger phantom thicknesses and has a maximum deviation of 7 % compared to the measurements (Fig. 7).

2. *Collimator scatter and head leakage*

For both linear accelerators (iX and TrueBeam), head leakage increases linearly with increasing distance from the isocenter in direction target toward gun. The fit of a linear function (Eq. 14) deviated in maximum 3 % and 8 % from the measurement for the TrueBeam and the iX, respectively. The gradient for the iX is four times larger than for the TrueBeam (Table II).

Collimator scatter shows a power-law behavior toward bigger distances from the isocenter. At around 40 cm the dose increases, as modeled by Eq. 12. Collimator scatter was fitted using weights which were proportional to the inverse of head

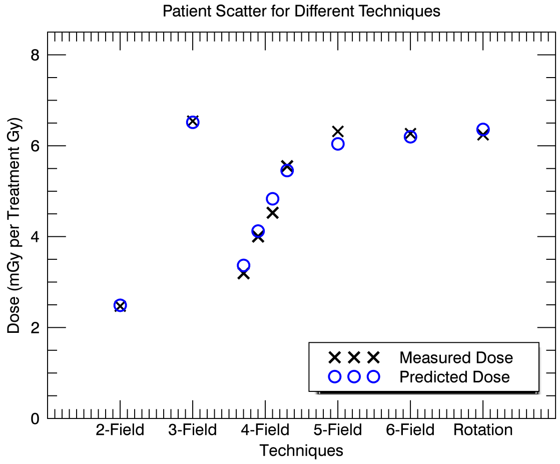

FIG. 7. Patient scatter per one Gray isocenter dose for various treatment techniques on the MPAX at 15 cm from the field edge. All plans except the 4-field were applied onto a $30 \times 30 \times 60\,\mathrm{cm}^3$ slab-phantom. The 4-field plans were irradiated on slab-phantoms with sizes of $30 \times T \times 60\,\mathrm{cm}^3$ (T from 15 to 30 cm from left to right). All measured plans had a V_{95} of around $1000\,\mathrm{cm}^3$.

TABLE II. The measured parameters corresponding to the head leakage model (Eq. 13) for a 6 MV nominal beam energy.

	TrueBeam		iX	
$\mathrm{G}_{\mathrm{leakage}}$	C_8	C_9	C_8	C_9
	0.134	$5.98 \cdot 10^{-5}$	0.0730	$2.58 \cdot 10^{-4}$

leakage. All fitted parameters are listed in Table III.

TABLE III. The measured constants corresponding to the collimator scatter model (Eq. 10) for a 6 MV nominal beam energy.

	TrueBeam		iX	
$\mathrm{F_c}(W, L, W_{mlc})$	C_1	C_2	C_1	C_2
$\frac{W_{mlc}}{W} \leq 0.8$	0.620	0.599	0.511	0.670
$\frac{W_{mlc}}{W} > 0.8$	1	0	1	0

$\mathrm{G}_{\mathrm{W_G \times L_G}}$	C_3	C_4	C_5	C_6	C_7	C_3	C_4	C_5	C_6	C_7
$G_{5\times5\,\mathrm{cm}^2}$	$3.00 \cdot 10^6$	-2.86	3.06	482	55.3	$3.00 \cdot 10^6$	-3.02	0	–	–
$G_{10\times10\,\mathrm{cm}^2}$	$1.46 \cdot 10^5$	-2.19	1.67	521	85.8	$6.29 \cdot 10^5$	-2.44	1.98	522	87.0
$G_{20\times20\,\mathrm{cm}^2}$	$3.10 \cdot 10^6$	-2.48	1.76	553	131	$5.20 \cdot 10^6$	-2.60	2.28	575	-127

For all field sizes (5×5, 10×10 and $20 \times 20\,\mathrm{cm}^2$) and the two different linear accelerators, the biggest deviation of the fitted collimator scatter with respect to the measurement in air was 19 %. For this comparison, points where excluded at which head leakage was at least three times bigger than collimator scatter. Furthermore, the closest measurement location to the isocenter ($z_{iso} = 20\,\mathrm{cm}$) of the $20 \times 20\,\mathrm{cm}^2$ field had to be excluded. This close to the isocenter, the shielding effect of the jaws and MLCs for big fields is different compared to smaller fields. The measurements and the corresponding fits for collimator scatter and head leakage for the TrueBeam can be seen in Fig. 8(a). In addition, head leakage is plotted for measurements away from the isocenter in direction gun toward target.

The field size dependence of collimator scatter (Eq. 11) shows a linear increase toward wider and longer jaw positions (jaws defined by the MLCs). The origin of collimator scatter is assumed to be the rear L-jaw (L_2 in Fig. 5). To preserve scatter conditions, only the L_1-jaw was moved for the measurement of the field length dependence. The L_2-jaw remained at an opening of 5 cm. These asymmetric jaw set ups resulted in different shielding conditions of the scattered primary beam compared to symmetric fields. As a consequence, field lengths up to 15 cm were used for modeling.

The change in dose for different MLC widths (constant jaw positions) can be fitted by a linear function (Eq. 11). The increase in dose was less pronounced for locations closer to the isocenter than those further away. Nevertheless, the average collimator scatter changes at z_{iso}-positions were fitted from 30 to 60 cm for the iX and from 20 to 70 cm for the TrueBeam. At a MLC width opening of 80 % of the jaw width opening, the out-of-field dose is bigger than for the jaws defined by the MLCs. However, this has no consequence for a real patient treatment as the MLC- and jaw-settings are similar for a 3DCRT plan. In case of an intensity-modulated plan, the MLC width opening is much smaller than the jaw width opening. All parameters are listed in Table III. Collimator scatter measurements for MLC openings in length showed no clear trend and were not modeled according to the measurements.

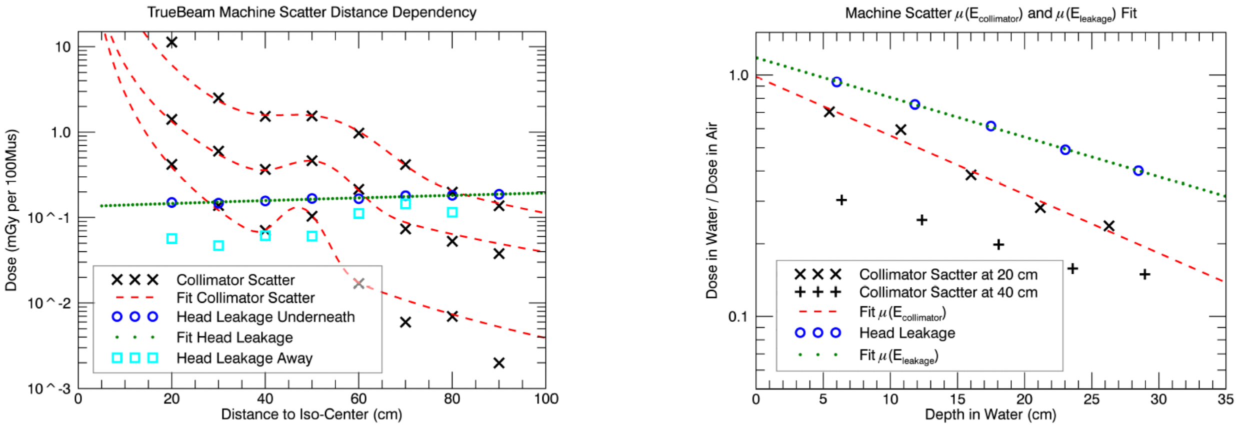

(a) (b)

FIG. 8. (a) The measured TrueBeam machine scatter out-of-field dose for different distances to the isocenter in direction target toward gun. The X's represent various field sizes to determine the collimator scatter. The lower X's correspond to a 5 × 5, the middle to a 10 × 10, and the upper to a 20 × 20 cm^2 field. In addition, head leakage measured away from the isocenter in direction gun toward target are represented by the squares. (b) The ratio of collimator scatter and the ratio of head leakage between the measurements in air and water to determine the attenuation coefficients $\mu(E_{collimator/leakage})$.

Finally, the machine scatter dose in air for a real patient plan could be compared to the model's prediction. A 4-field plan resulted in 12 % deviation of the predicted versus the modeled point dose. The plan contained a boost in form of four small fields. For these fields, the dose prediction deviated in average by 24 % relative to the measurement while the four larger fields only deviated 8 % on average. The IMRT plan out-of-field dose resulted in a deviation of 20 %.
The collimator scatter attenuation coefficient in water was determined to be 0.0561 cm^{-1} from the measurement at the iX linear accelerator. Only the dose values at a distance of 40 cm away from the isocenter were used to determine $\mu(E_{collimator})$ because there the fit of an exponential function will predict no attenuation for 0 cm depth in water [see Fig. 8(b)]. The mean value of $\mu(E_{leakage})$ was 0.0377 cm^{-1}. In contrast to $\mu(E_{collimator})$, the leakage attenuation was similar for all measured distances to the isocenter. The fit at a distance of 60 cm from the isocenter can be seen in Fig. 8(b).

B. Whole-body dose-distribution prediction

The double standard error (2SD) and thus the 95 % confidence interval for the TLD measurements of the 4-field plan irradiated on the iX and the TrueBeam were ±10 %. For the IMRT and the VMAT plan measurements done by Hälg et al. [19], the 2SD was ±33 % due to another method.
Unless otherwise stated, the difference between TLD measurements and model-calculated stray dose is given for 12.5-82 cm from the isocenter (around 7.5-77 cm from the field edge, see Fig. 9). For the TPS and TLD measurement, the dose difference is given for 7.5-10 cm from the isocenter (around 2.5-5 cm from the field edge, see Fig. 9).

The model prediction deviated on absolute mean by 9 % and in maximum by 28 % to the measurement of the 4-field plan made on the iX. For the 29 detectors along the MPAX, the absolute mean was 9 % and the maximum difference 26 %. The TPS predicted the dose to an absolute mean and a maximum deviation to the measurements of 5 % and 16 %, respectively. For the 4-field plan measured with the TrueBeam, the absolute mean and maximum deviation of the model at the 142 TLD locations were 11 % and 37 %, respectively. For the MPAX the maximum deviation was reduced to 29 %. The TPS predicted the dose for the TrueBeam to an absolute mean and maximum difference of 4 % and 12 %, respectively. The iX linear accelerator showed on average a higher out-of-field dose than the TrueBeam, whereby the measured stray dose was 1.5 times higher at a distance 75 cm away from the isocenter.
The VMAT plan DICOM control points were combined in six discrete fields for the stray dose calculation. The absolute mean deviation was 11 % with a maximum of 41 % at a distance of 50 cm away from the isocenter. A discretization of the

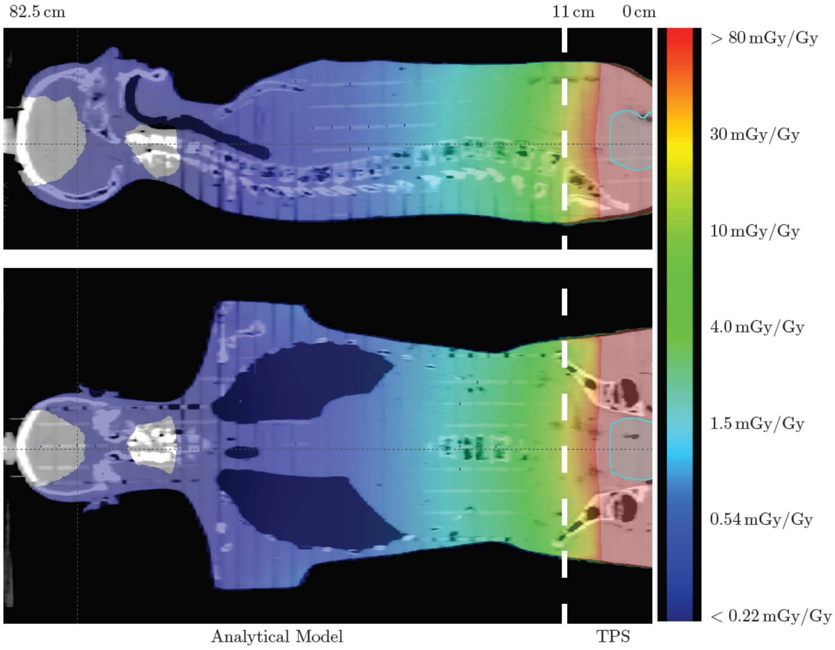

FIG. 9. Analytical model and TPS fused total dose per treatment Gy for the 4-field plan imported in the TPS. The outline of the target can be seen in the hip region.

control points into 12-fields did not show better results. For a 3-field discretization, the maximum deviation was reduced to 34 % but the absolute mean discrepancy increased to 13 %. Out of all measured plans, the VMAT showed the smallest maximum deviation of 20 % along the MPAX compared to the model prediction. The TPS deviated 8 % on absolute mean with a maximum of 17 % to the TLD measurements.
The IMRT plan showed an absolute mean and maximum deviations of 11 % and 44 %, respectively, between the modeled and the measured out-of-field dose. From 20-82 cm away from the isocenter, the absolute mean and maximum deviation were 9 % and 32 %, respectively. The maximum deviation located at 22.5 cm along the MPAX, the measured dose, and the predicted different contributions for all plans can be seen in Fig. 10. The TPS dose showed an absolute mean and a maximum deviation to the IMRT plan measurement of 15 % and 24 %, respectively.
The model calculation based on matrix operations needed 9 minutes to calculate the 2×10^6 dose grid points per field. Six of the 9 min were for the calculation of patient scatter and 3 min for collimator scatter and head leakage contributions. The software IDL used a single core of an Intel Xeon CPU E5420 at 2.5 GHz to calculate the stray dose.

IV. DISCUSSION

We developed a model to determine the out-of-field dose for photon radiation therapy delivered with Varian linear accelerators operated at 6 MV nominal beam energy. The stray dose was separated according to its origins: head leakage, collimator, and patient scatter [15]. For patient scatter, a mechanistically based model was developed. The various parameters were determined using measurements of the stray dose in simple geometries. The out-of-field model was implemented in the software IDL and uses only the exported DICOM body-outline and plan from the TPS as basic input. For a realistic verification of the model, treatment stray doses for a rhabdomyosarcoma in the prostate of several techniques (3DCRT, IMRT, and VMAT) were calculated and compared to systematic TLD measurements in an anthropomorphic phantom [19]. The TPS dose was calculated up to 12 cm from the isocenter. To avoid a gap in the whole-body dose grid, the model was applied to 11 cm from the isocenter (around 6 cm from the field edge). The TPS and model dose grids were fused and reimported in to the TPS. The fused whole-body out-of-field dose showed an absolute mean deviation of 11 % and a maximum deviation below 44 % compared to TLD measurements.

A. Patient scatter

A highly adaptive patient scatter model was presented and tested for different distances to the field edge, patient and field sizes, and delivery techniques. The model of patient scatter was trained with measurements from 10-50 cm from the field edge, for field widths of 5-20 cm and lengths of 2-20 cm. Although several empirical models are available describing internal scatter [9, 13], this is, to our knowledge, the first mechanistic model of patient scatter.
For all measured field sizes the model estimates the patient scatter dose accurately and the assumption to set $\mu(E_{patient})$

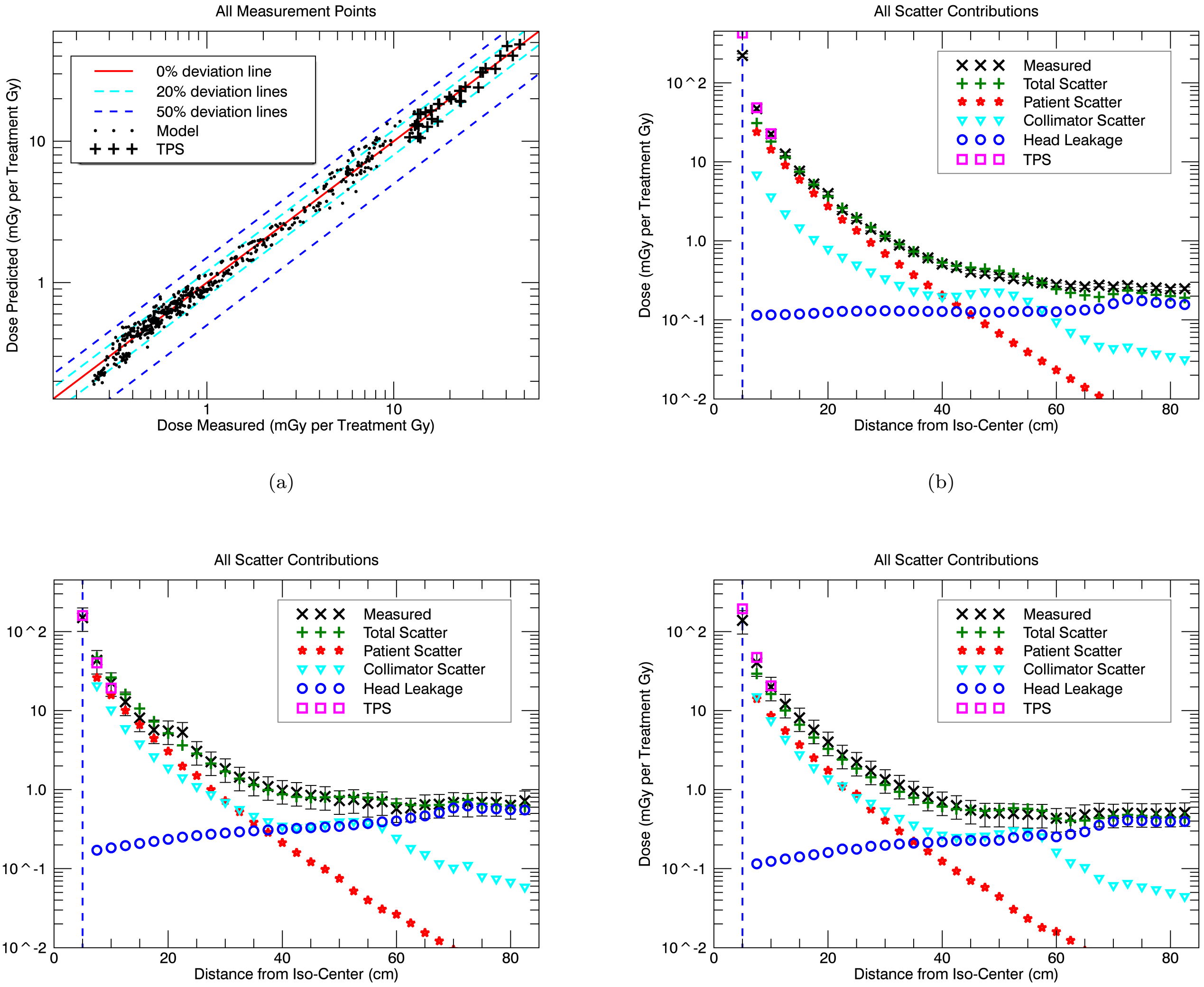

(a) (b)

(c) (d)

FIG. 10. (a) The Alderson measurements (head first suppine) compared to the predicted doses for 605 TLDs of the four plans. Furthermore, the single stray dose contributions, the total predicted, and the measured doses along the MPAX for (b) the 4-field plan measured with the TrueBeam, (c) the IMRT and (d) VMAT plan measured with the iX. The dashed line in (b)-(d) indicates the field edge. The TLD error bars are the estimated double standard error.

constant is justified [Fig. 6(a)]. In water, the value of $\mu(E_{patient})$ (Table I) corresponds to a photon energy of around 0.9 MeV (National Institute of Standards and Technologies). Chofor et al. [5] simulated a mean patient scatter energy of 0.8 MeV for a Siemens Primus linear accelerator and a nominal beam energy of 6 MV. This is in agreement with our measurements.
The patient scatter variation parallel to the CAX (R-dependence) is well predicted by scaling the back scatter in Eq. 8 by a constant C_B [Fig. 6(d)]. For all phantom thicknesses (R_{iso} variation), patient scatter on the MPAX is excellently predicted by the model when compared to the measurements.
The patient scatter model predicts well the bigger gradients of the relative dose decrease proximal to the CAX and MPAX for smaller field sizes when compared to larger field sizes [Fig. 6(c)].
In Fig. 7, the large increase in patient scatter when using multiple field plans instead of a 2-field plan can be explained by bigger field widths of the multiple field plans to irradiate the same V_{95}. The variation in patient scatter among the 3-,4-,5-,6-field, and rotation plans applied onto the same phantom is a result of different R-values and field widths.

B. Collimator scatter and head leakage

A simple empirical model for machine scatter was presented and tested for two treatment plans. Head leakage and collimator scatter were measured along the MPAX from 20 cm up to 90 cm from the isocenter. Additionally, collimator scatter was measured for various symmetric jaw positions defined by the MLCs and for constant jaw positions combined with different MLC openings.

For the smallest field measured, head leakage was the main contribution to the machine scatter after a distance of 30 cm away from the isocenter (in direction target toward gun). For the largest field measured, this distance is shifted to 90 cm [Fig. 8(a)]. Hence, it is much more important to accurately model collimator scatter for larger fields than for small ones.

For constant jaw positions, collimator scatter measured with MLCs retracted is higher when compared to the measurement, where the jaws are defined by the MLCs. This is caused by a different shielding. A similar shielding effect was seen when a field (jaws defined by the MLCs) with a length of 20 cm is measured close to the isocenter. Hence, for large field lengths, the prediction of collimator scatter close to the isocenter gets worse [Fig. 8(a)].

For asymmetric fields where the width and the length deviate more than 5 cm, it is recommended to remeasure the collimator scatter and redetermine the parameters of Eq. 12.

From publications [5, 9] as well as from the measured variation in $\mu(E_{collimator})$ along the MPAX, various origins for collimator scatter can be noticed. A more sophisticated analytical model for collimator scatter is the multi plane source model of Benadjaoud [6]. The model predicts collimator scatter of open fields compared to measurements to an average accuracy of 9 % and maximum difference of 40 % (maximum is located 30 cm from the CAX). Furthermore, calculations of complex field-shapes (defined by the MLC) are possible. The simple collimator scatter model used here predicted machine scatter 30 cm from the isocenter for moving MLCs (IMRT plan) with a difference of 20 % compared to the chamber measurement. Moreover, to calculate collimator scatter for every MLC control point of an intensity-modulated plan would be too time consuming.

The determined $\mu(E_{collimator})$ is smaller than $\mu(E_{patient})$. Collimator scatter photons reach a specific point in the patient only if they are scattered in a smaller angle than photons from a patient scatter process.

C. Whole-body dose-distribution

The three model-calculated out-of-field dose components for the 4-field and the IMRT plan [Figs. 10(b) and (c)] are in agreement with the measured data by Ruben et al. [15]. Compared to the IMRT plan, patient scatter of the VMAT plan is reduced caused by applying smaller field sizes when treating the same target. Furthermore, machine scatter is decreased because a smaller number of MUs is needed to deliver the VMAT when compared to the IMRT plan.

Various MC studies have been published [3–5, 10] where out-of-field dose was simulated in simple geometries. For a complex MC code with over 100 accelerator components integrated in the simulation [10], the average local difference was 14 % for the simulation of open fields (MLC retracted) compared to TLD measurements. Kry et al. [14] simulated out-of-field doses in an anthropomorphic phantom for 6 MV IMRT plans to an average absolute difference compared to TLD measurements of 14 %. The model presented in this paper calculated the out-of-field dose for real treatment plans to an average local difference of 11 % compared to TLD measurements. Depending on the computer cluster, MC simulations need hours up to days to determine the out-of-field dose. The model presented here calculates the stray dose of one field in around 30 s for a voxel size of $1 \times 1 \times 1\,\mathrm{cm}^3$, which is sufficient for modeling secondary tumor induction [3]. To our knowledge, there is no publication about whole-body out-of-field dose calculation for VMAT plans.

A physics-based analytical model to calculate the therapeutic and stray doses was introduced by Jagetic and Newhauser [9]. The algorithm was tested for open fields in simple geometries up to distances of 40 cm from the isocenter and resulted in a root mean square (RMS) deviation below 9.3 % for all measured fields. Our model predicted the out-of-field dose from 20 to 90 cm from the isocenter with a RMS discrepancy of 11.6 % compared to the 4-field, IMRT, and VMAT plan measured with the iX in the Alderson phantom. Furthermore, the model of Jagetic and Newhauser cannot be used for IMRT and VMAT modalities and was not tested for complex geometries.

The model-calculated out-of-field dose grids of the various treatment plans were fused with the TPS dose grids. The model-calculated out-of-field dose had to be extended closer to the isocenter to avoid a gap in the whole-body dose. Although the parameters of the model were not trained so close to the isocenter, the out-of-field dose was well predicted between 11 cm and 20 cm. This good agreement between modeled and measured stray doses could be a consequence of the mechanistically based modeling of patient scatter, since internal scatter is the main contribution in this range [5, 9, 15–17]. The out-of-field dose was calculated by the TPS up to 11 cm from the isocenter (6 cm from the field edge). The TPS-prediction lay within the accuracy we aimed for in this work [Fig. 10(a)]. The good agreement on the MPAX between the model-calculated and the TPS-predicted dose compared to the TLD measured dose can be seen in Figs. 10(b)-(d). In the same figures, the smooth transition between the TPS dose and the model-calculated stray dose is shown.

The whole-body dose distribution imported into the TPS can be used for further analysis. From the transversal view of the model-calculated 3DCRT stray dose shown in Figs. 11(a) and 11(b), it can be seen that at 10 cm from the field edge, the dose increases toward the center of the body as a consequence of the internal patient scatter contribution. The opposite is true for a distance of 72.5 cm from the field edge, where external machine scatter is dominating and the center is shielded by the body itself.

Our mechanistic model of patient scatter can be used right away for all treatment machines with a similar beam energy spectrum compared to 6 MV Varian beams. For other nominal beam energies or flattening filter free beams, simple measurements could be done to fit the four patient scatter parameters (Table I). Head leakage and collimator scatter have to be adapted for different energy spectra and treatment geometries. For energies larger than 10 MV, an additional model for

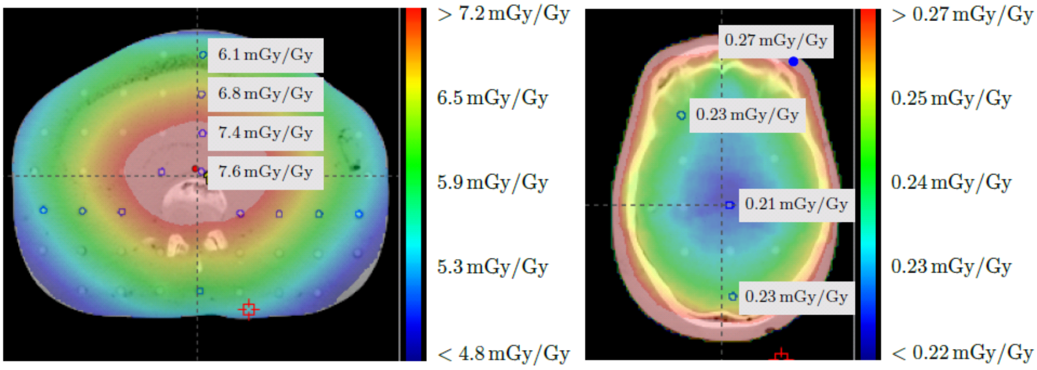

(a) (b)

FIG. 11. In color wash the model-calculated and in the boxes the measured out-of-field dose for transversal slices in the phantom (a) 15 cm and (b) 77.5 cm from isocenter. The blue circles represent the TLD locations. Indicated by the solid blue circle the TLD placed on the left eye at a distance of 76 cm from the isocenter.

neutron dose is necessary [22]. It is planned to measure the stray dose of high energy photons (15 MV), to refit the model parameters and compare the predictions of the model to high energy TLD measurements in the Alderson phantom.
The current model was just tested for one target size and location. Further investigations are planned for different locations and target sizes. An automatic integration of the out-of-field dose algorithm in a commercial TPS was not performed. The problem of a TPS integration is the size of the planning CT of the patient, which is usually linked to the treatment location. A possible solution would be to fuse the planning CT with the scaled Alderson phantom containing a wide range of organs at risk [19, 23]. For this, it is planned to develop an algorithm which correctly resizes the Alderson phantom and all its contained structures to the patient's anatomy.

ACKNOWLEDGEMENT

This work was funded by the grant KFS-3249-08-2013 from the Swiss Cancer League.

DISCLOSURE

The authors have no relevant conflicts of interest to disclose.

[1] Horner MJ, Ries LAG, Krapcho M, Neyman N, Aminou R, Howlader N, Altekruse SF, Feuer EJ, Huang L, Mariotto A, Miller B, Lewis D, Eisner M, Stinchcomb D, and Edwards B, "SEER Cancer Statistics Review, 1975-2006, National Cancer Institute," .

[2] Schneider U, "Modeling the risk of secondary malignancies after radiotherapy," Genes **2**, 1033–1049 (2011).

[3] Kry SF, Titt U, Pönisch F, Followill D, Vassiliev ON, White RA, Mohan R, and Salehpour M, "A Monte Carlo model for calculating out-of-field dose from a Varian 6 MV beam," Medical Physics **33**, 4405–4413 (2006).

[4] Joosten A, Bochud F, Baechler S, Levi F, Mirimanoff RO, and Moeckli R, "Variability of a peripheral dose among various linac geometries for second cancer risk assessment," Physics in Medicine and Biology **56**, 5131–5151 (2011).

[5] Chofor N, Harder D, Willborn KC, and Poppe B, "Internal scatter, the unavoidable major component of the peripheral dose in photon-beam radiotherapy," Physics in Medicine and Biology **57**, 1733–1743 (2012).

[6] Benadjaoud MA, Bezin J, Veres A, Lefkopoulos D, Chavaudra J, Bridier A, de Vathaire F, and Diallo I, "A multi-plane source model for out-of-field head scatter dose calculations in external beam photon therapy," Physics in Medicine and Biology **57**, 7725–7739 (2012).

[7] Ahnesjö A, "Collimator scatter in photon therapy beams," Medical Physics **22**, 267–278 (1995).

[8] McParland BJ and Fair HI, "A method of calculating peripheral dose distributions of photon beams below 10 MV," Medical Physics **19**, 283–293 (1992).

[9] Jagetic LJ and Newhauser WD, "A simple and fast physics-based analytical method to calculate therapeutic and stray doses from external beam, megavoltage X-ray therapy," Physics in Medicine and Biology **60**, 4753 (2015).

[10] Bednarz B and Xu XG, "Monte Carlo modeling of a 6 and 18 MV Varian Clinac medical accelerator for in-field and out-of-field dose calculations: development and validation," Physics in Medicine and Biology **54**, N43–N57 (2009).

[11] Howell RM, Scarboro SB, Kry SF, and Yaldo DZ, "Accuracy of out-of-field dose calculations by a commercial treatment planning system," Physics in Medicine and Biology **55**, 6999–7008 (2010).

[12] Schneider U, Hälg RA, Hartmann M, Mack A, Storelli F, Joosten A, Möckli R, and Besserer J, “Accuracy of out-of-field dose calculation of tomotherapy and cyberknife treatment planning systems: a dosimetric study,” Zeitschrift Für Medizinische Physik **24**, 211–215 (2014).

[13] Taddei PJ, Jalbout W, Howell RM, Khater N, Geara F, Homann K, and Newhauser WD, “Analytical model for out-of-field dose in photon craniospinal irradiation,” Physics in Medicine and Biology **58**, 7463–7479 (2013).

[14] Kry SF, Salehpour M, Titt U, White RA, Stovall M, and Followill D, “Monte Carlo study shows no significant difference in second cancer risk between 6- and 18-MV intensity-modulated radiation therapy,” Radiotherapy and Oncology **91**, 132–137 (2009).

[15] Ruben JD, Lancaster CM, Jones P, and Smith RL, “A comparison of out-of-field dose and its constituent components for intensity-modulated radiation therapy versus conformal radiation therapy: implications for carcinogenesis,” International Journal of Radiation Oncology • Biology • Physics **81**, 1458–1464 (2011).

[16] Kase KR, Svensson GK, Wolbarst AB, and Marks MA, “Measurements of dose from secondary radiation outside a treatment field,” International Journal of Radiation Oncology • Biology • Physics **9**, 1177–1183 (1983).

[17] Lillicrap SC, Morgan HM, and Shakeshaft JT, “X-ray leakage during radiotherapy,” The British Journal of Radiology **73**, 793–794 (2000).

[18] Diallo I, Haddy N, Adjadj E, Samand A, Quiniou E, Chavaudra J, Alziar I, Perret N, Guérin S, Lefkopoulos D, and Vathaire F, “Frequency distribution of second solid cancer locations in relation to the irradiated volume among 115 patients treated for childhood cancer,” International Journal of Radiation Oncology • Biology • Physics **74**, 876–883 (2009).

[19] Hälg RA, Besserer J, and Schneider U, “Systematic measurements of whole-body dose distributions for various treatment machines and delivery techniques in radiation therapy,” Medical Physics **39**, 7662–7676 (2012).

[20] Klein O and Nishina T, “Über die streuung von strahlung durch freie elektronen nach der neuen relativistischen quantendynamik von Dirac,” Zeitschrift für Physik **52**, 853–868 (1929).

[21] Tahmasebi Birgani MJ, Behrooz MA, Shahbazian H, and Shams A, “Determination of the attenuation coefficient for megavoltage photons in the water phantom,” International Journal of Radiation Research **9**, 251–255 (2012).

[22] Kry SF, Salehpour M, Followill DS, Stovall M, Kuban DA, White RA, and Rosen II, “Out-of-field photon and neutron dose equivalents from step-and-shoot intensity-modulated radiation therapy,” International Journal of Radiation Oncology • Biology • Physics **62**, 1204–1216 (2005).

[23] Hälg RA, Besserer J, and Schneider U, “Systematic measurements of whole-body imaging dose distributions in image-guided radiation therapy,” Medical Physics **39**, 7650–7661 (2012).

Chapter 2

Whole-body dose and energy measurements in radiotherapy by a combination of LiF:Mg,Cu,P and LiF:Mg,Ti

Pascal Hauri[1,2] and Uwe Schneider[1,2]

[1] Institute for Radiotherapy, Radiotherapie Hirslanden AG, Aarau, Switzerland

[2] Department of Physics, University of Zurich, Zurich, Switzerland

This chapter was adapted from the original article:

“Whole-body dose and energy measurements in radiotherapy by a combination of LiF:Mg,Cu,P and LiF:Mg,Ti”

Published in:

Zeitschrift für Medizinische Physik 2017, in press.
doi:10.1016/j.zemedi.2017.07.002.

Purpose: Long-term survivors of cancer who were treated with radiotherapy are at risk of a radiation-induced tumor. Hence, it is important to model the out-of-field dose resulting from a cancer treatment. These models have to be verified with measurements, due to the small size, the high sensitivity to ionizing radiation and the tissue-equivalent composition, LiF thermoluminescence dosimeters (TLD) are well-suited for out-of-field dose measurements. However, the photon energy variation of the stray dose leads to systematic dose errors caused by the variation in response with radiation energy of the TLDs. We present a dosimeter which automatically corrects for the energy variation of the measured photons by combining LiF:Mg,Ti (TLD100) and LiF:Mg,Cu,P (TLD100H) chips.

Methods: The response with radiation energy of TLD100 and TLD100H compared to ^{60}Co was taken from the literature. For the measurement, a TLD100H was placed on top of a TLD100 chip. The dose ratio between the TLD100 and TLD100H, combined with the ratio of the response curves was used to determine the mean energy. With the energy, the individual correction factors for TLD100 and TLD100H could be found. The accuracy in determining the in- and out-of-field dose for a nominal beam energy of 6 MV using the double-TLD unit was evaluated by an end-to-end measurement. Furthermore, published Monte Carlo (MC) simulations of the mean photon energy for brachytherapy sources, stray radiation of a treatment machine and cone beam CT (CBCT) were compared to the measured mean energies. Finally, the photon energy distribution in an Alderson phantom was measured for different treatment techniques applied with a linear accelerator. Additionally, a treatment plan was measured with a Cobalt machine combined with an MRI device.

Results: For external radiotherapy, the presented double-TLD unit showed a relative type A uncertainty in doses of $-1\,\% \pm 2\,\%$ at the two standard deviation level compared to an ionization chamber. The type A uncertainty in dose was in agreement with the theoretically calculated type B uncertainty. The measured energies for brachytherapy sources, stray radiation of a treatment machine and CBCT imaging were in agreement with MC simulations. A shift in energy with increasing distance to the isocenter was noticed for the various treatment plans measured with the Alderson phantom. The calculated type B uncertainties in energy were in line with the experimentally evaluated type A uncertainties.

Conclusion: The double-TLD unit is able to predict the photon energy of scatter radiation in external radiotherapy, X-ray imagine and brachytherapy sources. For external radiotherapy, the individual energy correction factors enabled a more accurate dose determination compared to conventional TLD measurements.

Keywords: TLD, Out-of-Field, Photon Energy, Linear Accelerator, Brachytherapy, CBCT

I. INTRODUCTION

Radiation treatment modalities have steadily improved [intensity-modulated radiation therapy (IMRT), volumetric-modulated arc therapy (VMAT), proton and heavy ion therapy, etc.]. As a consequence, cancer cure rates have increased and it is expected that they will increase further in the future [1]. As a result, there are now many long-term survivors of cancer who are at risk of late effects from radiotherapy, including second primary cancers. These malignancies have been linked to chemotherapy as well as radiation exposure. It is estimated that more than 0.1 % of the population between the ages of 16 and 44 are survivors of childhood cancer [2]. The induction of second cancers can be an important side-effect of radiation. The basic input of the majority of cancer risk models is the dose distribution in the patient. The patient dose is usually calculated with a commercial treatment planning system (TPS). Commercial TPS, however, are commissioned to provide accurate dose distributions to judge the target dose and the dose to organs at risk (> 1 Gy). For locations beyond the treatment field borders, the accuracy of TPS computations can be orders of magnitude wrong [3, 4]. However, for the induction of second malignancies, those low dose volumes (mGy) can be of great importance. The accurate determination of the out-of-field patient dose is therefore an active field of research.

Currently, two methods are proposed to compute out-of-field dose: Monte Carlo simulations and bio-physical/empirical dose models. The accurate measurement of peripheral dose distributions is essential, either for testing the results of the dose computations or as the basis for model developments. In photon therapy, the dose distribution can vary by several orders of magnitude including a variation of the energy spectrum, which makes the accurate dose measurement not an easy task. Measurements with thermoluminescence dosimeters (TLD) are well suited for dose measurements over a wide dose range. The variation in response with radiation energy of the TLD measurements is corrected by an energy-dependent calibration factor. In radiotherapy, this correction factor is usually obtained from Monte Carlo simulations of the photon energy spectra in the patient [5, 6]. The disadvantage of this method is that it relies on simulation of the expected photon energy spectra.

The aim of this study was to develop a double-TLD unit consisting of the well-studied [6–13] LiF:Mg,Ti (TLD100, Thermo Fisher Scientific, Waltham, MA) and LiF:Mg,Cu,P (TLD100H) chip. As the response with radiation energy of both TLDs are different due to the anomaly of TLD100H [14], an estimate of the mean photon energy is possible by the analysis of the ratio of the TLD100 to TLD100H readout. The dose is then determined by applying an energy correction which is a function of the ratio of both TLD readouts.

Gorbics et al. [15] and others [16–18] presented a method to determine the photon energy by using different types of TLDs with a non-linear energy response. Nelson et al. [18] suggested not to use TLD100 because of the low sensitivity to photons.

Instead, the authors used the dose ratio of TLD100H with other TLD materials showing large gradients in response with radiation energy. The advantage of their method is the large dose ratios of the various TLD types (up to 160) which increase the precision in energy discrimination.

There are mainly five reasons why a combination of TLD100 and TLD100H was used for simultaneous energy and dose measurements although the LiF-TLDs show a small variation in response with radiation energy relative to other types of TLDs. (1) LiF-TLDs are tissue-equivalent in terms of radiation. They will disturb the radiation field not as much as TLDs consisting of a higher Z material would do. This fact is important since a TLD100H was placed on top of a TLD100 for simultaneous energy and dose measurement. (2) As the main aim with respect to energy determination in this work was to increase the accuracy of the dose measurements, it is beneficial to use TLDs showing a small variation in response with radiation energy. Therefore, the error of the energy evaluation has a smaller impact on the accuracy of the dose determination. (3) By using a combination of tissue equivalent TLD100 and TLD100H, both energy-corrected measurements can be used for dose determination enabling a more precise result. (4) There is a lack of literature for the relative response of TLDs for energies between 0.25 MeV and 0.6 MeV [7, 15, 17–21]. However, this is the energy interval expected for a linear accelerator in the out-of-field region [5, 6]. Hence, a small gradient in response with radiation energy is of advantage since it is more robust for a interpolation as compared to an interpolation involving large gradients. (5) The response with radiation energy of TLD100 and TLD100H was taken from the literature [7, 21, 22]. The researchers determined the response as a function of the mean photon energy. The mean energies were calculated from the spectra of the photon irradiations used for calibration. A difference in the shape of the spectrum between the calibration and a field measurement can lead to a systematic error even if the mean energies of the spectra are the same. As smaller the gradient of the response is changing, as smaller are the systematic errors in dose and energy determination. The response ratio with radiation energy of TLD100 divided by TLD100H shows the smallest change in gradient compared to the suggested TLD type combinations from the literature [15–18]. Hence, the systematic error is smaller by using the TLD100/TLD100H ratio compared to the suggested combination from the literature.

To enable a faster work-flow and protect the TLD100 crystals a different thermal treatment compared to the literature was chosen. It contained a more conservative annealing at 270 °C instead of 400 °C and no low temperature annealing. Duggan et al. [21] investigated the response with radiation energy for different thermal treatment procedures of TLD100 and TLD100H. They found that TLDs of one doping show the same response with radiation energy for different thermal treatments. The response with radiation energy of the TLDs was taken from Davis et al. [7]. They used linear heating of the TLDs for the readout compared to an isothermal readout presented in this manuscript. However, Kron et al. [20] used an isothermal readout to investigate the response with radiation energy of LiF:Mg,Ti and LiF:Mg,Cu,P. For the investigated photon spectra in the energy range of interest (0.06-1.2 MeV) the dose-to-water response with radiation energy evaluated by Kron et al. [20] deviates less than 9 % compared to the values of Davis et al. [7]. A comparison between the response with radiation energy was made for the thermal treatment used by Davis et al. [7] and the thermal treatment used in this work.

In this manuscript, the type B uncertainty of the double-TLD unit in determining the dose and mean energy was calculated. The accuracy for in- and out-of-field dose measurements of external radiotherapy was evaluated by an end-to-end measurement. Furthermore, the ability of the double-TLD unit to determine the mean energy for external radiotherapy, X-ray sources and brachytherapy was tested.

II. METHODS AND MATERIALS

A. Double-TLD unit

1. *Detector calibration*

A double-TLD unit consisting of TLD100 and TLD100H was used for simultaneous dose and energy measurements. All TLD discs were marked with a pencil dot to keep orientation for the readout. TLDs were calibrated with a nominal beam energy of 6 MV. The beam was applied with a linear accelerator of the type TrueBeam or Clinac iX (Varian Medical Systems, Palo Alto, CA, USA). Both machines showed the same mean photon energy of 1.5 MeV for the calibration beam. A $25 \times 25\,\mathrm{cm}^2$ open field (MLC retracted) irradiated on a $30 \times 30 \times 21\,\mathrm{cm}^3$ RW3-slab phantom resulted in a flat dose profile at the isocenter with a dose variation of ±1 % (2σ) [23]. The isocenter was located in a phantom depth of 14.7 cm [100 cm source isocenter distanced (SID)]. According to the distributor (PTW, Freiburg, Germany), the RW3 phantom mimics water equivalence for photons in the energy range of ^{60}Co to 25 MeV. In batches consisting of PMMA casings, up to 50 TLD chips were irradiated (front face) in the primary field. The TLDs were distributed in the casings such that each TLD100 was next to a TLD100H chip. These neighboring chips received the same calibration dose and constituted a double-TLD unit. The calibration was done with three different doses (see Table I). The PMMA batches were placed in a rectangular cutout centered in the middle of two RW3-slabs. For calibration, the slabs containing the PMMA batch were placed below 14 and above 5 RW3-slabs such that the TLDs were located in a depth of 14.7 cm along the central field axis (CAX) facing the beam. The slabs which contained the batch could be exchanged by a 2 cm thick solid slab containing a hole for an ionization chamber (IC). In the same depth at which the TLDs were positioned, the dose was registered by a Rigid Stem IC (30016, PTW, Freiburg, Germany). In addition, a reference chamber (Semiflex, 32013, PTW) was installed in the last two slabs along the CAX. The

Rigid Stem chamber was cross-calibrated to the Semiflex chamber by three measurements for each calibration dose (Table I). This way, every irradiated batch could be related to the absolute received dose via the reference chamber. The calibration and readout were done once before and once after a field measurement resulting in a unique calibration for each TLD.

TABLE I. Technical data for TLD readout by the Fimel PCL3 isothermal automatic TLD reader used in this work. The three dose ranges, various filter and photo multiplier (PM) voltage combinations prevented an amplification change of the TLD reader.

Harshaw (diameter: 4.5 × 0.6 mm)	TLD100			TLD100H		
Dose range name	Small	Middle	High	Small	Middle	High
Calibration dose (mGy)	~ 8	~ 45	~ 500	~ 8	~ 45	~ 500
Range (mGy)	1.0-13	8-130	50-2400	1.0-13	8-130	50-2400
Filter	Blue	Small grey	Big grey	Small grey	Big grey	Small & Big grey
PM voltage (V)	890	875	825	900		

2. *Thermal treatment*

With a microprocessor-controlled oven (Fimel ETT Annealing Oven, PTW, Freiburg, Germany), up to 80 TLDs at once were annealed in a metallic container before irradiation. Using a heating gradient of $\sim 300\,^\circ\mathrm{C/min}$ the TLDs were annealed according to Table II. After annealing, the metal container instantaneously slid on a big aluminum block with a smoothed surface to cool down to room temperature. The aluminum block was air-cooled by a large fan. The rapid cooling of the TLDs enhanced the sensitivity to ionizing radiation [24]. No low temperature anneal was used for TLD100 in order to prevent a sensitivity decrease [10].

The majority of the data points for the TLD100 and TLD100H response with radiation energy was taken from Davis et al. [7]. In agreement to our work, TLD100 and TLD100H were shock-cooled after each annealing step. In contrast to our work, the TLDs were cooled on a big brass block instead of an aluminum block. Further differences in the two thermal treatments for TLD100 can be seen in Table II.

TABLE II. The annealing procedures for the two differently doped TLD types. After each annealing step the TLDs were shock-cooled to room temperature on an aluminum block.

Identifier	TLD100 (This work)	TLD100$_{400\,^\circ\mathrm{C}}$ (Davis et al. [7])	TLD100H
Annealing	60 min at 270 °C	60 min at 400 °C followed by 120 min at 100 °C	30 min at 240 °C
Preheating	15 min at 75 °C	12 min at 100 °C	10 min at 90 °C

3. *Detector readout*

In the Fimel annealing oven, the TLDs were preheated in batches before readout (see Table II). The glow curves of the investigated TLDs showed a multiple peak-structure. The first glow peak disappeared from the readout curve due to preheating (illustrated in Fig. 1). The metal container slid on an aluminum block to cool down to room temperature after preheating.

A Fimel PCL3 isothermal automatic TLD reader (PTW, Freiburg, Germany) with isothermal heating zone was used for the readout of the detectors. The TLDs were placed in small metal containers and were stacked in an automatic loading device for readout. Each TLD was always placed in the same metallic container for multiple readouts to guarantee the same heating-curve on the isothermal heating zone operated at 240 °C. With a photo multiplier (PM), the emitted light of each TLD was measured in terms of charge integration. The PCL3 reader uses four levels to amplify the PM signal depending on the detected charge per time. With optical filter combinations and adjustments of the PM voltage, the amplification of the TLD signal were kept in the first (the highest) level. This was done to avoid an additional error caused by the amplification

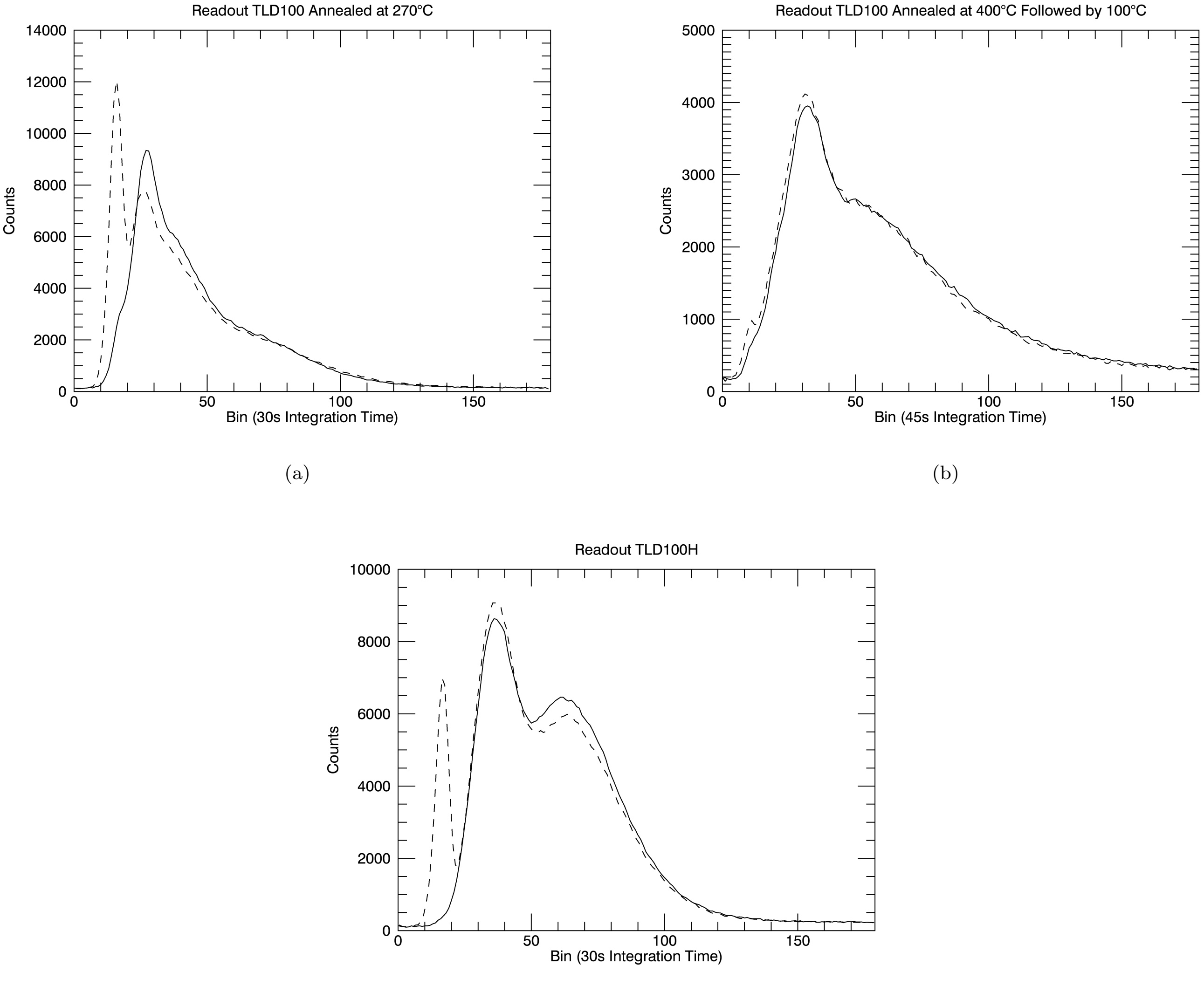

(a)

(b)

(c)

FIG. 1. Isothermal heating curve without (dashed line) and with preheating (solid line), for (a) TLD100 annealed at 270 °C, (b) TLD100 annealed at 400 °C followed by 100 °C, and (c) TLD100H. The difference between the main peaks in (a) is caused by an amplification change of the reader for the TLD readout without pre-heating.

change. The combinations of the optical filters and the PM voltage for the readout of TLD100 and TLD100H can bee seen in Table I.

4. Dose determination

To calculate the dose, an individual detector calibration for each TLD was made before and after a field measurement. The measured dose-to-water D_{meas} for one TLD was determined as follows,

$$\begin{aligned} D_{meas} &= \left\{ \left(\frac{D_{before}/c_{before} + D_{after}/(c_{after} \cdot K^c_{batch})}{2} \right) \cdot c_{meas} \cdot K^m_{batch} - D_{background} \right\} \cdot K_{absorption} \cdot K_{energy} \\ &=: D_{uncor} \cdot K_{energy}, \end{aligned} \tag{1}$$

where $D_{before,after}$ are the calibration doses before and after the measurement, respectively. $D_{before,after}$ were determined by an IC. $c_{before,after}$ are the integrated PM counts from the calibration readouts corresponding to one TLD. The integrated charge from the field measurement readout is indicated by c_{meas}. The signals $c_{before,after}$ and c_{meas} were corrected for dark current detected by the PM.

A systematic shift in response of all TLDs in a batch was noticed for two repeated calibration cycles. This shift of the mean of the first calibration (prior to the field measurement) to the second calibration (posterior) could be corrected with K^{c}_{batch}. Hence, the sensitivity of the TLDs to radiation due to variation in cooling after annealing and due to response changes for repeated readouts was corrected by K^{c}_{batch}. Furthermore, the correction for the PM output fluctuation per readout is included in K^{c}_{batch}. This systematic shift occurred also for the measurement and was corrected by K^{m}_{batch}. For the field measurement cycle, at least four TLD100s and four TLD100Hs per batch ('shift-TLDs') were irradiated according to the calibration protocol. For each 'shift-TLD', the resulting ratio of dose per PM counts D_{meas}/c_{meas} was compared to the individual mean of the ratios D_{before}/c_{after} and $D_{after}/(c_{after} \cdot K^{c}_{batch})$ of the two calibration cycles. The mean deviation of the four 'shift-TLDs' to the calibration cycles resulted in K^{m}_{batch}.

$D_{background}$ is the dose registered by the TLDs due to background radiation. Mostly, the time interval between the irradiation and the readout was below several days such that no background correction had to be applied. For one measurement [MRIdian (ViewRay, Oakwood Village, OH, USA)], the TLDs were transported in an airplane such that a background correction was essential. Six TLD100s and four TLD100Hs were irradiated according to the protocol of the smallest dose range (Table I). The background TLD readouts were done with a PM voltage of 900 V and without an optical filter. This readout procedure enabled the biggest possible counts per TLD but induced an amplification change of the PM which led to an additional error.

The double-TLD unit consisted of a TLD100 and TLD100H chip. For the measurement, the TLD100H was put on top of the TLD100. This arrangement could lead to a dose difference between the TLD100H compared to the TLD100. $K_{absorption}$ is dependent on the radiation energy and corrected for the dose differences between the two TLDs. By stacking two TLD100H, $K_{absorption}$ was determined by the dose ratio of the lower divided by the higher TLD100H dose. Furthermore, $K_{absorption}$ corrected for the dose difference caused by the inverse square law.

Both TLD types show a variation in response with radiation energy as can be seen in Fig. 2. The variation in response to different photon energies was corrected by K_{energy}. The determination of K_{energy} with the double-TLD method is described in Section II A 5.

D_{uncor} is the dose not corrected for the variation in response with radiation energy. Hence, for a conventional in-field measurement D_{uncor} represents the individual TLD dose.

The final dose of one double-TLD unit D_{final} was calculated with the mean of the corrected TLD100 dose $D_{meas,100}$ and the corrected TLD100H dose $D_{meas,100H}$.

The ranges of the values for the correction factors used in this work are listed in Table III.

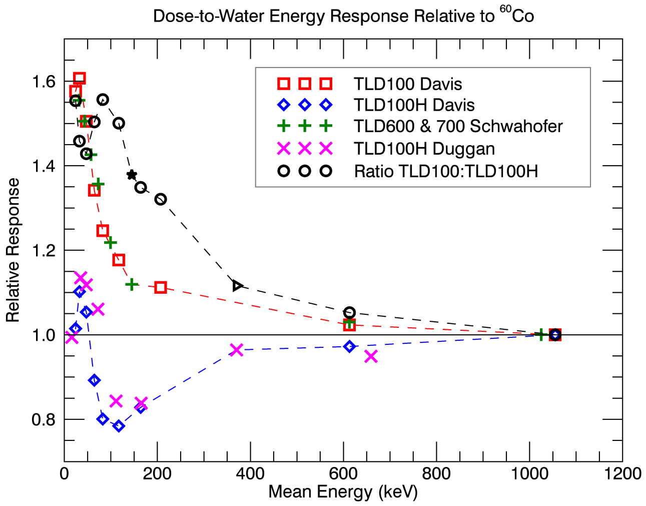

FIG. 2. TLD100, TLD600, TLD700 and TLD100H response with radiation energy relative to a mean photon energy of ^{60}Co . The air-kerma-based response values of Davis et al. [7] and Duggan et al. [21] were converted to dose-to-water via mass attenuation coefficient ratio of air-to-water. The circles represent the relative response ratio TLD100/TLD100H. The star at 145 keV and the triangle at 370 keV were determined with the response data from Schwahofer et al. [22] and from Duggan et al. [21], respectively. The data points from Duggan et al. [21] below 370 keV are given for the effective energy. To determine the mean energy and K_{energy}, a linear interpolation was made along the dashed lines.

TABLE III. Ranges of the correction factors used for this work.

K_{batch}	K_{energy} TLD100	K_{energy} TLD100H	$K_{absorbtion}$
0.96-1.04	0.66-1.00	0.95-1.25	0.99-1.99

5. *Mean energy determination*

The response with radiation energy compared to ^{60}Co for TLD100 and TLD100H is shown in Fig. 2 and Table IV. Furthermore, the relative response ratio between TLD100 and TLD100H is displayed as a function of the mean energy. For ^{60}Co a mean photon energy of 1055 keV at the point of measurement was simulated by Davis et al. [7]. To determine the photon energy of a measurement, the TLD100 dose was divided by the TLD100H dose. Both doses were derived from Eq. 1 without a K_{energy} correction. The energy was determined by a linear interpolation of the TLD100/TLD100H dose ratio with the energy response curve (Fig. 2). Using the resulting energy, both correction factors K_{energy} for TLD100 and TLD100H were calculated. A simple linear interpolation was used to determine K_{energy} because there is a lack of mechanistic understanding of the response with radiation energy of TLD100 and TLD100H. We believe that a linear interpolation is justified since the number of response points is increasing with response gradients (see Fig. 2). For energy determination a TLD100 was attached to a TLD100H. The change in the energy spectrum caused by the attached TLD was neglected since both TLD typs were only 0.6 mm thick.

TABLE IV. Relative response with radiation energy of the differently doped TLDs normalized to ^{60}Co. All air-kerma-based values [7, 21] were converted to dose-to-water via mass attenuation ratio of air to water. The data corresponding to 145 keV and 370 keV were taken from Schwahofer et al. [22] and Duggan et al. [21], respectively. * represents the data point determined with TLD600 and TLD700. A linear interpolation was made between the data points for energy and dose determination.

Energy (keV)	$1/K_{energy}$ TLD100 (TLD600 & 700)*	$1/K_{energy}$ TLD100H	Ratio $\frac{D_{uncor,100}}{D_{uncor,100H}}$
24	1.58	1.01	1.55
33	1.61	1.10	1.46
47	1.51	1.05	1.43
65	1.34	0.892	1.50
83	1.25	0.800	1.56
117	1.18	0.784	1.50
145	1.12*	–	1.38
164	–	0.842	1.35
207	1.11	–	1.32
370	–	0.964	1.12
613	1.02	0.972	1.05
1055	1.00	1.00	1.00

The response as a function of the mean energy of TLD100 and TLD100H was taken from the literature [7, 21, 22]. In these papers, the mean energy was calculated using the calibration spectrum of the photon irradiation. A difference in the spectrum of a field measurement compared to the calibration spectrum can lead to a systematic error in energy determination. This systematic error can be minimized by using a detector showing a small change in gradient for the response with radiation energy. In this manuscript, the measured mean energy is defined as the value resulting from the linear interpolation of the TLD100/TLD100H dose ratio with the energy response curve (Fig. 2), which is assumed in first approximation to be the mean energy of the applied spectrum.

Dependent on radiation energy TLD100 shows supralinearity above a gamma dose level of 1.0 Gy [25], whereas TLD100H is linear up to 10 Gy [20, 26, 27]. Unless otherwise stated, the mean photon energy of an irradiation was determined for dose levels below 1.0 Gy.

6. *Uncertainty estimation*

The difference in TLD response between the calibration beam (mean energy 1.5 MeV [5]) and the ^{60}Co sources (mean energy 1.1 MeV [7]) was neglected. This difference in response is around 1 % [5].

The type B uncertainties in energy and dose of one double-TLD unit were calculated using Gaussian error propagation (Table V). For the calculation the same uncertainty of ±2 % at the two standard deviation level (2σ) was assumed for the uncorrected TLD100 and TLD100H dose (D_{uncor} in Eq. 1). $K_{absorption}$ introduced in Eq. 1 corrects for a systematic error caused by two stacked TLDs. This correction factor was determined using multiple measurements for each experiment. Hence, the random error induced by $K_{absorption}$ was neglected for the estimation of uncertainty.

TABLE V. The linear equations to calculate the final dose of one double-TLD unit D_{final} and the corresponding uncertainties. $m(E)$ refers to the gradient and $c(E)$ to the intercept of the linear functions corresponding to the energy intervals plotted in Fig. 2. The subscripts $_R$ and $_I$ identify the relative response ratio curve TLD100/TLD100H and the individual response curves of TLD100 or TLD100H, respectively. For TLD100 and TLD100H the same uncertainty $\sigma_{D_{uncor},rel}$ of ±2 % was assumed.

$Energy = \left(\frac{D_{uncor,100}}{D_{uncor,100H}} - c_R(E)\right) \cdot m_R(E)^{-1}$	$\sigma_{Energy} = \frac{D_{uncor,100}}{D_{uncor,100H}} \cdot m_R(E)^{-1} \cdot \sqrt{2}\sigma_{D_{uncor},rel}$
$K_{energy,I} = \Big(m_I(E) \cdot E + c_I(E)\Big)^{-1}$	$\sigma_{K_{energy,I},rel} = m_I(E) \cdot \Big(m_I(E) \cdot E + c_I(E)\Big)^{-1} \cdot \sigma_{Energy}$
$D_{meas,I} = D_{uncor,I} \cdot K_{energy,I}$	$\sigma_{D_{meas,I},rel} = \sqrt{\sigma^2_{K_{energy,I},rel} + \sigma^2_{D_{uncor,I},rel}}$
$D_{final} = (D_{meas,100} + D_{meas,100H})/2$	$\sigma_{D_{final},rel} = \frac{1}{2}\sqrt{\sigma^2_{D_{meas,100},rel} + \sigma^2_{D_{meas,100H},rel}}$

B. Experiments

1. *Accuracy in dose of the double-TLD unit for external radiotherapy*

The accuracy and type A standard uncertainty of the double-TLD unit was determined by an end-to-end measurement. A $10 \times 10\,\mathrm{cm}^2$ open field (MLC retracted, Gantry 270 °, table 0 °) was irradiated on a $30 \times 30 \times 62\,\mathrm{cm}^3$ RW3-slab phantom using a nominal beam energy of 6 MV. The dose was measured by a Farmer chamber (30013, PTW, Freiburg, Germany) at three positions in-and out-of-field (see Table VI). The chamber-containing slabs were replaced by the PMMA-holder slabs (see Section II A 1) containing two double-TLD units. At the same positions as for the chamber measurements the dose was determined multiple times by double-TLD units. The set-up mimicked the whole-body dose measurements of treatment plans using an adult anthropomorphic Alderson Rando phantom.

The relative response with radiation energy of TLD100 was taken from Davis et al. [7]. They used a thermal treatment for TLD100 (identifier: $\mathrm{TLD100}_{400\,^\circ\mathrm{C}}$) which was different to the thermal treatment used in this work (see Table II). The accuracy in detecting the dose between the two thermal treatments was investigated. At each chamber measurement location shown in Table VI, four to six $\mathrm{TLD100}_{400\,^\circ\mathrm{C}}$, TLD100 and TLD100H were irradiated individually. According to Eq. 1, the dose was calculated for the single TLDs without K_{energy} and the need to correct for $K_{absorption}$. The mean of the TLD doses at one chamber measurement location was corrected with K_{energy}. K_{energy} was calculated by using the mean TLD100H dose either combined with the mean $\mathrm{TLD100}_{400\,^\circ\mathrm{C}}$ dose or combined with the mean TLD100 dose.

The fading effect of TLD100 was investigated. A set of twelve TLD100 was calibrated in the smallest dose range and annealed according to Table I. Three days post annealing, the TLD received a in-field dose of 8.0 mGy. The readout of the TLDs was done three days after irradiation. The post calibration was done right away. Without correcting for K_{batch}, the dose was determined according to Eq. 1.

2. *Mean energy determination in external radiotherapy*

The energy measurements of external radiotherapy were compared to the MC simulations preformed by Kry et al. [5]. For the same set-up as described by Kry et al. [5], the mean energy was determined for different distances to the CAX by the double-TLD unit. A $10 \times 10\,\mathrm{cm}^2$ open field (MLC retracted, Gantry 90 °, table 0 °) was irradiated (6 MV nominal beam energy) with a Clinac iX on a $30 \times 30 \times 90\,\mathrm{cm}^3$ RW3-slab phantom (SSD 100 cm). At a depth of 3.7 cm in the phantom, the dose was measured at 10 cm, 30 cm, and 50 cm distance from the CAX in the direction toward gun. The applied MUs corresponded to a dose of around 10 mGy. Energy was determined by using the TLD100 and the TLD100H dose evaluated by Eq. 1 without K_{batch} and K_{energy} correction. By neglecting K_{batch}, the uncertainty in dose for the single TLDs was increased from ±2 % to ±3 %.

In a further experiment, the difference in response with radiation energy of $\mathrm{TLD100}_{400\,^\circ\mathrm{C}}$, TLD100, and TLD100H was compared to MC simulations made by Scarboro et al. [6] and Kry et al. [5]. The measurement set-up is shown in Table VI. The response with radiation energy of the different TLDs was found by dividing the dose measured by the TLDs and the dose measured by the IC. According to the specifications, there is no variation in dose-to-water response with radiation energy of the IC in the energy interval expected (0.2-1.5 MeV). Hence, the response with radiation energy of the IC could be neglected for the mean energy determination.

Lastly, the mean photon energies for external radiotherapy were determined at 151 out-of-field points in an adult anthropomorphic Alderson Rando phantom. The double-TLD units (consisting of a TLD100 and TLD100H chip) were equally distributed in the phantom according to Hälg et al. [23]. The orientation of the TLDs relative to the beam was the same

TABLE VI. The set-up for measuring the accuracy and type A standard uncertainty of the double-TLD unit. Furthermore, the set-up for measuring the difference in response with radiation energy between TLD100$_{400\,^{\circ}\mathrm{C}}$ and TLD100. 'Distance from isocenter' indicates the distance the treatment table was moved toward gun compared to the in-field measurement. Also presented, the orientation of the TLDs toward the gantry head and the quantity of TLDs of one type used per measurement. Only measurements up to 30 cm from the isocenter were conducted due to the limited sensitivity of the ionization chamber.

Distance from isocenter	Depth in phantom	MLCs	Dose measured	Orientation	Quantity
Calibration					
In-field	14.7 cm	Retracted		Front facing gantry	
End-to-end measurement					
In-field	15.0 cm	Retracted	50 to 2300 mGy	Edges facing gantry	11
15 cm	15.0 cm	Retracted	8 to 130 mGy	Edges facing gantry	8
30 cm	15.0 cm	Retracted	1 to 13 mGy	Edges facing gantry	7
Comparison between dose determination TLD100$_{400\,^{\circ}\mathrm{C}}$ and TLD100					
In-field	15.0 cm	Retracted	480 mGy	Edges facing gantry	6
10 cm	3.7 cm	Retracted	44.9 mGy	Front facing gantry	4
15 cm	15.0 cm	Retracted	44.3 mGy	Edges facing gantry	6
15 cm	15.0 cm	Jaws defined by MLCs	7.55 mGy	Edges facing gantry	5
30 cm	15.0 cm	Retracted	7.53 mGy	Edges facing gantry	6

as for the end-to-end dose measurement (edges of the TLD-chips facing the gantry head). Three different treatment plans of a rhabdomyosarcoma in the prostate [3D-conformal radiation therapy (3DCRT), IMRT, and VMAT] were irradiated with a TrueBeam operated at a 6 MV nominal beam energy. The 3DCRT plan was irradiated using a four field box, the IMRT plan using five fields with dynamic MLCs, and the VMAT plan using one arc. Furthermore, an IMRT treatment plan (16 fields) for the same indication was measured using the MRIdian system (Cobalt machine combined with an MRI device). All used treatment plans were based on common planing guidelines [23]. The mean energies were evaluated by the TLD doses determined using Eq. 1 without K_{batch} and K_{energy} correction.

3. *Mean energy determination in brachytherapy*

The mean energy of two well-known brachytherapy sources was investigated. A TLD100H on top of a TLD100 followed by two stacked TLD100H were placed in a PMMA holder. The four TLDs facing the source were irradiated with ~ 8 mGy by ^{137}Cs. The source to TLD distance (7 cm) was covered with PMMA material. The same measurement was repeated with ^{192}Ir for a double-TLD unit to source distance of 9 cm and 12 cm. The dose of the single TLDs was calculated by Eq. 1 with one calibration (after the measurement), and no K_{batch} and K_{energy} correction. $K_{absorbtion}$ was determined from the dose ratio of the two stacked TLD100Hs. Thus, $K_{absorbtion}$ included the dose decrease ($< 2.5\,\%$) caused by the inverse square law.

4. *Mean energy determination for X-ray sources*

The ability of the double-TLD unit to predict the mean energy for X-ray imaging was tested using the on-board cone beam CT (CBCT) of the TrueBeam linear accelerator. At 152 in- and out-of-field locations in the Alderson phantom the mean energies were determined for two different pelvis CBCT protocols given by the vendor [(half fan type, full trajectory, 125 kV$_{\mathrm{p}}$, 1080 mAs) and (full fan type, half trajectory, 125 kV$_{\mathrm{p}}$, 750 mAs)]. The CBCTs were irradiated multiple times to apply a dose of at least 1 mGy anywhere in the phantom. The orientations of the double-TLD units were the same as for the treatment plan measurements (see Section II B 2). To evaluate the mean energies, the resulting TLD100/TLD100H dose

ratios were interpolated between the ratios corresponding to 47-83 keV (Table IV).
In a last experiment, the mean energy of a Faxitron RX-650 (Faxitron X-Ray Corporation, Lincolnshire, IL, USA) was measured. This 130 $\mathrm{kV_p}$ unit (5 mA, 0.5 mm Al filtration) is used in biology laboratories to irradiate cell cultures. For each of the 25 measurements with and without Petri dish, a TLD100H was placed on top of a TLD100. Between 0.1 Gy and 0.7 Gy of dose was irradiated in around 15 s. The mean energy was evaluated by using the TLD100 and TLD100H dose determined according to Eq. 1 without correcting for K_{batch}.

III. RESULTS

Unless otherwise stated, the arithmetic mean and the 95 % confidence interval (2σ) are presented.
The air-kerma-based values from Davis et al. [7] were converted to dose-to-water via mass attenuation ratio of air-to-water (Fig. 2). The converted values deviated by 0 % ± 5 % from the LiF:Mg,Ti dose-to-water response measured by Schwahofer et al. [22].

A. Uncertainty estimation

In Table VII the calculated uncertainties in energy and dose determination for one double-TLD unit is presented. The values were calculated for the energy intervals shown in Fig. 2 using the equations presented in Table V. The evaluation was based on the assumption of a ±2 % uncertainty for an in-field dose determination. Compared to an IC, the individual in-field dose (front face irradiation) of TLD100 and TLD100H could be measured to 0.0 % ± 2.1 % and −0.4 % ± 2.0 %, respectively. Hence, the assumption of $\sigma_{D_{uncor},rel} = \pm 2\,\%$ was justified.
The uncertainty in energy decreased with increasing gradient of the relative response ratio TLD100/TLD100H (m_R see Table VII). A smaller gradient of the individual relative responses with radiation energy of TLD100 and TLD100H (m_I) led to a smaller uncertainty in dose for a double-TLD unit. The calculated uncertainty in dose was below ±3 % for energies down to 0.12 MeV (Table VII).

TABLE VII. The calculated type B uncertainty for one double-TLD unit. The values represent the 95 % confidence interval calculated using Table V.

Energy interval (keV)	m_R (1/1000 keV)	$2\sigma_{Energy}$ (keV)	$2\sigma_{D_{final},rel}$
24-33	+11.5	±4	±3 %
33-47	−2.01	±20	±12 %
47-65	+4.37	±9	±8 %
65-83	+2.93	±15	±6 %
83-117	−1.63	±27	±4 %
117-145	−4.37	±9	±2 %
145-164	−1.56	±25	±2 %
164-207	−0.651	±58	±2 %
207-370	−1.25	±28	±3 %
370-613	−0.263	±117	±2 %
613-1055	−0.119	±245	±2 %

B. Dose accuracy for external radiotherapy

The determined in- and out-of-field doses from the end-to-end measurement (see Table VI) showed an overall deviation of −0.6 % ± 2.0 % compared to the IC. The eleven evaluations of the highest dose range showed a deviation of −0.8 % ± 2.2 %, the eight evaluations of the middle dose range a deviation of −0.8 % ± 1.8 % and the seven evaluations of the smallest dose range a deviation of −0.2 % ± 1.8 %. The experimentally evaluated uncertainties in dose were in good agreement with the calculated uncertainties (±2 %, see Table VII). TLD100 showed an over-response of 3 % for the in-field irradiation of 2.3 Gy. This systematic error caused by the supralinear response of TLD100 was balanced by the double-TLD method. The final determined dose by the double-TLD unit for the irradiation of 2.3 Gy deviated less than 1 % compared to the IC measurement. Two calibration cycles of $\mathrm{TLD100}_{400\,^\circ\mathrm{C}}$ showed a variation of ±3 %. Therefore, an uncertainty in dose of ±3 % was assumed for $\mathrm{TLD100}_{400\,^\circ\mathrm{C}}$. The difference in measuring the dose between $\mathrm{TLD100}_{400\,^\circ\mathrm{C}}$, TLD100 and TLD100H is plotted in Fig. 3(a). In-field, the $\mathrm{TLD100}_{400\,^\circ\mathrm{C}}$ underestimated the dose compared to the IC by −3.2 %. $\mathrm{TLD100}_{400\,^\circ\mathrm{C}}$ and TLD100 showed a significant difference ($\alpha = 5\,\%$) in response in the out-of-field region except for the measurement where the TLD front faced the gantry (see Table VI). Furthermore in Fig. 3(a), the K_{energy} corrected mean dose is plotted. Compared to the IC the corrected dose calculated by the TLD100$_{400\,^\circ\mathrm{C}}$ and TLD100H showed a deviation of $-3.5\,\% \pm 2.0\,\%$ over the five measurement locations. In comparison, the corrected dose calculated by the TLD100 and TLD100H showed a deviation of $-0.8\,\% \pm 1.9\,\%$. No remaining dose was noticed for the readout of annealed TLD100$_{400\,^\circ\mathrm{C}}$, TLD100 or TLD100H.

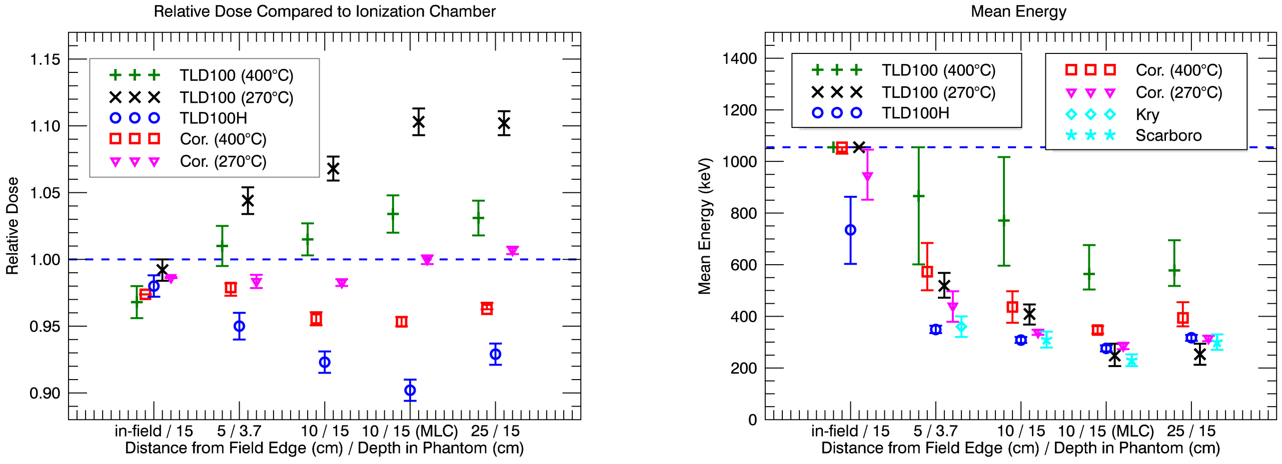

(a)

(b)

FIG. 3. (a) Dose determined by the TLDs divided by the dose measured with the ionization chamber. Cor. indicates the mean of the doses corrected by the individual $K_{energy,I}$ values. Furthermore, the uncorrected mean TLD100H, TLD100, and TLD100$_{400\,^\circ\mathrm{C}}$ dose. The error bars represent two standard uncertainties (type B) of the mean ($2\sigma/\sqrt{n}$). The 2σ values of the individual TLDs were propagated to the Cor. values. (b) The corresponding mean energies and uncertainties for the determined doses in (a). Furthermore, the simulations from Kry et al. [5] and Scarboro et al. [6] with error bars (2σ) based on the estimated statistical uncertainties. The dashed line in (b) indicates the maximum resolvable mean energy by the double-TLD unit.

Using preheating and no K_{batch} correction, TLD100 showed no fading effect. The determined dose after three days post irradiation deviated to the Rigid Stem chamber by $-1.1\,\% \pm 2.3\,\%$.

C. Mean energy determination in external radiotherapy

The MC simulations by Kry et al. [5] and the measured mean energies using the double-TLD unit for different distances to the CAX are listed in Table VIII. The experimentally determined energies were in good agreement with the simulated energies. The increase of the mean energy with increasing distance from the CAX could be observed for the measurements as well for the simulations. The measured uncertainties in energy of the double-TLD units (Table VIII) were in line with the calculated uncertainties (Table VII). An increase in the uncertainties with increasing energy was observed experimentally as well as theoretically.

TABLE VIII. For a 6 MV nominal beam energy, the mean photon energy in the out-of-field region simulated by Kry et al. [5] and measured in this work. Seven double-TLD units were used per energy. For the measurement the uncertainty (type A) of the mean ($2\sigma/\sqrt{7}$) and for the simulations the statistical uncertainties (2σ) are shown.

Distance from CAX	MC simulation	Measured	Difference
10 cm	(0.36 ± 0.04) MeV	$(0.34 \pm \frac{0.03}{\sqrt{7}})$ MeV	(0.02 ± 0.04) MeV
30 cm	(0.39 ± 0.10) MeV	$(0.37 \pm \frac{0.05}{\sqrt{7}})$ MeV	(0.02 ± 0.10) MeV
50 cm	(0.41 ± 0.02) MeV	$(0.43 \pm \frac{0.11}{\sqrt{7}})$ MeV	(-0.02 ± 0.05) MeV

In Fig. 3(b), the mean energies determined for TLD100$_{400\,^\circ\mathrm{C}}$, TLD100, and TLD100H are shown. The mean energies determined by dividing the TLD100$_{400\,^\circ\mathrm{C}}$ by the IC measured dose were overestimated compared to the published MC simulations by 0.27-0.50 MeV. However, the overestimation was reduced to 0.09-0.21 MeV by determining the energies with the TLD100$_{400\,^\circ\mathrm{C}}$/TLD100H ratio. The four mean energies determined by the TLD100/IC, TLD100H/IC, and TLD100/TLD100H dose ratios deviated compared to the MC simulations by (-0.06 ± 0.08) MeV, (-0.01 ± 0.02) MeV, and

(-0.04 ± 0.03) MeV (uncertainty of the mean $2\sigma/\sqrt{n}$), respectively. Hence, they were in good agreement with the MC simulations.

For the MRIdian measurement (TLDs transported in an airplane), a background dose of (0.063 ± 0.008) mGy and (0.042 ± 0.002) mGy (uncertainty of the mean $2\sigma/\sqrt{n}$) was determined from the six TLD100 and four TLD100H, respectively. In addition to the uncertainty of the measurement, an error of ±5 % was assumed. This additional error was caused by the amplification change of the TLD reader for the calibration procedure without filter. For all treatment plans, an out-of-field $K_{absorption}$ correction factor of 1.01 was used for TLD100. The measured mean energies were averaged in each Alderson slice and are plotted in Fig. 4 as a function of distance to the isocenter. Close to the field edge, the VMAT plan showed the highest and the 3DCRT the lowest mean photon energy. Up to around 20 cm from the isocenter, all measured treatment plans showed a decrease of the mean energy. For the plans measured with the TrueBeam, the mean photon energy slightly increased to 0.4 MeV from around 20 cm up to 85 cm isocenter distance. The 3DCRT plan showed the most dominant increase in energy. The mean photon energy measured for the MRIdian plan increased from 20 cm up to 40 cm before it started to decrease to 0.3 MeV. In Fig. 5, the TLD100 and TLD100H dose of the 3DCRT plan is plotted without energy correction relative to the dose determined by the double-TLD unit. The largest energy correction (K_{energy}) was 0.91 and 1.13 for TLD100 and TLD100H, respectively.

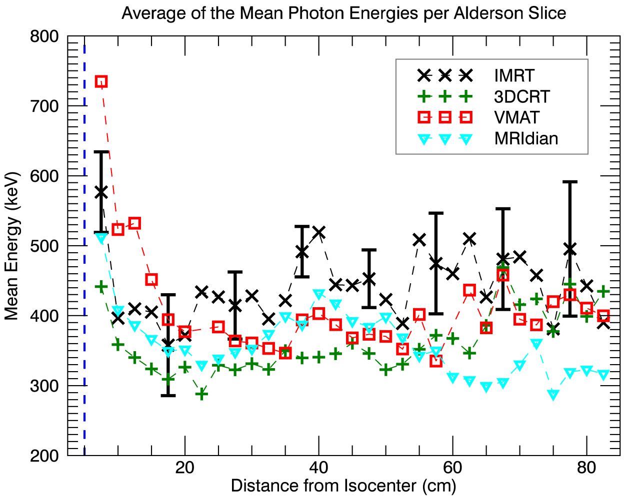

FIG. 4. Out-of-field measured mean energies (averaged per Alderson slice) for 6 MV treatment plans and a ^{60}Co irradiation (MRIdian). The vertical dashed line represents the field edge. The error bars represent two standard uncertainties (type B) of the mean $(2\sigma/\sqrt{n})$ per Alderson slice with $\sigma = 0.14$ MeV.

D. Mean energy determination in brachytherapy

The published MC simulations and the measurements of the mean energy for brachytherapy sources can be seen in Table IX. For ^{137}Cs the measured mean energy was in good agreement with the simulation. For lower brachytherapy energies of 0.2 MeV, the double-TLD method overestimated the mean energy by 0.1 MeV. The mean energy simulations of ^{192}Ir by Meli et al. [28] were in agreement with other simulations [29]. $K_{absorbtion}$ was determined with one measurement per energy. Hence, the uncertainty in energy was calculated with a dose ratio variation TLD100/TLD100H of ±4.0 % (instead of ±2.8 %) using Table V.

E. Mean energy determination for X-ray sources

In Fig. 6, the simulated energy spectrum [31] and the calculated mean energy (64 keV) of the CBCT is plotted. Additionally, the mean energy with two standard uncertainties of the mean for the full- [$(60 \pm 15/\sqrt{152})$ keV] and the half- [$(69 \pm 22/\sqrt{152})$ keV] rotation CBCT can be seen. The determined mean energies were in good agreement with the simulation. The experimentally evaluated uncertainties in energy were in line with the calculated values (see Table VII). An increase in the uncertainty for an increase in the mean energy was noted for the experiment and for the calculation. $K_{absorption}$ was determined to 0.987 ± 0.007 (uncertainty of the mean $2\sigma/\sqrt{n}$). The mean energy of the CBCT was calculated from the whole-body measurement since a small change in energy is expected in the phantom [32]. In the field-of-view region, CBCT doses up to 1.7 Gy were measured. TLD100 showes supralinearity for doses a above 1.0 Gy [25]. However, within the experimental

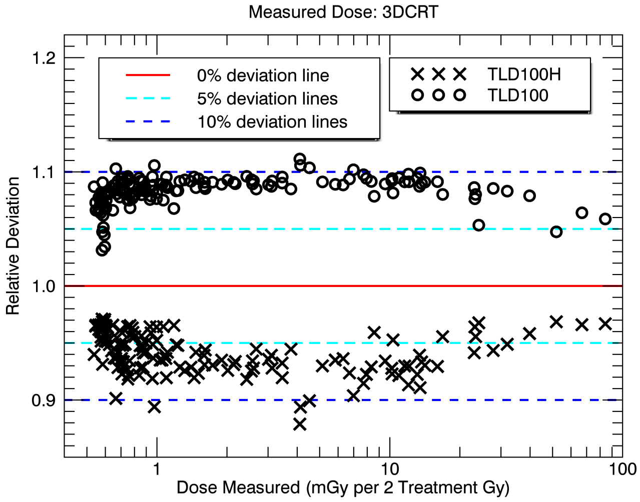

FIG. 5. Uncorrected TLD100 and TLD100H dose measured for the 6 MV 3DCRT plan divided by the corrected dose. The dose was corrected for the change in response with radiation energy using the double-TLD method presented in this work. Each pair of TLD100 and TLD100H at one dose point represents a double-TLD unit in the Alderson phantom.

TABLE IX. The simulated and measured mean photon energies in PMMA for two brachytherapy sources. The ^{137}Cs simulations were made for 8 cm source to TLD distance [30]. For 9 cm and 12 cm source to TLD distance, the mean energies of ^{192}Ir were estimated using the simulated locations of 5 cm and 10 cm source to TLD distance [28]. The 95 % confidence interval was calculated for the measurement by assuming a dose ratio (TLD100/TLD100H) uncertainty of 4 % (2σ). The error bars of 2σ for the simulation are based on the estimated statistical and interpolation uncertainties.

	Distance from source	MC simulation	Measured	Difference
^{137}Cs	7 cm	(0.60 ± 0.05) MeV	$(0.60[-0.16, +0.35])$ MeV	$(0.00[-0.17, +0.35])$ MeV
^{192}Ir	9 cm	(0.21 ± 0.02) MeV	(0.29 ± 0.04) MeV	(-0.08 ± 0.04) MeV
^{192}Ir	12 cm	(0.19 ± 0.02) MeV	(0.28 ± 0.04) MeV	(-0.09 ± 0.04) MeV

uncertainties no difference in the mean energy for doses between 1.0 mGy to 1.7 Gy was noted.

$K_{absorption}$ was determined to 1.99 ± 0.09 for the Faxitron measurement. The evaluated dose ratios of TLD100 and TLD100H without any build-up (Petri dishes) was 1.73 ± 0.11. For the measurements with build-up material, the dose ratio went up to 1.90 ± 0.23. The ratio of three TLD100 placed in the beam next to three TLD100H was 1.94 ± 0.12. No energy could be determined since all measured ratios were outside of the permitted range of $[1.0, 1.6]$ given by the response ratio curve (Fig. 2).

IV. DISCUSSION AND CONCLUSION

We introduced a double-TLD unit consisting of the two differently doped TLD100 and TLD100H. The accuracy of the method to determine the in- and out-of-field dose for external radiotherapy was evaluated by an end-to-end measurement for an interval of 1.5-0.2 MeV mean photon energy. The double-TLD unit showed an experimental accuracy of $-1\,\% \pm 2\,\%$ (2σ) compared to an IC. The measured uncertainties in dose was in agreement with the theoretically calculated values. The method automatically corrects for the variation in response with radiation energy of the TLDs by determination of the mean energy of the imping photons. The ability to determine the mean energy was evaluated for external radiotherapy, CBCT imaging and brachytherapy. The method resulted in good agreement between the experimentally determined and published MC simulated mean energies for all modalities. The calculated type B uncertainties in energy determination of the double-TLD unit were in line with the experimentally evaluated type A uncertainties.

A new thermal treatment for TLD100 was introduced using a more conservative high temperature annealing at 270 °C instead of 400 °C. Furthermore, the thermal treatment did not contain a low temperature annealing. The advantages are a three times faster work-flow and a protection of the TLD100 crystals. Using preheating, the low energy traps of TLD100 and $\text{TLD100}_{400\,^{\circ}\text{C}}$ could be cleared and the shape of the isothermal heating curves looked the same (Fig. 1). For the same

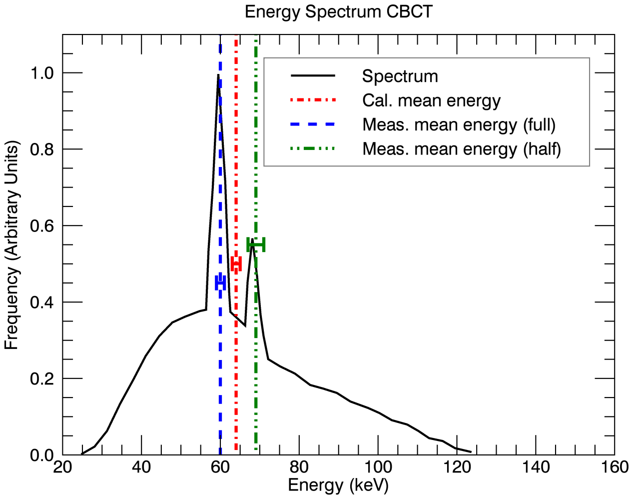

FIG. 6. Energy spectrum of the CBCT X-ray source simulated by Abuhaimed et al. [31] for a SID of 100 cm. Furthermore, the calculated mean energy of the spectrum with 2σ based on the statistical uncertainties of the simulations. The measured mean energies were derived from 152 measurement locations (in- and out-of-field) in the Alderson phantom for a full and half trajectory CBCT. Error bars of the measurement indicate two standard uncertainty (type A) of the mean ($2\sigma/\sqrt{n}$).

irradiation, TLD100 showed two times more signal in the main peak compared to TLD100$_{400\,^\circ\mathrm{C}}$. Linearity in dose and no fading effect were seen for the TLD100 using the thermal treatment presented in this work. An additional low temperature annealing for TLD100 will not produce improvement in dose measurement performance according to Muniz et al. [33].

Dependent on radiation energy TLD100 shows supralinearity in dose above 1.0 Gy [25], in contrast TLD100H is linear up to 10 Gy [20, 26, 27]. For external radiotherapy, in-field doses up to 2.3 Gy were measured. The individual $K_{energy,I}$ correction factors of the double-TLD unit reduced the systematic error caused by supralinearity. However, the mean energy was underestimated. For the CBCT doses of 1.0-1.7 Gy no supralinearity was noticed within the experimental uncertainties. According to Massillon et al. [25] and Cai et al. [34], the supralinear response in dose of TLD100 decreases for decreasing photon energy. Furthermore, an increase in TLD100 dose of a few percent caused by supralinearity would lead to a small error in mean energy since the gradient of response with radiation energy was large for the X-ray spectrum used. Nevertheless, it is recommended to use the double-TLD unit for dose levels below 1.0 Gy or to correct for the nonlinearity of the TLD dose calibration.

Most of the data for the response with radiation energy was taken from Davis et al. [7]. They used the same thermal treatment as for TLD100$_{400\,^\circ\mathrm{C}}$. In contrast to the expectations, the TLD100/IC ratio showed better agreement with MC simulations compared to the TLD100$_{400\,^\circ\mathrm{C}}$/IC ratio [Fig. 3(b)]. Compared to IC, the TLD100$_{400\,^\circ\mathrm{C}}$ showed a significant under-response for the in-field measurement. The difference of the in-field measurement (side face) compared to the calibration (front face) was the orientation of the TLD toward the beam. TLD100 and TLD100H chips show a difference in response depending on the angle of irradiation [8, 35]. The LiF response decreases for a front face compared to a side face irradiation. In the out-of-field region, TLD100$_{400\,^\circ\mathrm{C}}$ showed a significant difference in response with radiation energy compared to TLD100 except for the irradiation where the TLDs were facing the beam. Therefore, one possible explanation for the difference in response for TLD100$_{400\,^\circ\mathrm{C}}$ and TLD100 could be the influence of the thermal treatment on the angular response. A dose determination within the accuracy aimed for in radiotherapy was possible by using the TLD100$_{400\,^\circ\mathrm{C}}$/TLD100H dose ratio. However, the TLD100/TLD100H ratio produced more accurate results and was more material protecting.

For external radiotherapy, the most accurate prediction in the mean energy compared to the simulations was derived from the TLD100H/IC ratio. In contrast to TLD100, the response with radiation energy of TLD100H is known for 0.37 MeV (Fig. 2). With more interpolation points, a more accurate energy prediction is expected.

For external radiotherapy, it was shown that in the first 20 cm the mean photon energy decreases with increasing distance from the field edge (Fig. 4). This decrease was different for different treatment techniques (3DCRT, VMAT, and IMRT). For the presented treatment plans, patient scatter is the dominating out-of-field dose contribution close to the field edge [36–41]. According to Hauri et al. [36], patient scatter corresponds to the lowest photon energy for all scatter contributions and is more pronounced for the 3DCRT compared to IMRT or VMAT treatment. The increase in energy with increasing isocenter distance can be explained by the increase of head leakage and collimator scatter [37]. All TrueBeam treatment techniques show the same mean energy at the furthest point from the isocenter. Head leakage is the dominating out-of-field dose contribution far from the isocenter for Varian linear accelerators [36, 37]. For Cobalt machines, leakage is almost not present due to a excellent shielding of the gantry head. This fact explains the drop in energy for the MRIdian treatment after 40 cm isocenter distance (Fig. 4).

Often, the stray dose in photon radiotherapy is measured with TLDs by using one general energy correction factor ([5, 23]).

However, the variation of the photon energy in the phantom body can lead to a systematic dose difference if only one correction factor is used ([6, 42] and Fig. 5). The main advantages of using the presented double-TLD unit are first, the randomly distributed error in dose and second, that the exact energy spectrum does not have to be known in advance. Furthermore, individual TLD energy correction factors can be evaluated for arbitrary complex treatment plans. Even with dedicated MC simulations this is not possible.

For brachytherapy, the presented method worked well for ^{137}Cs. For ^{192}Ir in PMMA, the mean energy of 0.2 MeV was overestimated compared to MC simulations by around 0.1 MeV. The overestimation in photon energy can be explained by the missing response values of TLD100H between 0.16-0.37 MeV. Nevertheless, the application of a correction factor corresponding to a mean energy of 0.3 MeV for a measurement with 0.2 MeV photons would lead to a systematic dose overestimation below 2 %.

The double-TLD unit determined the mean energy of the CBCT X-ray spectrum in agreement with the MC simulations. However, the interpolation of the TLD100/TLD100H dose ratios in the response ratio curve (Fig. 2) is unique for the CBCT X-ray spectrum used. The response ratio curve shows a local minimum and maximum for 83 keV and 47 keV, respectively. For spectra with mean energy around a local extreme, the mean energy cannot be determined since the interpolation is not unique.

For photon energies used in imaging, LiF TLDs show an angular dependence in dose response of up to 10 % [8, 35]. The accurate energy determination for the CBCT indicated the same decrease for a side face irradiation of TLD100 and TLD100H. Hence, for the energy determination with the double-TLD method the angular dependency is not problematic since the orientation toward the beam is the same for TLD100 and TLD100H. However, the dose can be underestimated.

The relative response ratio (Fig. 2) can also be used to determine the mean energy of a kerma measurement because the air-kerma-based values of TLD100 and TLD100H were converted to dose-to-water with the same mass attenuation factor per mean energy. The good agreement between the converted values [7] and the measured dose-to-water variation of LiF:Mg,Ti with radiation energy [22] shows that the conversion is appropriate. For the photon energy measurement of the Faxitron, the TLD100/TLD100H dose ratio with or without buildup material showed a large deviation to the predicted ratio. The expected mean photon energy for the 130 $\mathrm{kV_p}$ source lies between 80 keV and 120 keV. For TLD100 and TLD100H, Kron et al. [20] and Duggan et al. [21] found an anomalous dip in response for monochromatic photon beam of around 80 keV. The response with radiation energy for a mean energy of 80 keV is around two times lower for a monochromatic compared to a spectrum irradiation. The difference between the calibration and the measurement spectrum could be an explanation for the large TLD100/TLD100H ratios measured for the Faxitron irradiation.

The accurate dose and energy determination of the double-TLD unit was experimentally validated for external radiotherapy. For brachytherapy and CBCT imaging the double-TLD unit accurately determined the energy. This hypothesizes that the presented double-TLD unit can accurately determine the dose for brachytherapy and imaging modalities. However, this has to be verified in further experiments.

The mean energy of a spectrum could be measured by the double-TLD unit because the response as a function of the mean energy was used (Fig. 2). A systematic error is induced by a difference in the calibration spectrum and a field measurement spectrum. The dose ratios between other types of TLDs [15–18] will lead to a bigger systematic error since the response with radiation energy shows larger gradient changes compared to the TLD100/TLD100H method.

For nominal beam energies below 10 MeV, the presented dose and energy measurements can be utilized. Higher nominal beam energies will produce secondary neutrons which affect the signal of the TLDs [11]. In this case, it is suggested to measure the dose with neutron-insensitive TLD700 and TLD700H detectors. Schwahofer et al. [22] showed that TLD600 and TLD700 have the same energy dependence as TLD100 (Fig. 2). The LiF crystal of TLD600 is enriched with ^{6}Li while TLD700 contains mainly ^{7}Li. It is expected that the photon energy dependence of TLD600H and TLD700H is the same as for TLD100H since the number of neutrons in Li does not affect the energy bands of the TLD crystal [22].

ACKNOWLEDGMENT

This work was funded by the grant KFS-3249-08-2013 from the Swiss Cancer League.

DISCLOSURE

The authors have no relevant conflicts of interest to disclose.

---

[1] Schneider U, “Modeling the risk of secondary malignancies after radiotherapy,” Genes **2**, 1033–1049 (2011).
[2] Wolden SL, Lamborn KR, Cleary SF, Tate DJ, and Donaldson SS, “Second cancers following pediatric Hodgkin’s disease.” Journal of Clinical Oncology **16**, 536–544 (1998).

[3] Schneider U, Hälg RA, Hartmann M, Mack A, Storelli F, Joosten A, Möckli R, and Besserer J, “Accuracy of out-of-field dose calculation of tomotherapy and cyberknife treatment planning systems: a dosimetric study,” Zeitschrift für Medizinische Physik **24**, 211–215 (2014).

[4] Howell RM, Scarboro SB, Kry SF, and Yaldo DZ, “Accuracy of out-of-field dose calculations by a commercial treatment planning system,” Physics in Medicine and Biology **55**, 6999 (2010).

[5] Kry SF, Titt U, Pönisch F, Followill D, Vassiliev ON, White RA, Mohan R, and Salehpour M, “A Monte Carlo model for calculating out-of-field dose from a varian 6 MV beam,” Medical Physics **33**, 4405–4413 (2006).

[6] Scarboro SB, Followill DS, Howell RM, and Kry SF, “Variations in photon energy spectra of a 6 MV beam and their impact on TLD response,” Medical Physics **38**, 2619–2628 (2011).

[7] Davis SD, Ross CK, Mobit PN, Zwan LVd, Chase WJ, and Shortt KR, “The response of LiF thermoluminescence dosemeters to photon beams in the energy range from 30 kV X-rays to Co-60 gamma rays,” Radiation Protection Dosimetry **106**, 33–43 (2003).

[8] Freire LC, Pereira MF, Calado AM, Santos LM, Cardoso JV, and Alves JG, “Evaluation of the performance of two LiF:Mg,Ti and LiF:Mg,Cu,P dosemeters for extremity monitoring,” Radiation Protection Dosimetry **144**, 140–143 (2011).

[9] Freire L, Calado A, Cardoso JV, Santos LM, and Alves JG, “Comparison of LiF (TLD-100 and TLD-100H) detectors for extremity monitoring,” Radiation Measurements Proceedings of the 15th Solid State Dosimetry (SSD15), **43**, 646–650 (2008).

[10] Harris CK, Elson HR, Lamba MAS, and Foster AE, “A comparison of the effectiveness of thermoluminescent crystals LiF:Mg,Ti, and LiF:Mg,Cu,P for clinical dosimetry,” Medical Physics **24**, 1527–1529 (1997).

[11] Kry SF, Price M, Followill D, Mourtada F, and Salehpour M, “The use of LiF (TLD-100) as an out-of-field dosimeter,” Journal of Applied Clinical Medical Physics **8**, 169–175 (2007).

[12] Pradhan AS and Quast U, “In-phantom response of LiF TLD-100 for dosimetry of Ir-192 HDR source,” Medical Physics **27**, 1025–1029 (2000).

[13] Taylor ML, “Robust determination of effective atomic numbers for electron interactions with TLD-100 and TLD-100H thermoluminescent dosimeters,” Nuclear Instruments and Methods in Physics Research Section B: Beam Interactions with Materials and Atoms **269**, 770–773 (2011).

[14] Olko P, Bilski P, Ryba E, and Niewiadomski T, “Microdosimetric interpretation of the anomalous photon energy response of ultra-sensitive LiF:Mg,Cu,P TL dosemeters,” Radiation Protection Dosimetry **47**, 31–35 (1993).

[15] Gorbics SG and Attix FH, “LiF and CaF2:Mn thermoluminescent dosimeters in tandem,” The International Journal of Applied Radiation and Isotopes **19**, 81–84 (1968).

[16] Miljanic S, Vekic B, and Martincic R, “Determination of X-ray effective energy and absorbed dose using CaF2:Mn and LiF:Mg,Ti thermoluminescence dosemeters,” Radiation Protection Dosimetry **85**, 381–384 (1999).

[17] Oliveira ML and Maia AF, “TL tandem systems for the determination of effective energy in X radiation beams,” Applied Radiation and Isotopes **68**, 788–790 (2010).

[18] Nelson VK, Holloway L, and McLean ID, “The application of thermoluminescence dosimetry in X-ray energy discrimination,” Australasian Physical & Engineering Sciences in Medicine / Supported by the Australasian College of Physical Scientists in Medicine and the Australasian Association of Physical Sciences in Medicine **38**, 543–549 (2015).

[19] Sáez-Vergara JC, Romero AM, Ginjaume M, Ortega X, and Miralles H, “Photon energy response matrix for environmental monitoring systems based on LiF:Mg,Ti and hypersensitive phosphors (LiF:Mg,Cu,P and a-Al2O3:C),” Radiation Protection Dosimetry **85**, 207–211 (1999).

[20] Kron T, Duggan L, Smith T, Rosenfeld A, Butson M, Kaplan G, Howlett S, and Kazuyuki Hyodo, “Dose response of various radiation detectors to synchrotron radiation,” Physics in Medicine and Biology **43**, 3235 (1998).

[21] Duggan L, Hood C, Warren-Forward H, Haque M, and Kron T, “Variations in dose response with X-ray energy of LiF:Mg,Cu,P thermoluminescence dosimeters: implications for clinical dosimetry,” Physics in Medicine and Biology **49**, 3831 (2004).

[22] Schwahofer A, Feist H, Georg H, Häring P, and Schlegel W, “Experimental determination of the photon-energy dependent dose-to-water response of TLD600 and TLD700 (LiF:Mg,Ti) thermoluminescence detectors,” Zeitschrift für Medizinische Physik **27**, 13–20 (2017).

[23] Hälg RA, Besserer J, and Schneider U, “Systematic measurements of whole-body dose distributions for various treatment machines and delivery techniques in radiation therapy,” Medical Physics **39**, 7662–7676 (2012).

[24] Piters TM and Bos AJJ, “Influence of the cooling rate on repeatability of LiF:Mg,Cu,P thermoluminescent chips,” Radiation Protection Dosimetry **33**, 91–94 (1990).

[25] Massillon-JL G, Ávila O, and Brandan ME, “Supralinear response of LiF:Mg,Ti (TLD-100) after exposure to 100 keV average energy X-rays,” Radiation Measurements Proceedings of the 16th Solid State Dosimetry Conference , September 19-24 , Sydney , Australia, **46**, 1357–1360 (2011).

[26] Wu DK, Sun FY, and Dai HC, “A high sensitivity LiF thermoluminescent dosimeter–LiF(Mg,Cu,P),” Health Physics **46**, 1063–1067 (1984).

[27] Bacci C, Furetta C, D’Angelo L, and Giancola S, “Comprehensive study on LiF:Cu,Mg,P (GR-200 A),” Radiation Protection Dosimetry **47**, 215–218 (1993).

[28] Meli JA, Meigooni AS, and Nath R, “On the choice of phantom material for the dosimetry of Ir-192 sources,” International Journal of Radiation Oncology • Biology • Physics **14**, 587–594 (1988).

[29] Zilio VO, Joneja OP, Popowski Y, Rosenfeld A, and Chawla R, “Absolute depth-dose-rate measurements for an Ir-192 HDR brachytherapy source in water using MOSFET detectors,” Medical Physics **33**, 1532–1539 (2006).

[30] Pérez-Calatayud J, Granero D, Casal E, Ballester F, and Puchades V, “Monte Carlo and experimental derivation of TG43 dosimetric parameters for CSM-type Cs-137 sources,” Medical Physics **32**, 28–36 (2005).

[31] Abuhaimed A, Martin CJ, Sankaralingam M, Gentle DJ, and McJury M, “An assessment of the efficiency of methods for measurement of the computed tomography dose index (CTDI) for cone beam (CBCT) dosimetry by Monte Carlo simulation,” Physics in Medicine and Biology **59**, 6307 (2014).

[32] Kondo S and Koyama S, “Estimation of effective energy in phantom in X-ray CT using Monte Carlo simulation,” Progress in Nuclear Science and Technology **3**, 82–85 (2012).

[33] Muniz JL, Delgado A, and Hernandez Verduzco R, “A comparison of the TLD-100 dosimetric performance using different annealing procedures and glow curve analysis,” Radiation Protection Dosimetry **66**, 273–277 (1996).

[34] Cai GG, Bestion N, Wang SS, Shen WX, Delard R, Volpiliere J, Fesquet J, and Gasiot J, “Dose response of the individual peak for LiF:Mg,Ti (TLD-100) and LiF:Mg,Cu,P (GR-200a) TL materials at the photon energies of 30, 104, 1250 keV,” Radiation Protection Dosimetry **65**, 213–215 (1996).

[35] Dong SL, Chu TC, Lan GY, Wu TH, Lin YC, and Lee JS, “Characterization of high-sensitivity metal oxide semiconductor field effect transistor dosimeters system and LiF:Mg,Cu,P thermoluminescence dosimeters for use in diagnostic radiology,” Applied Radiation and Isotopes **57**, 883–891 (2002).

[36] Hauri P, Hälg RA, Besserer J, and Schneider U, “A general model for stray dose calculation of static and intensity-modulated photon radiation,” Medical Physics **43**, 1955 (2016).

[37] Ruben JD, Lancaster CM, Jones P, and Smith RL, “A comparison of out-of-field dose and its constituent components for intensity-modulated radiation therapy versus conformal radiation therapy: implications for carcinogenesis,” International Journal of Radiation Oncology • Biology • Physics **81**, 1458–1464 (2011).

[38] Chofor N, Harder D, Willborn KC, and Poppe B, “Internal scatter, the unavoidable major component of the peripheral dose in photon-beam radiotherapy,” Physics in Medicine and Biology **57**, 1733 (2012).

[39] Lillicrap SC, Morgan HM, and Shakeshaft JT, “X-ray leakage during radiotherapy.” The British Journal of Radiology **73**, 793–794 (2000).

[40] Kase KR, Svensson GK, Wolbarst AB, and Marks MA, “Measurements of dose from secondary radiation outside a treatment field,” International Journal of Radiation Oncology • Biology • Physics **9**, 1177–1183 (1983).

[41] Jagetic LJ and Newhauser WD, “A simple and fast physics-based analytical method to calculate therapeutic and stray doses from external beam, megavoltage X-ray therapy,” Physics in Medicine and Biology **60**, 4753 (2015).

[42] Nelson VK, “Response of TL dosimeters outside the field edge of a 6 MV Linac beam and its implication on patient dosimetry,” in *World Congress on Medical Physics and Biomedical Engineering 2006*, edited by Magjarevic R and Nagel JH (2007) pp. 2079–2082.

Chapter 3

No increase in effective dose from half compared to full rotation pelvis cone beam CT

Pascal Hauri[1,2], Roger A. Hälg[1,2], and Uwe Schneider[1,2]

[1] Institute for Radiotherapy, Radiotherapie Hirslanden AG, Aarau, Switzerland

[2] Department of Physics, University of Zurich, Zurich, Switzerland

This chapter was adapted from the original article:

"Technical Note: No increase in effective dose from half compared to full rotation pelvis cone beam CT"

Published in:

Journal of Applied Clinical Medical Physics 2017, **18(5)**, 364–368
doi:10.1002/acm2.12150.

Purpose: To image the abdomen of a patient with a gantry mounted imaging system of a linear accelerator, different cone beam computed tomography (CBCT) protocols are available. The whole-body doses of a full rotation abdomen CBCT and a half rotation CBCT were compared. In our clinic, both CBCT protocols are used in daily routine work.
Methods: With an adult anthropomorphic Alderson phantom, the whole-body dose per CBCT scan was measured with thermoluminescence dosimeters. The half rotation CBCT was applied such that the gantry mounted X-ray source rotated around the right side of the phantom. The 183 measurement locations covered all ICRP recommended critical organs (except the gonads). The effective dose was calculated with the mean organ dose and the corresponding tissue weighting factors. A point-by-point dose comparison of both protocols was conducted.
Results: The effective dose was 5.4 mSv ± 5 % and 5.0 mSv ± 5 % (estimated type B 1σ) for the full and the half rotation CBCT, respectively. There was no significant difference ($\alpha = 0.05$) in the effective dose within the precision of the measurement ($1\sigma = \pm 5\,\%$). The half rotation CBCT displayed an inhomogeneous dose distribution in a transversal phantom slice in contrast with the full rotation CBCT. In the imaging region, the mean dose was (20.5 ± 3.4) mGy and (19.2 ± 7.4) mGy (measured type A 1σ) for the full and the half rotation CBCT, respectively.
Conclusion: The half compared to the full rotation CBCT displays a smaller field-of-view in a transversal slice and no significant difference in the effective dose. Hence, the full rotation CBCT is favorable compared to the half rotation CBCT. However, by using the half rotation protocol, critical volumes in the patient can be spared compared to the full rotation protocol.

Keywords: Cone Beam CT, Effective Dose, Abdomen, Radiotherapy

I. INTRODUCTION

Cone beam computed tomography (CBCT) is widely used in clinics for patient positioning in a radiation treatment session. The advantage of image-guided radiation therapy (IGRT) is the application of more conformal plans and, therefore, a reduction of the irradiated volume. The additional dose received by the patient [1] raises concerns about late effects such as second primary cancers. Hence, the quantification of CBCT dose is an important issue.

The TrueBeam linear accelerator (Varian Medical Systems, Palo Alto, CA, USA) is equipped with a gantry mounted on-board imager (OBI) capable of performing CBCT scans. To image the abdomen, the pelvis or the pelvis spotlight protocol is available. For the pelvis protocol, the CBCT is acquired with a full rotation of the X-ray source around the patient. The pelvis spotlight protocol uses a half rotation of the X-ray source around the patient. The weighted CT dose index ($\mathrm{CTDI_w}$) given by Varian is 1/3 lower for the half compared to the full rotation CBCT. Hence, in clinical practice, the spotlight protocol is used more frequently because of the potential dose reduction compared to the full rotation protocol. The resulting spotlight CBCT has a smaller field-of-view in a transversal slice compared to the full rotation protocol.

In the last years, many studies have been conducted about CBCT dose for different protocols [2–9]. Some of them evaluated only the CTDI values [3, 9]. Kan et al. [10], Cheng et al. [6], and Hälg et al. [7] determined the effective dose (ED) for pelvis protocols using the OBI of a Varian linear accelerator. In another paper [2], Monte Carlo dose calculations of different pelvis CBCT protocols were performed for real patient geometries.

With the OBI (version 2.5.28.0) of a TrueBeam linear accelerator, the absorbed dose for the latest pelvis, and pelvis spotlight CBCT protocol was measured. Both CBCT protocols are used in-house in daily routine work. The 183 measurement locations in an anthropomorphic Alderson phantom were equipped with thermoluminescence dosimeters (TLDs). A combination of Li:Mg,Ti (TLD100) and Li:Mg,Cu,P (TLD100H) chips was used to automatically correct for the variation in response with radiation energy of the TLDs [11]. This allowed a more accurate determination of the whole-body absorbed dose ($1\sigma = \pm 5\,\%$) compared to previous studies. The ED values of both pelvis protocols were calculated by the determination of the mean doses to critical structures and the ICRP guidelines [12]. Furthermore, the absorbed dose of the pelvis and the pelvis spotlight CBCT was compared on a point-by-point basis.

II. METHODS AND MATERIALS

All measurements and detector readouts were performed according to a strict protocol to ensure consistency of the measurements.

A. Imaging modality and whole-body dose measurement

The two evaluated CBCT pelvis protocols were provided by the vendor (see Table I). For both protocols, the X-ray source was operated at 125 $\mathrm{kV_p}$, which resulted in a mean photon energy of 64 keV [9]. The CBCT measurements were done at Hirslanden Medical Center in Aarau, Switzerland.

The absorbed dose of the CBCTs was measured using an adult anthropomorphic Alderson-Rando phantom (RSD Radiology Support Devices, Long Beach, CA, USA). The phantom was positioned head first supine. The measurement locations were distributed in the Alderson phantom according to Hälg et al. [7]. The locations covered the ICRP recommended critical organs (except the gonads). At each of the 183 measurement locations in and on the phantom, a TLD100H was stacked on top of a TLD100 for dose measurement. To have a dose of at least 1 mGy at each measurement location, the full and the half rotation CBCT were irradiated 45 and 55 times, respectively. The dose of each CBCT protocol was normalized to one scan. The dose of 1 mGy ensured enough signal for the readout of the TLDs. The pelvis spotlight CBCT was acquired by rotating the cone beam over the right side of the Alderson phantom [see Table I and Fig. 2(b)].

TABLE I. Acquisition parameters for the two different kV CBCT protocols given by Varian (version 2.5.28.0). In our clinic, both protocols are used in daily routine work in the current form.

	Pelvis	Pelvis spotlight
Peak voltage ($\mathrm{kV_p}$)	125	125
Exposure (mAs)	1080	750
Fan Type	Half	Full
Gantry rotation (degree) (up,left,down,right) = (0°,90°,180°,270°)	360° 180° ↔ 180°	209° 256° ↔ 105°
Field-of-view diameter (cm)	46.5	26.2
Transversal dimension from isocenter (cm)	±8.75	±9.25
Slice thickness (mm)	2.0	2.0
Matrix (pixel)	512	512
Projections	900	500
$\mathrm{CTDI_w}$ (mGy)	14.3	10.1

B. TLD dose evaluation

The whole-body dose of the two CBCT protocols was measured with a combination of TLD100 and TLD100H chips. The two TLD types show a different response with radiation energy compare to ^{60}Co [13]. For the dose measurements, a TLD100H chip was put on top of a TLD100 chip. The doses measured by the TLD100 and TLD100H were evaluated by using individual calibration factors determined with a 6 MV nominal beam energy irradiation, applied with a TrueBeam linear accelerator. The individual energy correction factor for TLD100 and TLD100H was found by the ratio of the TLD100 divided by the TLD100H dose. Hence, each single TLD was corrected with a specific energy correction factor displaying a random error. The finale dose was calculated with the mean of the corrected TLD100 and TLD100H dose. A detailed description of the TLD dose and energy measurement is given by Hauri et al. [11]. All absolute dose measurements were correlated to a Farmer Chamber 30013 (PTW, Freiburg, Germany).

C. Dose comparison

ED values were obtained by using the tissue weighting factors from ICRP publication 103 [12] and the mean organ doses. Each organ dose was calculated by the mean of the determined point doses at the corresponding organ location. The image isocenter was located in the prostate region. The gonad dose had to be estimated due to missing measurement points. For this, the mean of six dose points was calculated. The points were located in a transversal slice 5 cm from the image isocenter in direction "feet toward head" (FH). In this transversal phantom slice, the points to estimate the gonad dose were located in the right to left (RL) middle of the phantom, along a line anterior posterior. The gonad location in the phantom was at −5 cm from the image isocenter in the FH direction. The ED was calculated according to the ICRP 103 [12] recommendation:

$$\mathrm{ED} = \sum_T w_T H_T = \sum_T w_T \sum_R w_R D_{T,R},$$

where w_R is the radiation weighting factor with $w_R = 1$ for photon irradiations. $D_{T,R}$ is the mean absorbed dose from radiation R in tissue T. w_T is the tissue weighting factor for tissue T with $\sum_T w_T = 1$. $H_T = \sum_R w_R D_{T,R}$ is the equivalent dose for tissue T. Furthermore, the absorbed dose of the two different CBCT protocols was evaluated by a point-by-point comparison.

III. RESULTS

The estimated type B standard deviation (1σ) for a CBCT dose point measurement was $\pm 5\,\%$. A more detailed error analysis can be found in Hauri et al. [11].

In Table II, the effective organ doses are displayed for both CBCT protocols. Furthermore, the number of measurement points to calculate the mean organ dose is shown. The ED was determined to $5.4\,\mathrm{mSv} \pm 5\,\%$ and $5.0\,\mathrm{mSv} \pm 5\,\%$ (type B 1σ) for the full and the half rotation CBCT, respectively. The $95\,\%$ confidence interval of the difference between the two ED values contained zero [$(0.4 \pm 0.7)\,\mathrm{mSv}$]. Hence, there was no significantly difference ($\alpha = 0.05$) of the ED values between the two protocols within the precision of the measurement ($\pm 5\,\%$).

TABLE II. The ICRP weighting factors w_T [12] and the determined equivalent dose H_T of the organ T for both CBCT protocols (OBI version 2.5.28.0). Furthermore, the number of measurement points to calculate the mean absorbed organ dose is shown. The mean red bone marrow and bone surface doses were determined from the same 33 measurement locations. The effective dose for the pelvis and the pelvis spotlight was calculated to $(5.4 \pm 0.3)\,\mathrm{mSv}$ and $(5.0 \pm 0.3)\,\mathrm{mSv}$, respectively.

	w_T	H_T pelvis (mSv)	H_T pelvis spotlight (mSv)	Number of measurement points
Gonads	0.08	23.8	22.0	6
Red bone marrow	0.12	4.49	4.31	33
Colon	0.12	6.09	5.01	17
Lung	0.12	0.190	0.154	30
Stomach	0.12	0.277	0.209	4
Breasts	0.12	0.215	0.201	4
Bladder	0.04	20.0	18.4	2
Liver	0.04	0.468	0.511	11
Oesophagus	0.04	0.135	0.119	5
Thyroid	0.04	0.0875	0.0716	2
Skin	0.01	17.7	17.1	5
Bone surface	0.01	4.49	4.31	33
Salivary glands	0.01	0.0695	0.0652	4
Brain	0.01	0.0526	0.0451	10
Remainder of body	0.12	9.23	8.62	56

Fig. 1 shows the point-by-point comparison of the absorbed dose for both CBCT protocols. The highest dose per scan was located in the field-of-view region. Here, the biggest differences in dose between the full and the half rotation CBCT was present. However, the mean dose of 37 measurement locations in the field-of-view region was $(20.5 \pm 3.4)\,\mathrm{mGy}$ and $(19.2 \pm 7.4)\,\mathrm{mGy}$ (measured type A 1σ) for the full and the half rotation CBCT, respectively. Outside the image region both protocols showed a similar dose per scan (Fig. 1). The peripheral dose decreased from $15\,\mathrm{mGy}$ to $0.030\,\mathrm{mGy}$ with increasing distance to the scanned region.

Figs. 2(a) and (b) show the dose in the same transversal CBCT slice in the imaging region for the full and half rotation CBCT, respectively. The dose of the full rotation CBCT was homogeneously distributed in a transversal slice of the phantom.

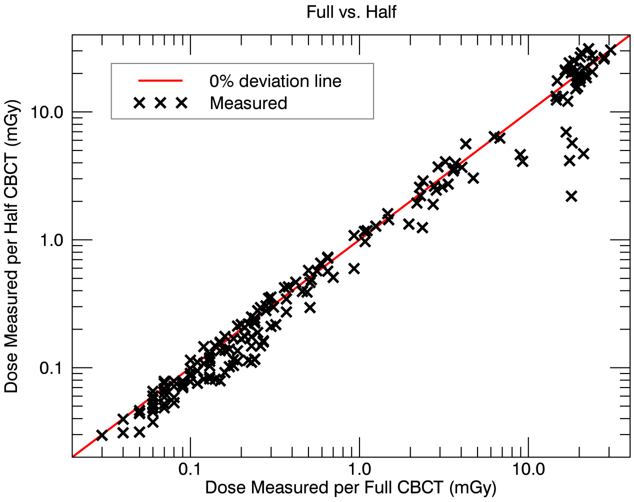

FIG. 1. Measured point doses per CBCT scan in the Alderson phantom. Each cross corresponds to a unique measurement location for the pelvis and the pelvis spotlight protocol. For all points below the 45 ° line, the dose of the pelvis spotlight was lower compared to the pelvis protocol.

In the RL middle of the slice, the dose of both protocols was similar. On the right side of the phantom, the half rotation CBCT displayed a higher dose compared to the full rotation CBCT. In contrast, on the phantom's left side, the dose of the spotlight CBCT was lower compared to the pelvis CBCT.

For the half rotation CBCT, the dose in the phantom's right side was higher compared to the left side. In the scanned region, the dose was up to a factor of ten higher on the right compared to the left side of the phantom [Figs. 2(b) and (c)]. Outside the imaging region, the dose on the right side was a factor of two higher compared to the phantom's left side. The right eye measurement location displayed 0.09 mGy per spotlight scan, while for the left eye, a dose of 0.05 mGy was noticed. The dose of the left eye for the full rotation CBCT was 0.08 mGy.

IV. DISCUSSION

With the OBI of a TrueBeam Varian linear accelerator, the doses of a full rotation and a half rotation CBCT protocol (Table I) were measured. Both CBCT protocols are used in daily routine work. At 183 points in and on an anthropomorphic Alderson phantom, the dose per scan was evaluated. For both protocols, the ED was calculated and the absorbed dose was compared on a point-by-point basis. Both ED values were in the range of 5 mSv. Within the precision of the measurement (type B $1\sigma = \pm 5\,\%$), there was no significant difference ($\alpha = 0.05$) between the two ED values. An inhomogeneous dose deposition in transversal phantom slices was noticed for the spotlight CBCT protocol.

Despite the efforts to reduce the dose to the patient, the H_T and ED values determined by others in 2011 (OBI version 1.4.13) [6] and 2012 [7] are of the same order as presented in this study. Hälg et al. [7] used the same measurement location and the same phantom as in the current study. Nevertheless, in a study from 2008 [10], a four times higher ED was reported for the Varian system. The mean organ doses determined by Monte Carlo simulations for real patient geometries [2] are in the same range as presented here (Table II). Hence, the anthropomorphic phantom used for the measurements represents an adult patient geometry well. The determined CBCT dose for an adult should not be projected to a pediatric patient, since the absorbed dose in a young patient is likely to be higher [8]. The higher dose is caused by less attenuation of the X-ray beam in the pediatric compared to the adult patient. Furthermore, in an adolescent patient, critical structures are closer to the imaging region compared to an adult patient.

In the image region, a dose reduction by a factor of ten for critical points can be achieved by using the half compared to the full rotation CBCT. To accomplish a dose reduction for a critical volume, the starting angle of the half rotation CBCT acquisition is crucial [see Fig. 2(b)]. Nevertheless, there is no significant reduction in ED for the half compared to the full rotation CBCT.

According to Gardner et al. [4], the contrast-to-noise ratio of the pelvis compared to the spotlight protocol is significantly higher. Hence, the full rotation CBCT provides better soft tissue contrast compared to the half rotation protocol.

The ED is a function of the mean organ dose. Therefore, the ED values depend on the distribution of the measurement location in the phantom. This study represents a conservative estimation of the ED since 1/5 of the TLDs were distributed in the imaging region representing 1/10 of the body. The type B uncertainty of the dose measurement ($1\sigma = \pm 5\,\%$) was propagated to the ED. This is rather an overestimation of the ED uncertainty since H_T was calculated by the mean of multiple measurement locations (Table II).

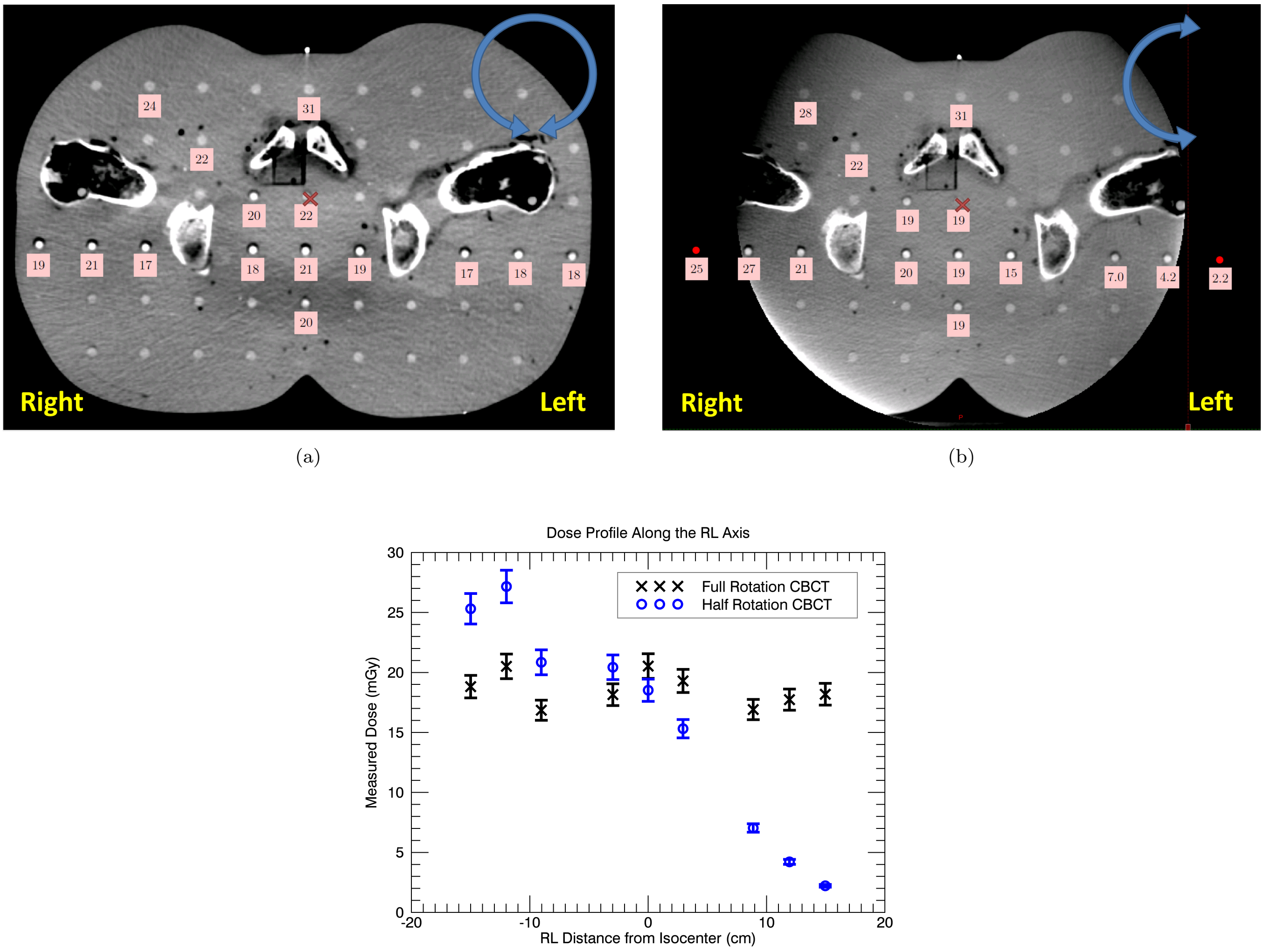

(a)

(b)

(c)

FIG. 2. The measured point doses (mGy) per scan in a transversal slice of the Alderson phantom for (a) the pelvis CBCT and (b) the pelvis spotlight CBCT. The arrow in the right upper corner of the CBCT slice indicates the rotation of X-ray source around the phantom. The cross in the middle of the slice represents the image isocenter. (c) The dose profiles along the RL axis of the full and the half rotation CBCT for the same transversal slice from (a) and (b). The error bars represent the standard deviation of the dose measurements.

The higher photoelectric cross section of bones compared to tissue is reported to cause a few times higher dose to bones than to nearby tissue [2, 5]. For the TLDs distributed in the human bony material of the Alderson phantom used in this work, no higher dose was noticed compared to the surrounding soft tissue. Hence, the equivalent dose to bones could be underestimated.

V. CONCLUSION

The half compared to the full rotation CBCT displays a smaller field-of-view and no significant difference in the ED. Hence, the full rotation CBCT is favorable compared to the half rotation CBCT. However, by using the half rotation protocol, critical points in the patient can be spared compared to the full rotation protocol.

ACKNOWLEDGMENT

This work was funded by the grant KFS-3249-08-2013 from the Swiss Cancer League.

DISCLOSURE

The authors have no relevant conflicts of interest to disclose.

[1] Murphy MJ, Balter J, Balter S, BenComo Jr. AJ, Das IJ, Jiang SB, Ma CM, Olivera GH, Rodebaugh RF, Ruchala KJ, Shirato H, and Yin FF, "The management of imaging dose during image-guided radiotherapy: report of the AAPM Task Group 75," Medical Physics **34**, 4041–4063 (2007).

[2] Montanari D, Scolari E, Silvestri C, Graves YJ, Yan H, Cervino L, Rice R, Jiang SB, and Jia X, "Comprehensive evaluations of cone-beam CT dose in image-guided radiation therapy via GPU-based Monte Carlo simulations," Physics in Medicine and Biology **59**, 1239–1253 (2014).

[3] Kim S and Alaei P, "Implementation of full/half bowtie filter models in a commercial treatment planning system for kilovoltage cone-beam CT dose estimations," Journal of Applied Clinical Medical Physics **17**, 5988 (2016).

[4] Gardner SJ, Studenski MT, Giaddui T, Cui Y, Galvin J, Yu Y, and Xiao Y, "Investigation into image quality and dose for different patient geometries with multiple cone-beam CT systems," Medical Physics **41**, 031908 (2014).

[5] Poirier Y and Tambasco M, "Experimental validation of a kV source model and dose computation method for CBCT imaging in an anthropomorphic phantom," Journal of Applied Clinical Medical Physics **17**, 6021 (2016).

[6] Cheng HCY, Wu VWC, Liu ESF, and Kwong DLW, "Evaluation of radiation dose and image quality for the varian cone beam computed tomography system," International Journal of Radiation Oncology • Biology • Physics **80**, 291–300 (2011).

[7] Hälg RA, Besserer J, and Schneider U, "Systematic measurements of whole-body imaging dose distributions in image-guided radiation therapy," Medical Physics **39**, 7650–7661 (2012).

[8] Son K, Kim JS, Lee H, and Cho S, "Imaging dose of human organs from kV-CBCT in image-guided radiation therapy," Radiation Protection Dosimetry **175**, 194–200 (2016).

[9] Abuhaimed A, Martin CJ, Sankaralingam M, Gentle DJ, and McJury M, "An assessment of the efficiency of methods for measurement of the computed tomography dose index (CTDI) for cone beam (CBCT) dosimetry by Monte Carlo simulation," Physics in Medicine & Biology **59**, 6307 (2014).

[10] Kan MWK, Leung LHT, Wong W, and Lam N, "Radiation dose from cone beam computed tomography for image-guided radiation therapy," International Journal of Radiation Oncology • Biology • Physics **70**, 272–279 (2008).

[11] Hauri P and Schneider U, "Whole-body dose and energy measurements in radiotherapy by a combination of LiF:Mg,Cu,P and LiF:Mg,Ti," Zeitschrift für Medizinische Physik (2017).

[12] Wrixon AD, "New ICRP recommendations," Journal of Radiological Protection **28**, 161 (2008).

[13] Davis SD, Ross CK, Mobit PN, Zwan LVd, Chase WJ, and Shortt KR, "The response of LiF thermoluminescence dosemeters to photon beams in the energy range from 30 kV X-rays to Co-60 gamma rays," Radiation Protection Dosimetry **106**, 33–43 (2003).

Chapter 4

Whole-body dose equivalent is similar for $6\,\mathrm{MV}$ and $15\,\mathrm{MV}$ intensity-modulated radiotherapy

Pascal Hauri[1,2] and Uwe Schneider[1,2]

[1] Institute for Radiotherapy, Radiotherapie Hirslanden AG, Aarau, Switzerland
[2] Department of Physics, University of Zurich, Zurich, Switzerland

This chapter is in preparation for a submission

Purpose: To investigate the difference in whole-body dose equivalents between 6 MV and 15 MV image guided radiotherapy (IGRT) treatments of a rhabdomyosarcoma in the prostate by using analytical dose models.

Methods: An analytical neutron dose model was developed to calculate the neutron dose equivalent for a radiotherapy patient. The model used the measured neutron dose close to the surface to project the dose into the patient by utilizing Monte Carlo (MC) simulated neutron spectra from the literature. A previously developed model for stray radiation of the primary beam was improved and used to calculate the photon out-of-field dose. The dose calculate by the treatment planning system was fused with the model calculated out-of-field dose resulting in a whole-body photon dose distribution. A daily cone beam CT dose was added to the neutron and photon dose equivalents. The calculated 3D dose distributions were compared to independent measurements conducted with thermoluminescence dosimeters (TLDs) and an anthropomorphic phantom. The photon dose was measured using LiF TLDs (TLD100, TLD100H, TLD700, and TLD700H). To measure the neutron dose contribution, the photoneutron fluence was registered via the TLD600 (n, α)-reaction and converted to neutron dose equivalent using MC simulate neutron spectra from the literature. The dose contributions from the IGRT treatments of three different modalities applied with two nominal X-ray energies were compared using dose equivalent volume histograms (DEVHs).

Results: The calculated out-of-field whole-body dose equivalents for the IGRT treatments agreed within $(9 \pm 10)\,\%$ (mean and type A standard deviation) compared to the measurements. The neutron dose equivalent was a minor contribution to the total out-of-field dose up to 50 cm from the isocenter. Further from the isocenter, head leakage was dominating inside the patient body whereas the neutron dose equivalent contribution was important close to the surface. There were small differences between the whole-body DEVHs of the 6 MV and 15 MV treatments applied with the same modality, although the out-of-field dose contributions showed large differences between the two beam energies. The patient volume in the low dose region (5 % of the prescribed dose), received a higher dose for the intensity-modulated radiation therapy (IMRT) treatments compare to the 3D-conformal treatments. Furthermore, in the low dose region, the dose of the volumetric-modulated arc therapy (VMAT) treatment was significantly lower compared to the dynamic IMRT treatment.

Conclusion: The calculated whole-body dose helped to understand the importance of the dose contributions in different areas of the patient. Regarding patient protection for IGRT treatments, the choice of beam energy is not important whereas the therapy modality has a large influence on the out-of-field dose. If the patient is treated with intensity-modulated beams, VMAT should be used instead of dynamic IMRT. The general models for photon and neutron dose equivalent calculation can be used for any patient geometry, tumor location and linear accelerator.

Keywords: Out-of-Field Dose, Radiotherapy, 15 MV, 6 MV, Neutron Dose Equivalent, CBCT

I. INTRODUCTION

Around 10 % of long-term cancer survivors develop a second tumor. 10 % of these second tumors are induced by the radiation treatment the patient received [1]. Most second cancers occur at the peripheral region where the dose is grater than 3.0 Gy [1]. However, Diallo et al. [2] identified an peak frequency in second malignant neoplasm for volumes that received a dose smaller than 2.5 Gy. However, this study was not limited to radiation induced second cancers. In external radiation beam therapy, the treated volume gets a high dose while the remaining body obtains a low dose bath. However, the untreated patient volume can be orders of magnitude larger than the treated volume. Usually, the dose is calculated around the threated volume and neglected in the rest of the patient body. However, with the whole-body dose the cancer risk could be estimated and used for treatment planning optimization.

The exposure of pregnant patients can have many negative effects for the fetus. These negative effects can be substantially minimized if the dose to the fetus is reduced to 100 mGy [3]. However, there are missing practical analytical models to estimated the fetal dose for novel treatments like intensity-modulated photon therapy [1].

Takam et al. [4] presented the current status of out-of-field neutron and leakage dose in radiation therapy and the associated risk for the patient. They reported an indication of out-of-field radiation-induced second caners. However, most of the reported treatments occurred decades ago such that studies of novel treatment machines are urgently needed.

For the same modality applied with different nominal X-ray energy, the target coverage, conformity, and homogeneity of the treatments are similar [5]. Hence, the choice of nominal X-ray energy should also be based on patient protection issues. Multiple studies investigated the difference in the peripheral dose between high (≥ 10 MV) and low nominal X-ray energy (< 10 MV) [6–10]. A Monte Carlo (MC) study made by Kry et al. [6], showed a similar photon out-of-field dose for 6 MV compared to 18 MV intensity-modulated radiation therapy (IMRT) treatments. For the nine organ locations investigated, the simulated neutron doses were typically much lower than the corresponding photon dose. However, they warranted an improved neutron dosimetry in order to achieve superior estimates. Ruben et al. [7] measured the components of the out-of-field photon dose for 6 MV and 18 MV treatments. The neutron dose contribution was obtained from published data. They reported that X-ray energy dose not affect the total photon scatter for the same modality. However, the additional neutron dose for 18 MV possible increased total body cancer risk compared to 6 MV IMRT treatments. Nevertheless, they could not draw a firm conclusion.

With increasing number of treatments using volumetric-modulated arc therapy (VMAT) and similar dose distributions of VMAT compared to IMRT treatments, the question arises about the difference in the out-of-field dose between the two modalities. To our knowledge, there is no study comparing the peripheral dose of high energy VMAT treatments with IMRT treatments.

In the current study we investigate the difference between the dose equivalent of 6 MV and 15 MV treatments. It is per se not clear that for a 15 MV X-ray nominal beam energy the out-of-filed dose will be smaller in comparison to 18 MV because of reduced photoneutron production. Compared to photons, neutrons are a minor part of the total out-of-field dose equivalent [1]. Howell et al. [8] reported a higher effective dose for 15 MV compared to 18 MV 3D-conformal radiation therapy (3DCRT) treatments.

Most of the neutron measurements reported in the literature were made in air [1, 8, 11–13] from which ambient neutron dose equivalent can be derived. Ambient neutron dose equivalent is an operational quantity for a conservative estimation of dose equivalent received by an individual. This leads to an overestimation of the true dose equivalent anywhere in the patient [1]. More sophisticated measurements are needed to measure the specific localized neutron dose in the patient. Furthermore, no analytical photoneutron model is available for a fast estimation of the neutron dose in the patient [1].

The use of X-ray imaging modalities can give a substantial dose to the patient [14, 15]. The choice of treatment technique and indication determines the image modality and therefore, the additional amount of dose to the patient. For patient positioning, the imaging dose is justified by the reduction of the margins around the target. A smaller planning target volume will lead to a sparing of the organs at risk. Hence, for image guided radiotherapy (IGRT) treatments, the patient receive an additional dose due to X-ray imaging. In this study we investigated the treatment of a rhabdomyosarcoma in the prostate. For each treatment fraction, the patient was assumed to be positioned with a full trajectory cone beam CT (CBCT) of the pelvis. Hence, we assigned a relative high imaging dose for the IGRT treatments. By investigating all contributions of the whole-body dose for an IGRT treatment, a better understanding in patient protection was achieved.

In the current study we investigate the whole-body dose equivalent for 6 MV and 15 MV IGRT treatments of a rhabdomyosarcoma in the prostate applied with three different modalities (3DCRT, IMRT, and VMAT). To access the neutron dose in the patient for the 15 MV treatments, a simple neutron dose model was developed. The off-axis photon dose of the treatments was calculated with a stray dose model. For this, a previously developed model of stray dose calculation for 6 MV static and intensity-modulated treatments was improved and adapted for 15 MV. The calculated stray dose was fused with the dose calculated by the treatment planning system (TPS) resulting in a whole-body photon dose. The calculated dose distributions were compared to independent LiF thermoluminescence detectors (TLD) measurements. An anthropomorphic Alderson phantom was loaded each time with new TLDs to measure the whole-body treatment doses. To correct the TLDs for the response with photon radiation energy, the mean energy at each measurement location was analytically calculated. The calculated neutron dose was compared to independent measurements made with a new method to determine the neutron dose equivalent. A daily CBCT dose was added to the photon and neutron dose equivalent. The resulting whole-body dose distributions of the six IGRT treatments were compared using dose equivalent volume histograms (DEVHs).

II. METHODS AND MATERIALS

In this manuscript, the indexes m, c, and s describe quantities which were derived either by measurements, calculations, or MC simulations, respectively. The abbreviations n stands for neutrons and γ for photons.

A. Whole-body photon and neutron dose models

Dose models were developed for radiotherapy photons, CBCT imaging and photoneutrons to obtain the whole-body dose of a treatment (see Fig. 1). In this work, dose calculations were preformed for an anthropomorphic Alderson phantom using a whole-body grid with a voxel dimension of $0.2 \times 0.2 \times 0.5\,\mathrm{cm}^3$. However, the radiotherapy photon and neutron dose models are generally applicable to any 3D-patient data set.

1. Neutron dose

The out-of-field neutron spectra and the fluence are not substantially affected by the off-axis distance, SSD, or field sizes [1]. However, neutron dose shows a strong decrease with increasing depth in the patient [16]. Based on this observations we developed a whole-body neutron dose model.

The bulk of neutrons are produced in the primary collimator [1]. In this work, we assumed a point source of neutrons in the X-ray producing target which is in close proximity of the primary collimator. Furthermore, the neutron trajectories in air were assumed to be straight lines (similar to photons). The photoneutron dose equivalent close to the surface was measured for a TrueBema operated at 15 MV (see Appendix VI B). For the gantry angle of a treatment field, the surface of the patient which is directly penetrated by the neutron trajectories was identified and the measured photoneutron dose was assigned. Afterwards, the assigned dose was projected into the patient by correcting for the decrease in dose resulting from the MC

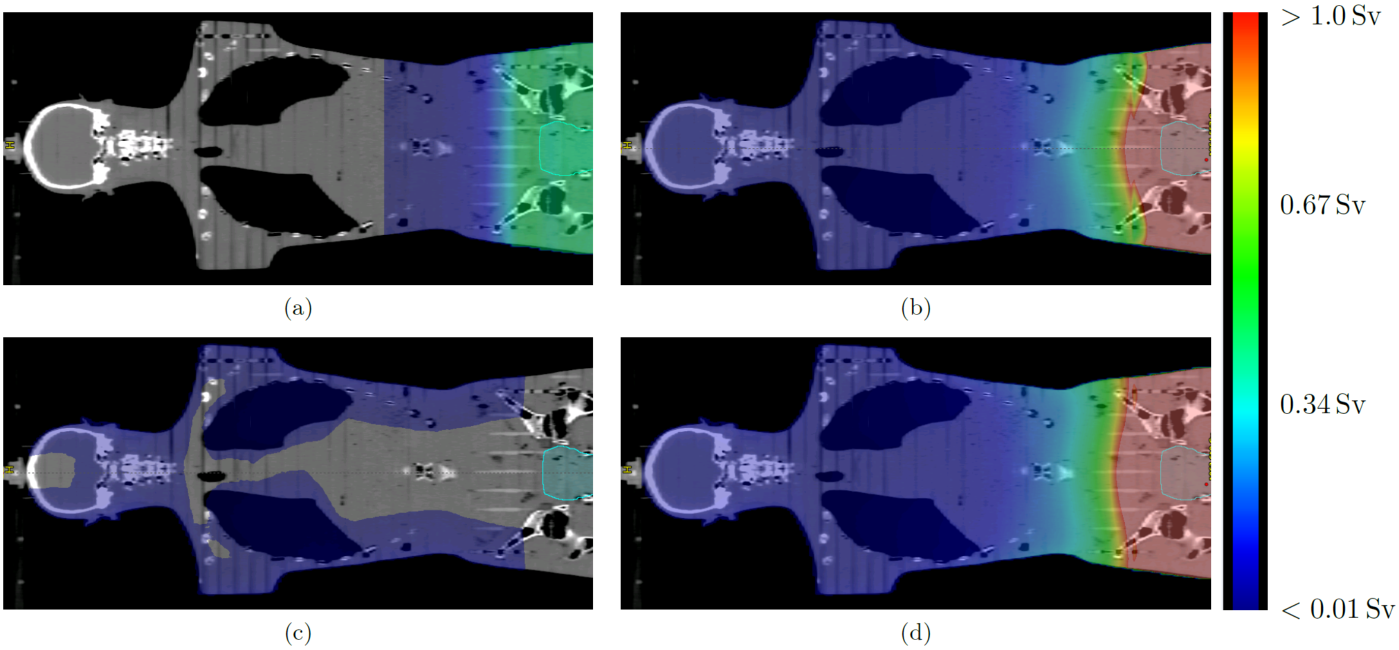

FIG. 1. The whole-body dose equivalent for the 15 MV IMRT treatment with a daily CBCT. The dose equivalent is shown for (a) neutrons, (b) photon scatter radiation fused with the TPS calculation, (c) 23 times a CBCT and (d) the summation of (a)-(c). The Fractionation scheme is presented in Table I. Furthermore, the outline of the rhabdomyosarcoma in the prostate can be seen.

simulated change in the neutron spectra [16].
The measured neutron dose equivalent was projected into the patient by,

$$H^n_{l,plan,c} = \frac{\sum_F H^n_{l,tissue,s}(d_F)\cdot \mathrm{MU}_F}{H^n_{tissue,s}(0.1\,\mathrm{cm})}\cdot H^n_{0.1\,\mathrm{cm},water,m}\cdot \mathrm{MU}_{plan} =: \frac{H^n_{l,plan,s}}{H^n_{tissue,s}(0.1\,\mathrm{cm})}\cdot H^n_{0.1\,\mathrm{cm},water,m}\cdot \mathrm{MU}_{plan}. \tag{1}$$

with $H^n_{l,plan,c}$ the calculated neutron dose equivalent in soft tissue (ICRU) for each voxel l. $H^n_{l,tissue,s}(d_F)$ is the predicted neutron dose equivalent per MU of a treatment field F. MU_F are the MUs normalized to the total MUs per treatment (MU_{plan}). $H^n_{l,tissue,s}(d_F)$ was calculated using the absolute neutron spectra in soft tissue simulated by Kry et al. [16] (Eq. 11). $H^n_{l,plan,s}$ is the predicted neutron dose per MU in a voxel l for a specific treatment. $H^n_{tissue,s}(0.1\,\mathrm{cm})$ is the neutron dose equivalent per MU in a depth of 0.1 cm soft tissue calculated with the absolute spectrum simulated by Kry et al. [16] (Eq. 11). $H^n_{0.1\,\mathrm{cm},water,m}$ is the neutron dose equivalent normalized to one MU measured in 0.1 cm depth of a $30 \times 30 \times 30\,\mathrm{cm}^3$ water-equivalent slab phantom [RW3, 2400 MUs, MLCs and jaws closed, SSD = 100 cm, 25 cm from central field axis (CAX)]. The difference in the simulated off-axis neutron dose close to the surface was below 3 % between soft tissue and water. Hence, the measured neutron dose in water was a good estimation of the dose in soft tissue. An extensive description of the neutron dose measurements can be found in Appendix VI B.
The depth in the phantom (d_F) of the field F was calculated using a straight line connecting the X-ray producing target and the voxel l. For the 3DCRT and the IMRT treatments, the calculation of the whole-body neutron dose equivalent was straight-forward since there was no gantry rotation during the beam on time. For the VMAT treatment, the neutron dose was calculated by grouping the control points of the one arc plan to six fields [17]. The resulting 3D out-of-field neutron dose equivalent of the IMRT treatment can bee seen in Fig. 1(c).

2. *Photon therapy dose*

A previously developed photon stray dose model for static and intensity-modulated 6 MV treatments [17], was improved and adapted for 15 MV (see Appendix VI A). The algorithm calculated the whole-body out-of-field dose of the coplanar treatments starting 4 cm longitudinal from the treatment volume. According to [1], the differences between TPS and measurements exceed 30 % of the local dose as close as 3 cm from the field edge, and differences increase by orders of magnitude at greater distances [18, 19]. At 4 cm longitudinal from the treatment volume, the dose of the TPS (Varian Eclipse, AAA-algorithm version 13.6.23) was fused with the model-calculated 3D out-of-field dose resulting in a whole-body photon dose [see Fig. 1(b)].

3. *Photon imaging dose*

The mean absorbed CBCT dose per Alderson slice was calculated using the average of the TLD dose measurement in the corresponding slice. The TLD measurements of the full trajectory pelvis CBCT are reported in [15]. The absorbed dose per voxel of a CBCT scan was calculated by interpolating the average CBCT dose per Alderson slab along the medial patient axis (MPAX). Therefore, the dose was the same for all voxels in a transversal dose-grid slice [see Fig. 1(a)]. According to Schneider et al. [20], the dose along the MPAX is in satisfying agreement with the average of the three-dimensional dose distribution in each Alderson slice.

4. *Whole-body dose*

To obtain a typical IGRT treatment dose, a daily CBCT 3D dose was added to the 3D photon dose per session. Furthermore for the 15 MV treatments, the neutron dose equivalent per session was added to the photon dose. The voxel-specific dose equivalents per session were multiplied with the number of sessions (see Table I), resulting in the 3D dose equivalent per treatment [see Fig. 1(d)].

TABLE I. The total treatment dose, total MUs, and MUs per treatment Gy. The treatments were planned by an experienced worker according to a strict protocol [21].

Plan	Treatment dose × fractions	Beam	Total MUs	MUs per treatment Gy
3DCRT	2.0 Gy × 26 = 52 Gy	6 MV	7326 MUs	141 MUs/Gy
		15 MV	5846 MUs	112 MUs/Gy
IMRT	2.2 Gy × 23 = 50.6 Gy	6 MV	22 989 MUs	454 MUs/Gy
		15 MV	21 661 MUs	428 MUs/Gy
VMAT	2.2 Gy × 23 = 50.6 Gy	6 MV	13 409 MUs	265 MUs/Gy
		15 MV	11 847 MUs	241 MUs/Gy

B. Whole-body TLD measurements

LiF TLD-chips (4.5 mm diameter, 0.6 mm thickness, Harshaw, Thermo Fisher Scientific, Waltham, MA) were used to measure the in- and out-of-field dose of external beam therapy. For TLD100 (LiF:Mg,Ti) and TLD100H (LiF:Mg,Cu,P), the same thermal treatment, calibration procedure and readout was used as described by Hauri and Schneider [22]. The thermal treatment, calibration procedure and readout for TLD600/700 (LiF:Mg,Ti) and TLD700H (LiF:Mg,Cu,P) were the same as used for TLD100 and TLD100H, respectively. For each TLD, an individual photon dose-to-water calibration factor [mGy/count] was determined with a 6 MV nominal X-ray energy irradiation applied with a TrueBeam linear accelerator (Varian Medical Systems, Palo Alto, CA). All absolute photon dose measurements [mGy] were correlated to a Farmer Chamber 30013 (PTW, Freiburg, Germany). The irradiations and detector readouts were performed according to a strict protocol presented in [22] to ensure consistency of the measurements.

The measured whole-body radiotherapy photon and neutron dose served as an independent verifications of the photon stray dose and neutron model.

1. *Treatment intention, planning, and irradiation*

The treated volume of this study was a rhabdomyosarcoma in the prostate for an adolescent patient (see Fig. 3). The planning CT of an anthropomorphic phantom (Alderson-Rando, RSD Radiology Support Devices, Long Beach, CA) as well as the contouring of the treated volume structures and organs were preformed at one hospital.

The treatment planning of the 6 MV and 15 MV 3DCRT (four field box), IMRT (five fields with dynamic MLCs), and VMAT (one arc) treatments was done using the Eclipse TPS. All treatments were planned by an experienced worker. A detailed description of the treatments and the strict planning guidelines can be found in Hälg et al. [21]. The 3DCRT treatments

included a sequential boost and the intensity-modulated treatments an integrated boost.
The diameter of the pelvis CBCT was 46.5 cm in a transversal slice and a field-of-view of ±8.75 cm from isocenter in the longitudinal direction. The CBCT protocol (version 2.5.28.0, half fan type, full trajectory, $125\,\mathrm{kV_p}$, 1080 mAs) was given by the vendor.
Using a conventional linear accelerator equipped with an on-board imaging system (TrueBeam), the six treatments and the CBCT were irradiated onto the Alderson phantom each time loaded with new TLDs. The phantom was positioned head first supine. For the 6 MV treatments and the CBCT scan, each measurement location in and on the phantom was equipped with a TLD100H stacked on top of a TLD100. For the 15 MV treatments, each measurement location was loaded with a TLD700H stacked on top of a TLD600. Confetti (made out of normal paper) were placed between all (TLD600,TLD700H)-pairs to avoid an α-particle contribution to the TLD700H signal originating from the $^6\mathrm{Li}(n,\alpha)$ capture. The measurement locations were distributed in the Alderson phantom according to Hälg et al. [21, 23]. Additionally, for the 15 MV treatments, the out-of-field photon dose of the skin was measured along a line from the bellybutton to the nose in steps of 10 cm. For this, the TLD700H were loaded in empty pill casings made of PMMA simulating the thickness of the skin. All absolute photon dose measurements were correlated to a Farmer Chamber 30013 since the chamber was used to determine the in-field TLD-calibration dose.

2. Photon dose of the CBCT and 6 MV *treatments*

The in- and out-of-field photon dose of the 6 MV treatments and the CBCT were measured separately using a combination of TLD100 and TLD100H chips. The two TLD types show a difference in response with photon radiation energy [24, 25]. For the dose measurements, a TLD100H chip was put on top of a TLD100 chip. The doses measured by the TLD100 and TLD100H were evaluated by using individual photon dose calibration factors. The correction factors for the response with photon radiation energy was found by the ratio of the TLD100 divided by the TLD100H dose. A comprehensive description of photon dose and the mean energy measurements for the CBCT and the 6 MV treatments is given in Hauri and Schneider [22]. Furthermore, a detailed description of the uncertainties in photon dose and mean photon energy is presented.

3. Photon dose of the 15 MV *treatments*

TLD100 contains the natural abundance of ^{6}Li and ^{7}Li while TLD600 contains primarily ^{6}Li. According to Schwahofer et al. [25], TLD600 and TLD100 show the same response with photon radiation energy since the number of neutrons in Li does not affect the energy bands of the TLD crystal. For the same reason, it was assumed in this manuscript, that there is no difference in the response with photon radiation energy between TLD100H and TLD700H.
The whole-body photon dose of the 15 MV treatments was determined for 189 locations in the Alderson phantom. The detected out-of-field photon dose of each TLD700H was corrected for the response with photon radiation energy. The individual correction factors were estimated by using the photon scatter contribution at each measurement location in the phantom. The total out-of-field dose consists mainly of three contributions: patient scatter, collimator scatter, and head leakage [7, 17, 26]. In the middle of a $30 \times 30 \times 30\,\mathrm{cm}^3$ water-slab phantom (SSD = 85 cm), the mean energy of the three scatter contributions were measured using a combination of TLD700 and TLD700H and the method described in [22]. For a $10 \times 10\,\mathrm{cm}^2$ field (defined by the MLCs), the mean energy of patient scatter was measured at 15 cm distance to the field edge. For the same field size, the mean energy of collimator scatter was determined at 15 cm and 35 cm distance from the field edge. At the same locations, the mean energy of head leakage was measured for closed jaws and MLCs. The separation of a field measurement into the three scatter contributions is described by Hauri et al. [17]. A previously developed 6 MV out-of-field dose model [17] was improved and adapted for 15 MV (see Appendix VI A). Using the adapted model, the dose of patient scatter, collimator scatter, and head leakage was calculated for each measurement location l in the phantom. The final out-of-field mean energy ($\overline{E}^{\gamma}_{l,c}$) was determined by,

$$\overline{E}^{\gamma}_{l,c} = \frac{1}{\sum_i D^{\gamma}_{i,l,c}} \sum_i D^{\gamma}_{i,l,c} \cdot \overline{E}^{\gamma}_{i,m}, \tag{2}$$

with $i = \{\text{patient scatter, collimator scatter, head lekage}\}$. $D^{\gamma}_{i,l,c}$ is the dose at the measurement location l and $\overline{E}^{\gamma}_{i,m}$ the mean energy of the scatter contribution i.
The calculated out-of-field mean energies together with the method presented in [22] were used to determine the individual correction factors for the response with photon radiation energy of the single TLDs. The multiplication of individual correction factors with the TLD700H-detected dose resulted in the final photon dose.
As a consistency check, the same method to calculate the TLD700H correction factors for the response with photon radiation energy of the 15 MV treatments was used for the three 6 MV treatments. In contradiction to the 15 MV measurements, the mean photon energies for the 6 MV treatments were explicitly measured as can be see in [22]. Using Eq. 2, the mean photon energy was calculated for each measurement location. The calculated and measured mean energies were converted to correction factors as described in [22]. The calculated and measured correction factors for the 6 MV treatments were

compared to estimate the uncertainty in the TLD700H photon dose measurement for the 15 MV treatments.

4. *Neutron dose equivalent of the* 15 MV *treatments*

A combination of TLD600 and TLD700H was used to measure the whole-body neutron dose equivalent of the 15 MV treatments. With a spectra-dependent correction factor (including fast neutrons), the measured neutron signal of a TLD600 was converted to neutron dose equivalent. This conversion is described in detail in Appendix VI B. TLD700H is not affected by neutrons in the energy range of interest [27]. TLD600 will register photons and neutrons. The neutron signal detected in the phantom was corrected for the photon contamination (see Eq. 8) The measured neutron signal ($R^n_{l,m}$) was converted to a neutron dose equivalent in soft tissue ($H^n_{l,m}$) using the neutron spectra-dependent conversion coefficient ($K^n_{l,plan,s}$),

$$H^n_{l,m} = \frac{\sum_F H^n_{l,tissue,s}(d_F) \cdot \mathrm{MUs}_F}{\sum_F R^n_{l,tissue,s}(d_F) \cdot \mathrm{MUs}_F} \cdot R^n_{l,m} =: \frac{H^n_{l,plan,s}}{R^n_{l,plan,s}} \cdot R^n_{l,m} =: K^n_{l,plan,s} \cdot R^n_{l,m}. \tag{3}$$

The index F represents the different fields per treatment with the corresponding gantry angle and MUs_F per field. The depth in the phantom (d_F) of the field F was calculated using a straight line connecting the X-ray producing target and the TLD-location l. The bulk of neutrons are produced in the primary collimator [1]. In this work, we assumed a point source of neutrons in the X-ray producing target which is in close proximity to the primary collimator. $H^n_{l,tissue,s}(d_F)$ and $R^n_{l,tissue,s}(d_F)$ is the predicted neutron dose equivalent and the predicted neutron signal per MU of a treatment field F, respectively. $H^n_{l,tissue,s}(d_F)$ (see Eq. 11) and $R^n_{l,tissue,s}(d_F)$ (see Eq. 9) were calculated using the absolute neutron spectra in soft tissue simulated by Kry et al. [16]. $H^n_{l,plan,s}$ is the predicted neutron dose equivalent and $R^n_{l,plan,s}$ is the predicted neutron signal of a specific treatment for the TLD-location l.

Kry et al. [16] simulated the neutron spectra in soft tissue. The Alderson phantom was assumed to be soft tissue-equivalent (ICRU) with the exception of the lungs. For the lungs a mass density of $0.25 \times \rho_{\text{soft tissue}}$ was assumed (relative hydrogen contend in lungs compared to soft tissue = 25 % [28]). For the 3DCRT and the IMRT treatments, the calculation of the depth in the phantom was straight forward since there was no gantry rotation during the beam-on time. For the VMAT treatment, the control points of the one arc were grouped to six fields with different gantry angles and corresponding MUS per field . A more detailed description of the approximation of the VMAT plan by discrete fields can be found in [17].

The neutron dose equivalents of the coplanar treatments were measured only outside the treatment volume. This had two reasons. First, the neutron dose equivalent inside the primary X-ray beam can be neglected compared to the dose resulting from photons [29, 30]. Second, by using TLD600, it was not possible to resolve the signal resulting from neutrons since the signal from photons was orders of magnitude higher in and close to the treated volume [31].

III. RESULTS

Unless otherwise stated, the mean and one standard deviation (σ) are presented. According to [32], type A is standing for the measured σ and the type B for the estimated σ.

A. Whole-body dose equivalent

1. *Photons*

The deviation between the calculated whole-body dose and the 183 point-dose measurements of the CBCT scan was $0 \pm 14\,\%$ (type A). This justifies the presented method to calculating the whole-body CBCT dose.

The measured mean photon energies of the three stray dose contributions can be seen in Table II. Within the measurement uncertainties, there was no difference in the mean energies of the scatter contributions between the 15 MV and 6 MV field measurements. The measured mean energy of head leakage was the same at 15 cm and 35 cm distance from the field edge. For a nominal X-ray energy of 15 MV, the mean energy of collimator scatter changes from > 1.1 MeV at 15 cm to 0.5 MeV at 35 cm distance from the field edge. A similar change in the mean energy of collimator scatter was noticed for the 6 MV nominal X-ray energy. However, close to the field edge patient scatter is the dominating scatter contribution [17, 26], whereas the biggest contribution of collimator scatter relative to the other contributions is at around 35 cm distance to the field edge (see Fig. 9). Hence, the mean energy of collimator scatter determined at 35 cm was used to calculate the final out-of-field mean energy for every measurement location (see Eq. 2).

Over all out-of-field TLD measurement locations of the three 6 MV treatments, an average mean photon energy of (0.40 ± 0.07) MeV (type A) was measured. For the same locations, an average mean photon energy of (0.40 ± 0.03) MeV (type A) was calculated. For the 15 MV treatments, an average mean photon energy of (0.47 ± 0.05) MeV (type A) was calculated.

TABLE II. The measured mean energies $(\overline{E}^{\gamma}_{i,m})$ with the type B uncertainty of the mean $(\sigma/\sqrt{n})$ for $i =$ patient scatter (ps), collimator scatter (cs), and head leakage (hl). The uncertainties were calculated according to [22].

Nominal X-ray energy	$\overline{E}^{\gamma}_{i,m}$ [MeV]		
	ps	cs	hl
6 MV	(0.28 ± 0.03)	(0.62 ± 0.07)	(0.35 ± 0.03)
15 MV	(0.29 ± 0.03)	(0.53 ± 0.04)	(0.45 ± 0.04)

Hence, the TLD measurements of the 15 MV treatments needed similar corrections for the response with photon radiation energy compared to the 6 MV treatments [22].
For the 6 MV plans, the deviation between the calculated and measured correction factors for the TLD100 response with photon radiation energy was (0 ± 1) % (type A). For TLD100H, the deviation between calculation and measurement was (-1 ± 1) % (type A). Using Gaussian error propagation, the uncertainty in the TLD700H dose measurement was determined as ±2 % (type B) ($\sigma = \pm 2$ % (type B) from the correction factor and $\sigma = \pm 1$ % (type A) from the uncorrected TLD700H dose measurement [22]).
In Fig. 2 the different out-of-field dose contributions for a VMAT treatment can be seen. For the 6 MV treatment, patient scatter was the largest out-of-field dose contribution. For 15 MV, collimator scatter was more important compared to patient scatter, Furthermore, the CBCT reached dose levels comparable to collimator scatter.

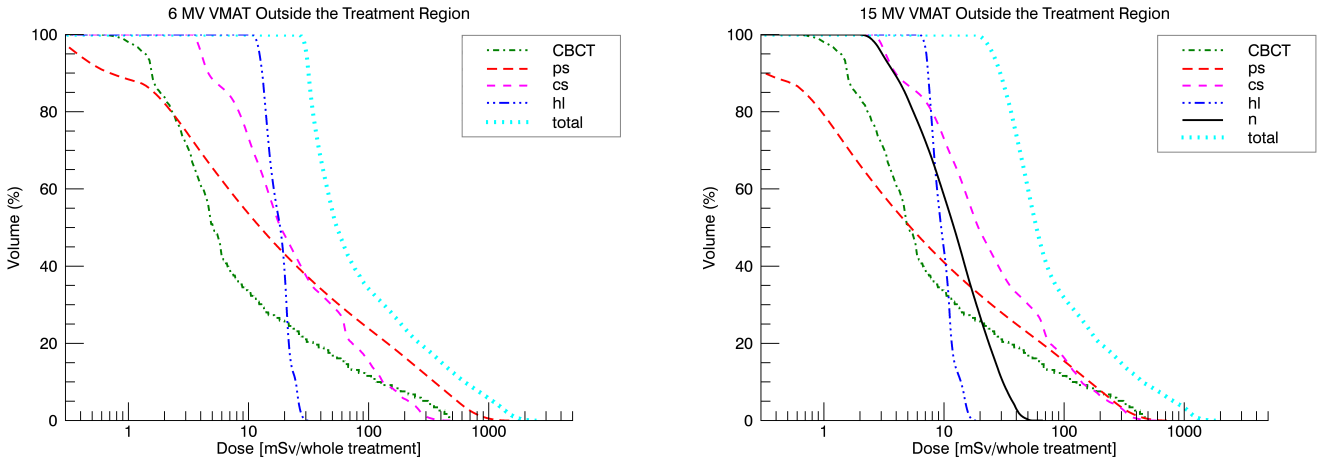

(a)

(b)

FIG. 2. All out-of-field dose contributions (CBCT: 23 times a daily CBCT dose, ps: patient scatter, cs: collimator scatter, hl: head leakage, n: neurons dose equivalent) for the VMAT treatments of (a) 6 MV and (b) 15 MV nominal X-ray energy.

Over all 15 MV treatments (3DCRT, IMRT, and VMAT), the deviation between the algorithm-calculated whole-body out-of-field photon dose and the measurement was (8 ± 10) % (type A). The deviation of the 6 MV treatments between algorithm-calculated and measured out-of-field photon dose was (10 ± 10) % (type A). The algorithm calculated the whole-body stray dose of the coplanar treatments starting 4 cm outside the treatment volume. The photon dose calculated by the TPS was compared to the measurement of the transversal Alderson phantom slices located 3 cm and 6 cm from the treatment volume. In the out-of-filed region, the deviation between the TPS-calculated and measured photon dose for the three 15 MV and three 6 MV treatments was (-5 ± 21) % (type A) and (8 ± 11) % (type A), respectively. For the same measurement locations, the deviation between the algorithm-calculated and the measured photon dose was (-10 ± 13) % (type A) and (-1 ± 15) % (type A) for the 15 MV and 6 MV treatments. The agreement between the algorithm-/TPS-calculated compared to the measured photon dose in the region where the two dose distribution were fused justified the combination of the TPS with the algorithm. The fused photon dose compared to the measurement along the MPAX can be seen in Figs. 9(b)-(c). In the same figures the measured photon skin dose for the 15 MV treatments along a line from the bellybutton to the nose is plotted. For all treatments, the VMAT showed the largest and the IMRT the smallest skin dose relative to the measured dose along the MPAX. The improved stray dose algorithm underestimated the skin dose close to the field edge by a factor of two.

2. Neutrons

Using the semi-empirical neutron model (Eq. 1), the neutron dose equivalent measured for 15 MV in 0.1 cm water [$(0.69 \pm 0.14)\,\frac{\mathrm{mSv}}{100\,\mathrm{MUs}}$ (type B)] was projected into the body. In Fig. 3, the measured and calculated neutron dose equivalent along the MPAX can be seen. The calculation and measurements were in good agreement. The large photon signal relative to the neutron signal close to the treated volume resulted in a large uncertainty in the neutron dose equivalent . However, the uncertainty resulting from the photon contamination was below ±10 % (type B) for locations more than 3 cm from the treated volume. For locations 3 cm from the treated volume, the uncertainty in the measured neutron dose equivalent was below ±30 % (type B). The estimation of the uncertainties in neutron dose equivalent measurement can be found in Appendix VI B. The difference between the calculated neutron dose equivalents and whole-body out-of-field measurements was 18 ± 27 % (type A) for the three 15 MV treatments.
The calculated and measured neutron dose equivalent showed a strong dependence with depth. Furthermore, the calculation and the measurement were in agreement within the measurement uncertainties. There was no significant difference ($\alpha = 0.05$) in the measured neutron dose equivalent per 100 MUs along the MPAX between the 3DCRT, IMRT, and VMAT treatment. However, for measurement points close to the surface, the treatments showed significant differences in neutron dose equivalent. The neutron dose close to the surface was dependent of the gantry angles of the treatment fields. Furthermore, the neutron model overestimated the dose equivalent in the lungs.

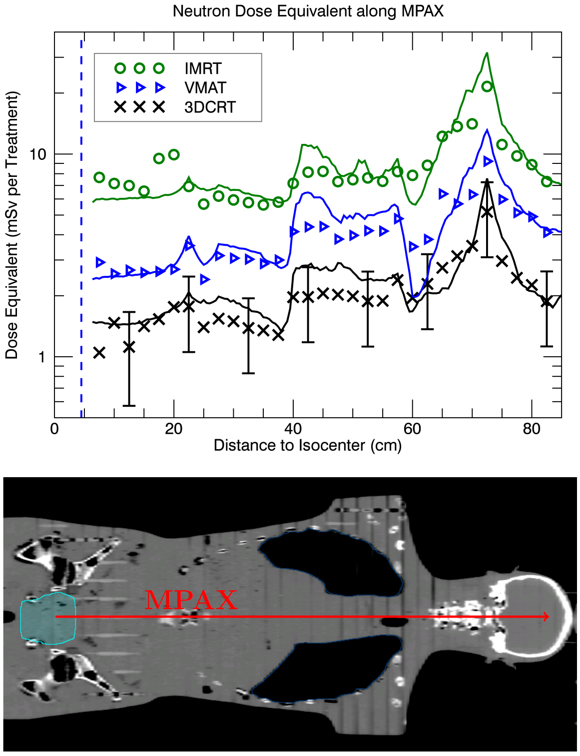

FIG. 3. The measured (points) and calculated (solid lines) neutron dose equivalent for the 3DCRT, IMRT, and VMAT treatments along the MPAX. For the measurements, a TrueBeam linear accelerator operated at 15 MV nominal X-ray energy was used. The 95 % confidence interval for the measured neutron dose equivalent (indicated by the error bars) decreased rapidly from ±100 % to ±40 % (type B) with increasing distance to the CAX. The dashed line indicates the edge of the treated volume. Furthermore, the Alderson phantom with the outline of the treated volume (rhabdomyosarcoma) in the hip region. The arrow represents the MPAX and is scaled to the upper figure.

3. Total dose equivalent

In Figs. 4(a) and (b), the out-of-field dose contributions and the total DEVH of the IMRT and the 3DCRT 15 MV treatments are plotted in a logarithmic scale. There was good agreement in the photon DEVH determined from the 151 out-of-filed measurement points and DEVH determined from the calculated photon dose. The DEVHs of the VMAT treatments (not plotted) were between the 3DCRT and the IMRT treatments. For all energies and treatment modalities, the photon stray dose of the primary beam was the biggest contribution to the total out-of-field dose. At the edge of the CBCT field-of-view, the daily CBCT dose reached levels comparable to the 3DCRT out-of-field dose [Fig. 4(b)].

In Figs. 4(c) and (d), the whole-body DEVH of the 6 MV and 15 MV treatments. For the same treatment modality, the DEVHs showed only small differences between the two beam energies.

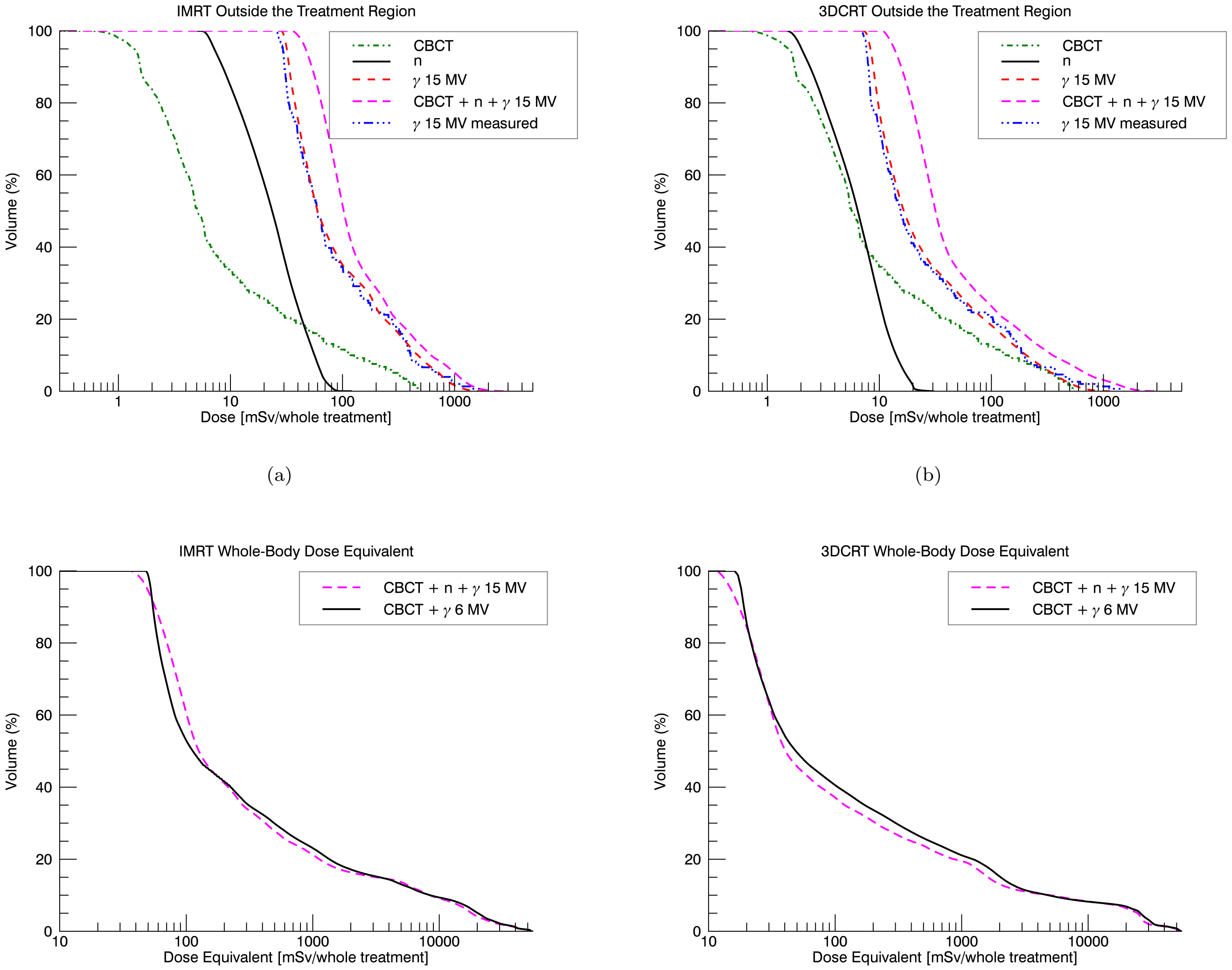

(a)

(b)

(c)

(d)

FIG. 4. Out-of-field dose equivalent volume histogram of the various contributions (CBCT: daily CBCT dose × number of treatment sessions, n: neutron dose equivalent, γ: photon dose) and the total dose for the 15 MV (a) IMRT and (b) 3DCRT plan per whole treatment. "γ 15 MV" indicates the whole-body photon dose. "γ 15 MV measured" was determined from the 151 out-of-field measurement locations distributed in the Alderson phantom. In (c) and (d), the in- and out-of-field whole-body DEVH for the 6 MV and the 15 MV treatments. In (c) for the IMRT and (d) for the 3DCRT treatment.

Outside the treated volume, the deviation between the measured and calculated final dose equivalent was $(10 \pm 11)\,\%$ (type A) and $(8 \pm 8)\,\%$ (type A) for the 15 MV and the 6 MV treatments, respectively. The measured uncertainty in the final dose equivalent was similar to the uncertainty in the stray photon dose since the stray dose was the biggest contribution of the total dose equivalent.

In Fig. 5 the whole-body DEVHs of the different modalities. In the high and intermediate dose region (> 3 Sv or 5 % of the prescribed dose), the DEVHs for the intensity-modulated treatments were similar. In the same dose region, the DEVHs of the 3DCRT treatments were different compared to the intensity-modulated treatments. The body volume in the low doses region (< 3 Sv) receives up to two times more dose for the VMAT compared to the 3DCRT treatments. For the IMRT treatments, the body receives up to four times more dose compared to the 3DCRT treatments.

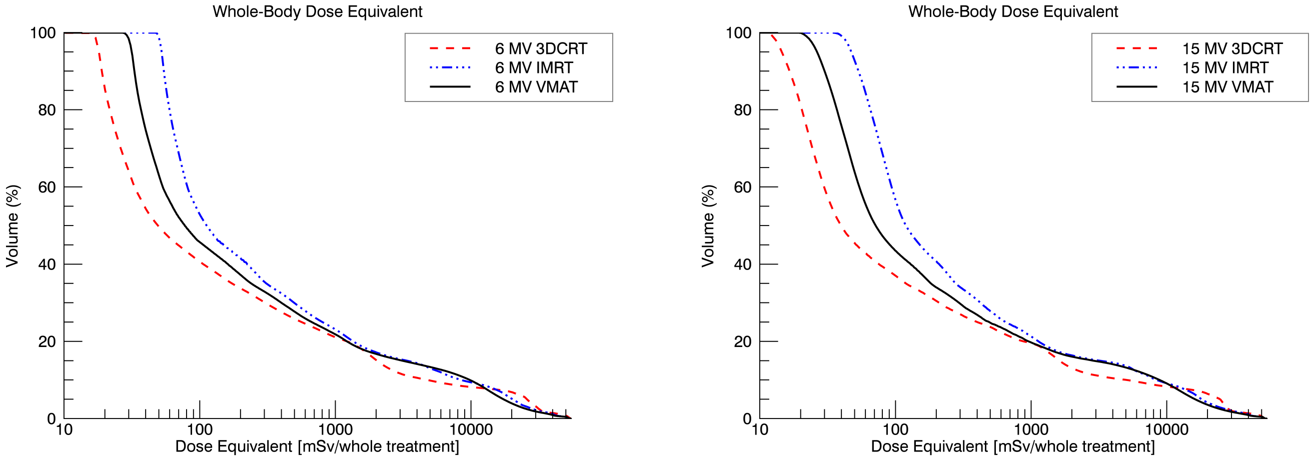

(a) (b)

FIG. 5. The whole-body DEVHs for (a) the 6 MV (b) the 15 MV treatments.

IV. DISCUSSION

The whole-body dose equivalent resulting from IGRT treatments of a rhabdomyosarcoma in the prostate was calculated for three different modalities (3DCRT, IMRT, and VMAT) and two nominal X-ray energies (6 MV, and 15 MV). The calculated 3D dose distribution was compared to whole-body TLD measurements. An algorithm to calculate the mean photon energy for each point in the patient was introduced. The measured mean photon energy at each TLD location agreed well with the calculated mean energy. Using the mean energy, the photon dose detected by TLDs was corrected for the response with photon radiation energy. The out-of-field dose was calculated with a previously developed model for photon scatter dose [17] which was improved for this work. The calculated out-of-filed dose was fused with the TPS-calculated dose resulting in a whole-body photon dose. For all treatment modalities and nominal X-ray energies, the whole-body dose agreed within (9 ± 10) % (type A) compared to the measured out-of-field photon dose. To access the 3D neutron dose of the 15 MV treatments, a simple neutron dose model was developed and compared to independent measurements. The whole-body TLD600 measurements were converted into neutron dose equivalent using MC simulated neutron spectra from the literature [16]. The calculated neutron dose agreed within (18 ± 27) % (Type A) compared to the measurements. A daily CBCT dose and the neutron dose equivalent were added to the whole-body photon dose of a treatment. For all modalities and nominal X-ray energies, the calculated whole-body dose equivalent agreed within (9 ± 10) % (type A) compared to the measured dose equivalent. The whole-body dose equivalent between the 6 MV and 15 MV treatments were compared using DEVHs. Small differences in the DEVHs were noticed for the treatments of different nominal X-ray energies applied with the same modality, although large difference in the scatter contributions were identified. Substantial deviations in the DEVHs between the three investigated modalities was seen. Hence, for patient protection, the choice of nominal X-ray energy plays a minor roll, whereas the treatment modality largely influences the out-of-field dose.

A. Photon dose

Close to the treated volume, the CBCT dose was a substantial contribution to the out-of-field dose resulting from a treatment (Fig. 4). In the field-of-view, the CBCT dose was almost constant [33]. Furthermore, the field-of-view extended around 4 cm over the boarder of the treated volume. In this area, the dose caused by scatter radiation of the primary beam dropped rapidly with increasing distance to the treated volume. The CBCT dose decreased exponentially with increasing distance to the field-of-view. Hence, a smaller field-of-view is beneficial regarding patient protection. However, a daily CBCT represented a conservative estimation of the imaging dose. The contribution of imaging to the total dose equivalent was similar for all investigated treatments since they had almost the same numbers of treatment sessions (see Table I). Hence, the results draw in this manuscript are valid even if the imaging dose is excluded. A detailed discussion of the CBCT dose in context of the treatment dose can be found in the literature [15].

The mean photon energies calculated/measured outside the treatment volume were in agreement with reported out-of-field mean energies for 6 MV and 15 MV treatment fields (field defined by the MLCs or IMRT fields) [34–36]. Kry et al. [34] simulated the same average photon energy (0.4 MeV) for a 6 MV field (defined by the MLCs) as we calculated/measured in the current work. Using the simulated average mean energy, they applied an overall correction factor for TLD100 to correct the out-of-field dose measurements. However, a general correction factor leads to a systematic error in dose [22, 35]. Patient scatter increases linearly with increasing patient thickness [17]. Hence, the off-axis photon energy close to the treated volume changes for different treatment locations in the patient. Using the method to calculate the mean photon energy, a systematic error in the dose correction can be avoided. The spectrum of patient scatter for a Simens Primus 6/15 linear accelerator was MC simulated by Chofor et al. [37]. In agreement with our work, a similar photon energy of patient scatter between 6 MV and 15 MV beams was reported. Photons of lower energies have an increased probability of large Compton scatter angles compared to high energy photons. Hence, particularly photons of lower energies from the primary X-ray spectrum causing patient scatter. For 6 MV and as well 15 MV beams, these low energy photons are present. However, compared to the main peak of the primary X-ray spectrum the number of low energy photons is increased for 6 MV compared to 15 MV. This explained the higher patient scatter of the 6 MV compared to 15 MV treatments.

Compared to the primary beam, the X-ray spectrum in the peripheral region is softer. Hence, an increase in organ-specific relative biological effectiveness (RBE) for carcinogenesis is expected [38]. With the presented method, the dose and corresponding mean photon energy can be calculated separately for patient scatter, collimator scatter, and head leakage. Hence, for every scatter contribution the RBE can be determined such that more accurate risk models can be developed.

Close to the field edge where patient scatter and collimator scatter were dominating (see Fig. 9), the 6 MV treatments showed a higher dose compared to the 15 MV counterparts. For a standard field, patient scatter was increased by a factor of two for 6 MV compared to 15 MV (Fig. 7) whereas collimator scatter was reduced just by a factor of 1.5 for 6 MV compared to 15 MV (Fig. 8). This factor was reduced further by the fact that collimator scatter scales with the applied MUs [17] and that the 6 MV treatments needed more MUs compared to the 15 MV counterparts (Table I).

Ruben et al. [7, 26] measured the components of the out-of-field dose for IMRT and 3DCRT fields up to a distance 40 cm from the isocenter. In agreement to our work, they reported an decreasing patient scatter dose for increasing nominal X-ray energy. Furthermore, they measured nearly the same 3DCRT out-of-field dose for 6 MV and 15 MV treatments. In their study, both 3DCRT treatments utilized the same MUs. We noticed an overall lower photon dose for the 15 MV compared to the 6 MV 3DCRT treatment. This can be explained by the reduced MUs for the 15 MV compared to the 6 MV treatment of our study.

The improved general model for stray dose calculation [17] predicted well the measured off-axis photon dose contribution in the anthropomorphic phantom. To our knowledge, this is the only analytical model for whole-body photon dose prediction for static and intensity-modulated treatments. An analytical model to calculate the out-of-field dose for intensity-modulated treatments was introduced by Sanchez et al. [36]. Their model is only applicable for distances $\geq$ 10 cm from the field edge because they neglected the patient scatter contribution. However, close to the field edge the largest out-of-field dose gradients are present. Furthermore, the TPS can not be used to calculate the out-of-filed dose up to 10 cm from the field edge since differences between TPS and measurements exceed 30 % of the local dose as close as 3 cm from the field edge [1], and differences increase by orders of magnitude at greater distances [18, 19].

An aspect of neutron interaction in the phantom is the production of capture gamma ray emission. The dose contribution from this emission can be neglected since it is relatively small compared to the scatter photon dose of the primary beam [30]. However, using TLD700H the capture gamma rays were measured together with the scatter photon dose. Furthermore, the capture gamma ray contribution was included in the predicted head leakage dose since the scatter dose model was adjusted using ionization chamber measurements (see Appendix VI A). The TLD700H measurements agreed well with the calculated stray dose in the off-axis region where head leakage was dominating [see Fig. 9(b)-(d)].

B. Neutron dose equivalent

The neutron dose was measured using a new method (see Appendix VI B). The signal from the (n, α) capture of the TLD600 was converted to a fictive photon dose signal using TLD-specific photon dose calibration factors. The converted signals were transformed into dose equivalents using neutron spectra-dependent conversion factors. The conversion factors were calculated by using a constant $(\overline{C})$, which linked the (n, α)-reactions per TLD600 volume to the converted neutron signal. $\overline{C}$ was measured for TLD600 chips. In contrast to the photon spectrum in radiation therapy, the thermal part of the neutron spectrum is strongly altered by TLD600. This results from the high (n, α) cross-section of ^{6}Li. Hence, the interior of the detector is shielded from thermal neutrons in a way that the value of $\overline{C}$ should be experimentally determined if other TLD600 shapes are used. However, photoneutron signals reported in the literature [9] could be retrospectively converted to neutron dose equivalent using the presented method (see Appendix VI B).

The neutron dose equivalent close to the surface was measured in water and used to calculated the dose in the phantom. The measured surface dose agreed with published data [13]. A discussion of the result for the measurement of the neutron dose equivalent in water can be found in Appendix VI B. The neutron model overestimated the neutron dose in the phantom body in average by 18 %. The overestimation was larger for the 3DCRT compared to the IMRT treatment. The 3DCRT treatments showed an average field opening of around $9 \times 10\,\text{cm}^2$ compared to an opening of $3 \times 10\,\text{cm}^2$ for the IMRT treatments. Howell et al. [39] reported a decreasing neutron fluence for an increasing field size. The MLCs are an additional source of photoneutron production [1]. Hence, the measurement of neutron dose for a closed field and projection into the patient represented a conservative estimation of the neutron dose equivalent.

The prediction by the neutron dose model was in an agreement with the measurements we aimed for in this work. This indicated a good estimation of the neutron spectrum at a certain measurement location in the phantom. Depth in tissue had a large effect on the neutron dose equivalent. Along the MPAX, the neutron dose peaked in the neck of the Alderson phantom for the calculation as well for the measurement (Fig. 3). In this area, the smallest depth in the patient was observable. The largest overestimation in neutron dose by the model compared to the measurements was seen in the lungs. A simple scaling with the density of the lungs was used to calculate the depth in the anthropomorphic phantom to predict the neutron spectra. However, no MC simulation was used to predict the neutron spectra in lung tissue. Wrong neutron spectra estimated in the lungs explain the overestimation in neutron dose. A higher assumed density for lung tissue would reduce the overestimation in dose. Furthermore, the path through the patient was calculated assuming a neutron pencil beam originating from the X-ray producing target. This assumption is to a great extend a simplification since in a treatment room photoneutrons have various sources of origin [1, 39]. Nevertheless, the neutron model showed an accuracy in dose equivalent we aimed for in this work. In order to use the model for other linear accelerators and nominal X-ray energies, the neutron dose close to the surface can be measured and projected into the patient.

Hälg et al. [29] measured the neutron dose equivalent using PADC detectors for the same treatment intention and treatment modalities as presented in the current work. For all treatments, the PADC detectors showed a systematic three times reduced neutron dose equivalent per 100 MUs compare to the results presented here. The deviation in the calibration procedure is assumed to be the reason for the systematic difference between the measurements.

The neutron dose per 100 MUs close to the surface showed a significant difference between the three 15 MV treatments (3DCRT, IMRT, VMAT). Close to the surface, the neutron dose was strongly dependent of the gantry angles of the treatment fields. Along the MPAX, there was no significant difference in the neutron dose equivalent between the three different modalities. Hence, the neutron dose equivalent inside the phantom scaled with the applied MUs independent of the treatment modality. This was not true for the neutron dose closer to the phantom surface.

C. Total dose equivalent

The DEVHs of the calculated photon stray dose were in good agreement with the DEVHs of the measurement (Fig. 4). Hence, the measurement locations represented well a whole-body photon dose. In comparison, DEVH of the calculated neutron dose equivalents showed more dose per volume compared to the DEVHs from the measurements. This can be explained by the fact that most of the TLD measurement locations are deeper than 1 cm in the phantom [21]. The locations were chosen such that they cover all ICRP-recommended organs [40]. The neutron dose decreases rapidly with increasing depth in the phantom [Fig. 1(a)]. However, most ICRP organs are not close to the patient surface. This relativized the high neutron dose contribution close to the surface.

For high and intermediate doses ($>$ 3 Gy or 5 % of the prescribed dose), the DEVHs for the same modality looked similar between the two nominal X-ray energies [Figs. 4(a) and (b)]. Hence, similar dose distributions were achieved in the target regions.

The out-of-field dose close to the treated volume was higher for the 6 MV compared to the 15 MV. Patient scatter and to a lesser extend collimator scatter are the dominating out-of-field dose contributions close to the treated volume. 6 MV nominal X-ray energy showed a two times increased patient scatter and a similar collimator scatter contribution compared to 15 MV (see Appendix VI A). This explained a higher DEVH of the 6 MV compared to the 15 MV treatments for the dose equivalent interval of 0.2-3 Sv [Figs. 4(c) and (d)]. At around 50 cm from the isocenter, head leakage and neutrons were the dominating out-of-field dose contributions [Figs. 9(b)-(d)]. Hence, for the doses interval $<$ 0.2 Sv, the differences in the DEVHs were dependent of the difference between head leakage of 6 MV compared to the sum of head leakage and neutrons dose of 15 MV. Head leakage and neutron dose scale linear with MU and are in first approximation independent of the field shape [1, 17]. The relative difference in MU for the 6 MV compared to the 15 MV treatment was smaller for the intensity-modulated treatments compared to 3DCRT treatments (see Table I). This explained the crossing of the 6 MV and 15 MV DEVHs for the intensity-modulated treatments at 0.2 Sv (see Fig. 4c). For the 3DCRT treatments the DEVH of the 15 MV plan was equal or below to the 6 MV DEVH. Hence, regarding patient protection, the 3DCRT 15 MV treatment was superior compared to the 6 MV treatment. The head leakage and neutron DEVHs can be seen in Fig. 6.

Head leakage was almost constant in the phantom, whereas neutron dose was evaluated towards the surface. For all modalities, the 100 % volume level of the DEVHs was located at a higher dose for 6 MV compared to 15 MV. This was caused by a smaller leakage dose for 15 MV compared to 6 MV (Fig. 8) and the relatively low neutron dose in the center of the body (Fig. 1). The lower head leakage dose for 15 MV compared to 6 MV relativized the additional neutron dose equivalent contribution of the 15 MV treatments. Head leakage is assumed to be reduced because of more forward directed photons in the X-ray producing target for 15 MV compared to 6 MV.

Kry et al. [41] suggested, that the effective dose equivalent has to show a difference of at least 50 % such that the difference in risk is significant. Between 15 MV and 6 MV, the dose equivalent was clearly below a difference of 50 % for the same treatment modality. However independent of the nominal X-ray energy, the dose equivalent in the low and intermediated dose region was increased by up to a factor of two for the VMAT compared to the 3DCRT treatment and by up to a factor of four for the IMRT compared to the 3DCRT treatments. Although close to the treated volume the dose distribution is beneficial for IMRT compared to 3DCRT treatment, this should be weighted against an increased dose equivalent in over 90 % of the patient's body for IMRT compared to 3DCRT treatments. Furthermore using VMAT, similar dose distributions in the treated volume can be achieved compared to IMRT [42]. However, the out-of-field dose is different between the two modalities favoring VMAT for patient protection since a shorter beam-on time is needed compared to IMRT.

Varian linear accelerators have been shown to produce the most photoneutrons compared to other vendors [1]. This has raised

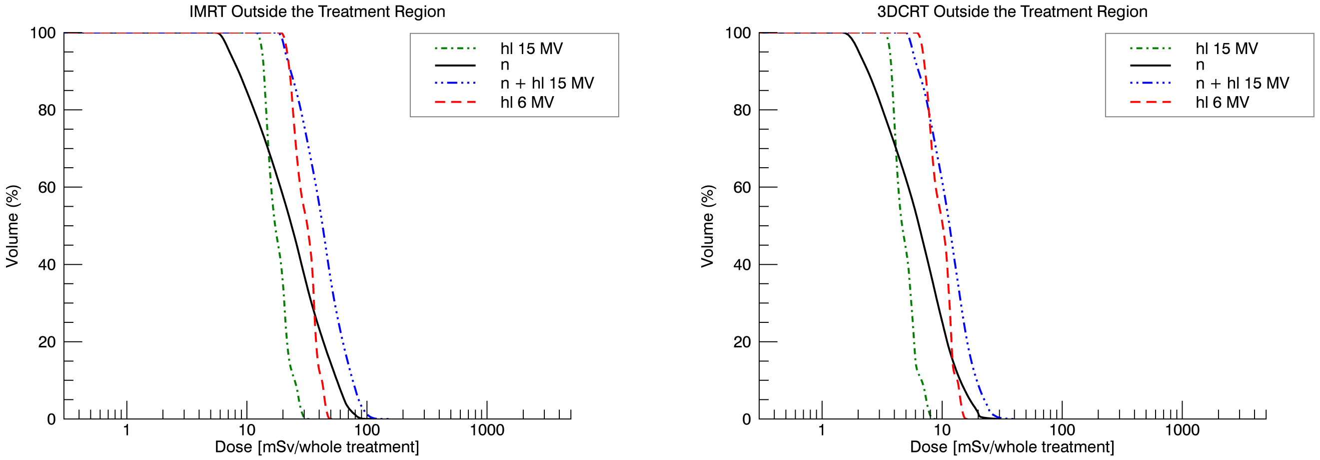

(a)

(b)

FIG. 6. Head leakage (hl) and neutron (n) DEVH for (a) the IMRT and (b) the 3DCRT treatments.

concerns about patient safety when treating someone with Varian linear accelerators operated at nominal X-ray energies higher than 10 MV [6, 43]. Far from the treatment region (> 50 cm), the photoneutron dose equivalent was similar compared to head leakage. Varian accelerators (600C, 21-iX) show a reduced leakage dose compared to other vendors (Elekta Synergy-II, Siemens Primus) [44]. Neutron dose and head leakage scale with the applied MUs such that an increase of neutron dose equivalent is balanced by the same decrease in head leakage (see Fig. 6). Hence, regarding patient protection for high energy treatments, the choice of the machine should not be based on neutron production but rather on the total dose equivalent.

Multiple studies reported an increased cancer risk based on an increased dose equivalent for high energy compared to low energy radiotherapy [43, 45]. The increased dose equivalent for high compared to low energy X-ray therapy were reported to be from the additional neutron dose. However, the neutron energies in these manuscripts were overestimated resulting in an overestimation of neutron dose. An extensive discussion of the overestimation in neutron dose reported by the literature can be found in [6]. For the same modality, we did not notice an increase in the whole-body dose equivalent for increasing nominal X-ray energy. For IMRT treatments, the findings are in agreement with a MC study made by Kry et al. [6].

A short coming of this study was that the investigation was located only to one treatment location (rhabdomyosarcoma in the prostate). However, the models presented in this manuscript are applicable for other treatment locations and patient geometries (except the whole-body CBCT dose calculation). The whole-body photon dose calculated using the stray dose model [17] was in good agreement with measurements of 6 MV treatments for Hodgkin disease (involved field and involved node) and for a treatments of an ependymoma in the head (3DCRT, IMRT, and VMAT) (unpublished data). Regarding out-of-field dose, further investigations are planned for different treatment indications. The investigation of other treatment locations compared to prostate are urgently needed [4].

To access the CBCT dose a whole-body measurement was generalized. It is time consuming and not practical to measure each time the dose of the used CBCT protocol. Furthermore, the choice of the protocol influences the dose distribution in the field-of-view region [33]. Analytical models to calculate the CBCT dose are available but they lack the ability to calculate the dose outside the field-of-view [46]. However, the CBCT dose outside the field-of-view is a minor contribution to the whole-body dose [15].

We did not include the out-of-field dose caused by electron contamination. Outside the primary beam, the dose close to the surface can be increased by a factor of 4 compared to deeper location (> 2 cm) [9]. However, most critical organs are located in a patient depth outside the reach of these electrons. Furthermore, usually treatments are applied using multiple gantry angles which reduces the increased surface dose caused by electron contamination compared to the dose in deeper locations [see Figs. 9(b)-(d)]. Nevertheless, the skin dose was underestimated.

For the calculation of the total whole-body dose of a real patient, the planning CT can be fused with a phantom containing the contours of critical tissues [47]. However, such a feature is not jet clinically available.

The reported neutron dose evaluated for a TrueBeam operated at 15 MV nominal X-ray energy can simply be scaled with a factor of 2.5 to access the neutron dose of the same treatments delivered with a Clinac iX operated at 18 MV nominal X-ray energy (see Appendix VI B). However, the scaling of the photon scatter dose for 15 MV compared to 18 MV is not straight-forward. For the Clinac iX operated at 18 MV, a 1.6 increased head leakage contribution was measured compared to the TrueBeam operated at 15 MV (see Appendix VI B). However, for 6 MV nominal X-ray energy an increased head leakage dose was reported for the Clinac iX compared to the TrueBeam caused by shielding differences of the two machines [17]. Hence, even for the same beam energy a higher dose equivalent is expected for the Clinac iX compared to the TrueBeam.

V. CONCLUSION

The calculated whole-body dose equivalent for IGRT treatments helped to understand the importance of the scatter contributions in different areas of the patient body. The calculations agreed well with the independent measurements and with reported values from the literature. For volumes receiving a doses lower than 20 % of the prescribed dose, 3DCRT is the choice of treatment regarding patient protection. For intensity-modulated treatments, VMAT should be used instead of IMRT because of a shorter beam on time for VMAT compared to IMRT which reduces the out-of-field dose.

By combining an improved model to calculate the scatter dose with the mean photon energies of the scatter contributions, it was possible to calculate the mean photon energy in the patient. The calculated energies agreed with measurements and reported values from the literature. The mean photon energy can be used for a more advanced calculation of the second tumor induction including RBE.

We introduced a simple neutron dose model which is easy to use and compared it with neutron dose measurements. The neutron dose calculated by the model overestimated the neutron dose equivalent by around 20 % compare to the measurements. However, this is the first analytical neutron model to calculate the dose equivalent resulting from photoneutrons produced by high energy external beam therapy. The relative small error in photon dose calculations compared to the relative large error in neutron dose equivalent reduced the overall error to around ±20 % (type B) since the photon dose was the main contribution to the out-of-field dose.

With the presented accuracy in whole-body dose calculation from IGRT treatments, the limiting factor for cancer risk assessment is the uncertainty in the risk calculation. Further research should be done to improve cancer risk models to achieve better estimates.

VI. APPENDIX

A. 15 MV photon scatter model

A general model for photon stray dose calculation developed for a nominal X-ray energy of 6 MV [17] was improved and adjusted for 15 MV. The total absorbed dose outside the treatment field (D_t) can be described as the sum of three contributions,

$$D_t = D_{ps} + D_{cs} + D_{hl}. \tag{4}$$

Patient scatter (D_{ps}) is the dose mainly produced by Compton scatter photons of the treatment field penetrating the patient. Photons of the primary field scattered at the jaws and MLCs is described by collimator scatter (D_{cs}). Head leakage is the out-of-field dose contribution from photons which originate from the X-ray producing target and leaking through the gantry head shielding (D_{hl}).

The four parameters of the mechanistic model of patient scatter (see Eq. 8 from [17]) were adjusted for 15 MV nominal X-ray energy. The total absorbed dose was measured with a Rigid Stem ionization chamber 30016 (PTW, Freiburg, Germany) in simple geometries. Patient scatter was extracted from the total out-of-field measurement and the four physically motivated fit parameters were determined.

In Table III, the evaluated parameters for 15 MV nominal X-ray energy can be seen. For comparison, the parameters for 6 MV determined in [17] are shown, too. The field width (C_W) and attenuation coefficient [$\mu(E^{\gamma}_{ps})$] showed almost no difference between the two nominal X-ray energies. However, the backscatter contribution (C_B) showed a clear decrease for 15 MV compared to 6 MV. Furthermore, the normalization constant (C_N) describing the magnitude of patient scatter decreased by a factor of 1.8 for 15 MV compared to 6 MV.

TABLE III. The four measured parameters for the patient scatter model (Eq. 8 from [17]) and the attenuation of the primary beam (pb) from the literature [48].

Beam	C_W	C_N	C_B	$\mu(E^{\gamma}_{ps})$	$\mu(E^{\gamma}_{pb,10\times10\,\mathrm{cm}^2})$
6 MV	0.845	0.724 mGy/Gy	0.203	0.007 22 mm^{-1}	0.005 41 mm^{-1}
15 MV	0.857	0.400 mGy/Gy	0.174	0.007 68 mm^{-1}	0.004 10 mm^{-1}

In Fig. 7, we see the comparison between patient scatter resulting from 15 MV and 6 MV nominal X-ray energy. The normalized patient scatter as a function of field widths and lengths showed no difference between 15 MV and 6 MV [Fig. 7(a)]. The absolute patient scatter dose 15 cm from the field edge along a line parallel to the CAX (R-dependence) showed an increased dose for 6 MV compared to 15 MV [Fig. 7(b)].

Chofor et al. [37] simulated an almost twofold increase in patient scatter for 6 MV compared to 15 MV nominal X-ray energy.

Ruben et al. [7] measured an increase in patient scatter of 1/3. However, the difference in patient scatter between two nominal X-ray energies is dependent of the location in the patient, as can be seen in Fig. 7(b). Patient scatter is independent of the beam head design and is an unavoidable result of external radiation therapy [37]. The differences in patient scatter of a 6 MV compared to a 15 MV showed that primarily the normalization constant of the patient scatter model has to be adjusted when using different beam energies. The normalization constant can be determined from one measurement set-up. However, for flattening filter free beams, all parameters could be different compared to beams produced with flattening filter.

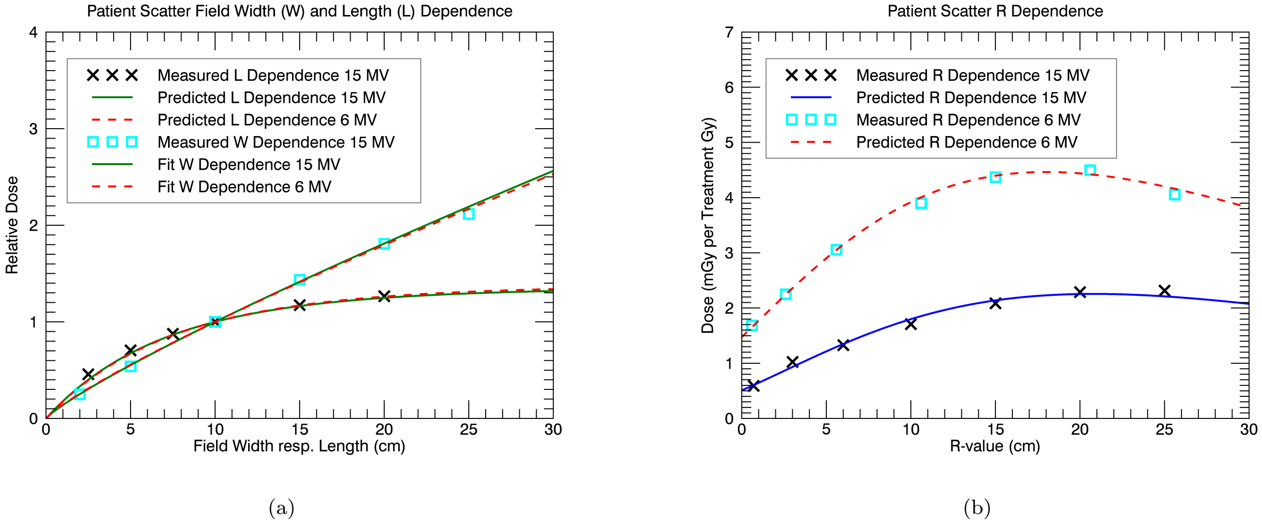

FIG. 7. In (a) the measured and model predicted field length dependence of patient scatter. Furthermore, the fit of the field width dependence. In (b) the measured and model-predicted dose along a line parallel to the CAX 15 cm from the field edge (R-dependence).

The empirical models of collimator scatter and head leakage from [17] were improved for the current work. For 6 MV and 15 MV nominal X-ray energy, collimator scatter and head leakage were measured along the MPAX in a $30 \times 30 \times 30\,\mathrm{cm}^2$ RW3 phantom (SSD = 100 cm) using a Rigid Stem ionization chamber. All measurements of collimator scatter and head leakage are discussed for location in the direction 'isocenter towards gun' and collimator rotation of 0 °. Especially the head leakage contribution can change for other locations in the gantry room [17].

For each energy, the measurements were made at different depths in the RW3 phantom (7 cm, 15 cm, 23 cm) with and without a lateral displacement of 8 cm from the MPAX. This resulted in nine dose curves parallel to the MPAX, assuming lateral symmetry for collimator scatter and head leakage. Furthermore, collimator scatter measurements were made for different symmetric field sizes defined by the MLCs. For head leakage, the measurements were conducted for jaws and MLCs closed. We noticed a change in collimator scatter for fields with changing MLC width openings compared to the jaw opening. To account for this effect, collimator scatter for different MLC width openings (jaws constant at $10 \times 10\,\mathrm{cm}^2$) was measured for different distances along the MPAX. With the results, a scaling matrix along the MPAX was calculated which corrected for the change of collimator scatter with changing MLC width openings. No such effect was noticed for a variation in the MLC length opening [17].

Depth dose curves of the two scatter contributions were measured in simple geometries at different distances along the MPAX to evaluate the exponential decrease in depth. The collimator scatter and head leakage dose in the Alderson phantom of a real treatment were calculated by an interpolation between the measured point doses. The point doses were scaled with the exponential decrease in depth to calculate the dose for different locations in the patient. To calculate the depth, the patient was assumed to be water-equivalent with the exception of the lungs. For the lungs, a mass density of $0.25 \times \rho_{\mathrm{water}}$ was assumed.

In Fig. 8, we see the collimator scatter and head leakage per 100 MUs along the MPAX in the center of the RW3 phantom. Collimator scatter is shown for a jaw field size of $10 \times 10\,\mathrm{cm}^2$ with a MLC field size of $9 \times 10\,\mathrm{cm}^2$ representing a 3DCRT field and MLC field size of $3 \times 10\,\mathrm{cm}^2$ representing an IMRT field. The field sizes were similar to the field sizes of the 3DCRT and IMRT treatments measured in this work. Hence, for calculation of the dose, the IMRT treatment with dynamic MLCs were approximated by static fields. For the 3DCRT fields, the ratio of collimator scatter between 15 MV and 6 MV decreased from 1.5 to 0.88 for increasing distance to the isocenter. This is in agreement with other publications, reporting increased collimator scatter close to the field edge with increasing energy [1].

Close to the field edge, collimator scatter of the 15 MV IMRT field was decreased by a factor of 0.7 compared to the 15 MV 3DCRT field. We believe, that this was caused by the shielding effect of the MLCs for photons of the primary beam scattered in the gantry head. The ratio of collimator scatter between the IMRT and the 3DCRT field increased to 1.3 (25 cm from isocenter) with increasing distance to the field edge. Hence, the additional photon scatter from the MLCs outweighed the shielding effect of the MLCs. For distances of 40 cm to the isocenter and greater, there was no difference in collimator scatter

for the 3DCRT and IMRT field.
Along the MPAX, head leakage of 6 MV was around 1.6 times higher compared to head leakage of 15 MV. For both nominal X-ray energies, head leakage showed the same increase for increasing distance to the isocenter. The increase can be explained by shielding effects of the gantry head.

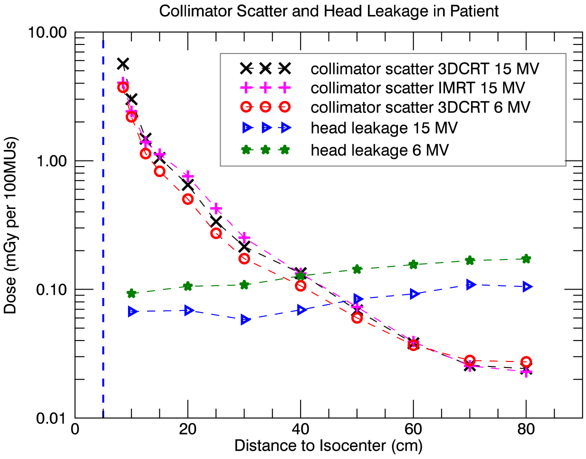

FIG. 8. Collimator scatter and head leakage for two nominal X-ray energies along the MPAX for a constant patient thickness of 10 cm. For 15 MV, collimator scatter is shown for a static IMRT and a 3DCRT field.

In Table IV, wee see the measured attenuation coefficient for collimator scatter and head leakage of the two nominal X-ray energies. In contrast to the expectation, the attenuation of the scatter contribution was higher for 15 MV compared to 6 MV nominal X-ray energy. The attenuation for collimator scatter was calculated using a straight line connecting the rear jaw and the point of interest in the patient. For head leakage, the attenuation was calculated using a straight line connecting the X-ray producing target with the point of interest located in the patient.

TABLE IV. The attenuation coefficients in water for collimator scatter and head leakage.

Beam	$\mu(E^{\gamma}_{cs})_m$	$\mu(E^{\gamma}_{hl})_m$
6 MV	$0.001\,96\,\mathrm{mm}^{-1}$	$0.002\,70\,\mathrm{mm}^{-1}$
15 MV	$0.003\,05\,\mathrm{mm}^{-1}$	$0.003\,31\,\mathrm{mm}^{-1}$

In Figs. 9(a)-(d), the measured versus the predicted out-of-field photon dose can be seen. For the 15 MV treatments, the predicted dose was in good agreement with the measured dose [Fig. 9(a)]. In Figs. 9(b)-(d), the out-of-field dose contributions along the MPAX are plotted. The total predicted dose was in good agreement with the measurements. Close to the treated volume, patient scatter was dominating. Depending on the modality, patient scatter or collimator scatter was the largest source of dose up to 50 cm from the isocenter. Further away, head leakage was the main contribution of the out-of-field dose. Additional to the dose along the MPAX, the measured skin dose is plotted. The higher skin dose was caused by an additional dose from the electron contamination in the out-of-field region [9]. The largest increase in skin dose compared to the MPAX dose was noticed for the VMAT treatment. The VMAT treatment had the longest beam on time for the gantry angles directly above the detectors. Hence, a different shielding of the detectors from the electron contamination and the various beam-on times explained the differences in the measured skin dose between the modalities.

B. Neutron spectrum specific correction

Primarily, the thermal part of the neutron spectrum was detected by TLD600 [27, 49]. With a spectra-dependent correction factor (including fast neutrons), the extracted thermal neutron signal from the (n, α)-reactions of a TLD600 was converted to neutron dose equivalent. For photoneutrons produced during radiotherapy, a drastic change of the neutron spectrum is expected as a function of depth in the patient [16]. Hence, a depth-dependent conversion factor was determined to convert the neutron signal to neutron dose equivalent. A combination of TL600 and TLD700H was used to determine the neutron dose. TLD700H are around 20 times more sensitive to photons compared to TLD600/700 [27] and show a 250 times reduced thermal neutron sensitivity compared to TLD600 [49]. A smaller correction of the TLD600 signal for the photon contamination reduces the error in the neutron signal.

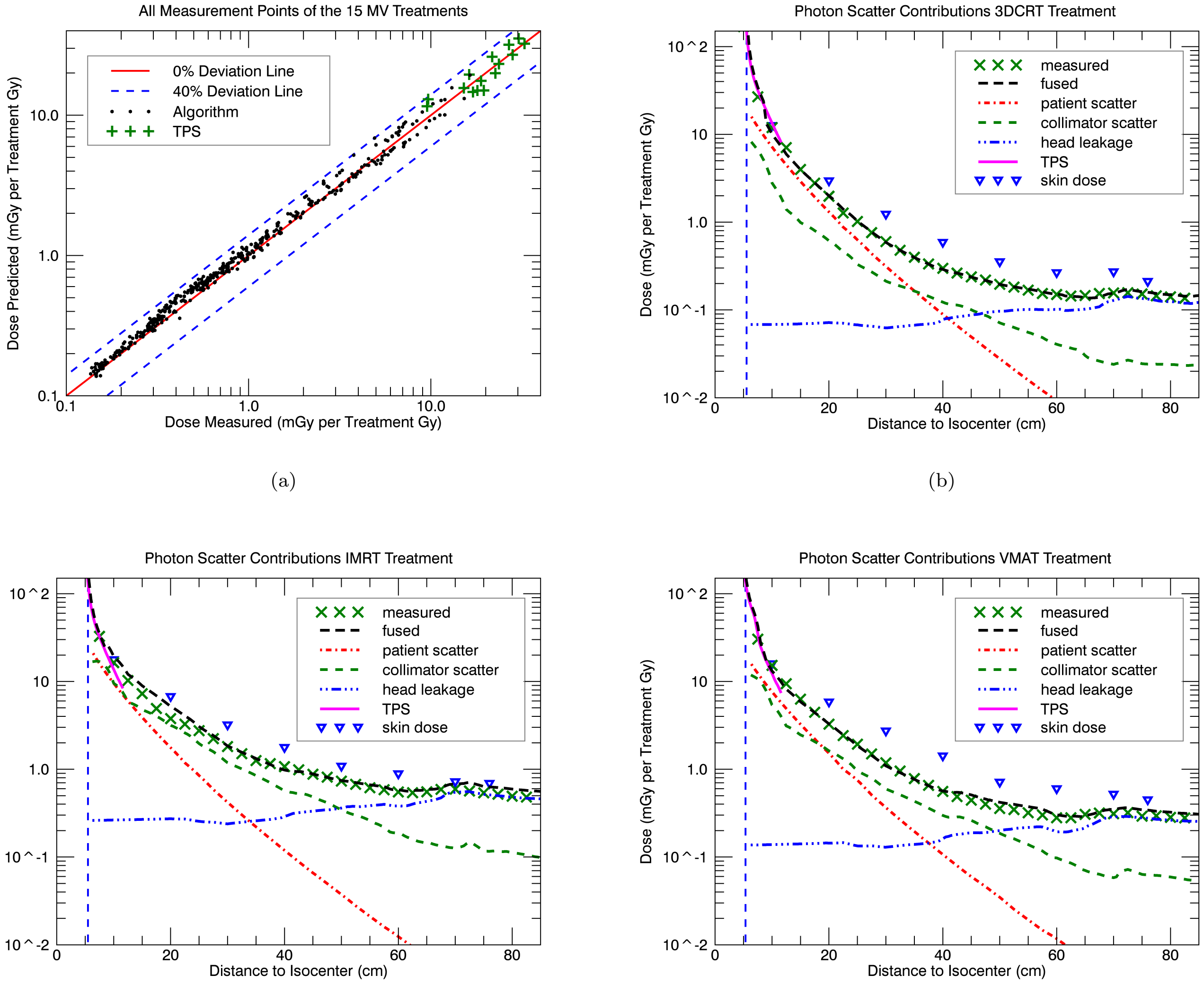

(a)

(b)

(c)

(d)

FIG. 9. (a) The 438 out-of-field TLD700H photon dose point measurements in the Alderson phantom (head first supine) compared to the algorithm-predicted doses for the three 15 MV treatments. Furthermore, the TPS-calculated out-of-field dose compared to the TLD measured dose is shown for the transversal phantom slice 3 cm from the treatment volume. The stray dose contributions, the total predicted doses fused with the TPS dose, and the measured doses along the MPAX for (b) the 3DCRT, (c) the IMRT, and (d) the VMAT treatment applied with a TrueBeam are shown. The vertical dashed lines in (b)-(d) represents the field edge calculated by the out-of-field dose algorithm. Additionally, the measured skin dose along a line from the bellybutton to the nose of the Alderson phantom is plotted.

1. *TLD600 reference calibration*

For calibration, the TLD600 were placed on the surface of an ISO water phantom [50–52] and irradiated separately with neutrons from a ^{241}AmBe and a ^{252}Cf source. The personal neutron dose equivalent $\{H_p^n(10)\ [\mathrm{mSv}]\}$ can be calculated using the normalized neutron spectrum in air $[\phi_{air}^n(E^n)]$ and the fluence to personal dose equivalent conversion coefficients $\{h_p^n(10, E^n)\ [\mathrm{mSv} \cdot \mathrm{cm}^2]\}$ from IAEA TR403 [53]

$$H_p^n(10) = \sum_{E^n} [N \cdot \phi_{air}^n(E^n)] \cdot h_p^n(10, E^n), \tag{5}$$

where $N\ [\mathrm{cm}^{-2}]$ is the total numbers of neutrons per cm^2.

The neutron response per volume of TLD600 placed at the surface of the ISO water phantom was determined by Veinot and Hertel [54]. They simulated mono-energetic neutrons in air imping on the ISO water phantom to determine the response factors $\{r_{\mathrm{ISO}}^n(E^n)\ [\mathrm{cm}^2 \cdot (n,\alpha)\text{-reactions} \cdot n^{-1}/\mathrm{cm}^3]\}$. Hence, the response factors accounted for the neutrons scattered by the

ISO water phantom. The simulated response curve with neutron energy was qualitatively in agreement with the response curve from IAEA TR403 [53]. The neutron signal detected by a TLD600 at the surface of the ISO water phantom (R^n_{surface}) can be expressed by

$$R^n_{\text{surface}} = C \cdot N \sum_{E^n} \phi^n_{air}(E^n) \cdot r^n_{\text{ISO}}(E^n). \tag{6}$$

with C is a constant of proportionality, linking the TLD600 signal to the (n,α)-reactions per TLD600 volume. C was determined using Eq. 6 and by solving Eq. 5 for N

$$C = \frac{R^n_{m,\text{surface}}}{N \sum_{E^n} \phi^n_{air}(E^n) \cdot r^n_{\text{ISO}}(E^n)} = \frac{R^n_{\text{surface}}}{H^n_p(10)} \cdot \frac{\sum_{E^n} \phi^n_{air}(E^n) \cdot h^n_p(10, E^n)}{\sum_{E^n} \phi^n_{air}(E^n) \cdot r^n_{\text{ISO}}(E^n)}. \tag{7}$$

The reference spectra in air of ^{241}AmBe and ^{252}Cf were taken from the IAEA TR403 compendium [53].
The neutron signal at the surface was measured by irradiating eight TLD600 with neutrons, once using a ^{241}AmBe and once using a ^{252}Cf source. $H^n_p(10)$ was provided by PSI Calibration Laboratory. At the Calibration Laboratory, $H^n_p(10)$ was determined by using a neutron dose rate meter calibrated at the Physikalisch-Technische Bundesanstalt (PTB, Braunschweig, Germany) which is used in the laboratory as secondary standard. The measurement of the neutron fluence at the center of the front surface of the ISO water phantom was converted into $H^n_p(10)$ by using conversion coefficients for the neutron spectrum of the ^{241}AmBe and ^{252}Cf source specified by ISO [52]. The conversion coefficients included the scatter contribution of the phantom.
The generic reader output of each TLD600 ($S^{\gamma+n}_{600}$ [counts]) was converted to a fictive photon dose signal ($R^{\gamma+n}_{600}$ [mGy$_\text{S}$]) using TLD-specific photon dose calibration factors. The measured neutron signal was simply the difference between $R^{\gamma+n}_{600}$ and the photon dose signal (R^γ_{600}) of a TLD600. The conversion of the generic reader output for TLD600 to a fictive photon dose signal had mainly two reasons. (1) A generally applicable C for all TLD600 was determined, since it was not possible to measure an individual C for all 200 TLD600 used in this work. It was discovered that for all TLD600, the ratio of photon/neutron signal was constant for a specific irradiation. However, the generic readout output in counts for the eight calibration TLD600 showed a large variation. This variation was accounted for by converting the generic readout counts to a fictive photon dose signal using TLD-specific photon dose calibration factors. (2) The neutron calibration determined in this work can be generally used by workers, if they are converting the generic readout counts of their TLD600 to a fictive photon dose signal. In general, it is simpler to calibrate TLD600 using photons compared to neutrons.
Eight (TLD600,TLD700H)-pairs per irradiation (^{241}AmBe and ^{252}Cf) were loaded in empty pill casings made of PMMA. The pill casings were fixed on the surface of the ISO water phantom. The TLDs had different orientations towards the neutron source. The front surface of two TLD chip pairs (0 °) and the edge of two other TLD pairs (90 °) were facing the source. The remaining four pairs were positioned at an angle of 70 ° relative to the surface of the water phantom. Furthermore, five (TLD700,TLD700H)-pairs per irradiation were fixed on the surface of the ISO water phantom to measure the photon dose and the mean photon energy ($\overline{E}^\gamma_m$) for the ^{241}AmBe and the ^{252}Cf calibration. The measurement of the photon dose and mean photon energy by a combination of TLD700 and TLD700H is described in [22]. The measured mean energy together with the method described in [22] was used to determine the correction factor for the response with photon radiation energy [$\overline{G}_{\text{TLD}}(\overline{E}^\gamma_m)$ $(k = 5)$] of TLD700H and TLD600, respectively. At 50 cm source-surface distance, 28.4 mSv and 36.4 mSv personal neutron dose equivalent were irradiated by ^{241}AmBe and ^{252}Cf, respectively. The neutron signal at the surface of TLD600 for each (TLD600,TLD700H)-pair was determined by

$$R^n_m = R^{\gamma+n}_{600} - R^\gamma_{600} = S^{\gamma+n}_{600} \cdot L^\gamma_{600,cal} - S^\gamma_{700\text{H}} \cdot L^\gamma_{700\text{H},cal} \cdot \frac{\overline{G}_{700\text{H}}(\overline{E}^\gamma_m)}{\overline{G}_{600}(\overline{E}^\gamma_m)}. \tag{8}$$

$L^\gamma_{600,cal}$ [mGy/count] and $L^\gamma_{700\text{H},cal}$ are the TLD-specific photon dose calibration factors for TLD600 and TLD700H, respectively. $S^\gamma_{700\text{H}}$ [counts] is the photon dose signal detected by TLD700H.
With the mean of the TLD600 neutron signals $(k = 8)$ per irradiation, C was calculated (Eq. 7). A mean $\overline{C}$ $(k = 16)$ was determined from the ^{241}AmBe and the ^{252}Cf irradiation.

2. *Neutron dose equivalent conversion*

$\overline{C}$ [mGy$_\text{S}\cdot$cm$^3/(n,\alpha)$-reaction] from Eq. 7 measured at PSI standard laboratory was used to calculate the signal to neutron dose equivalent conversion factors for photoneutrons produced by linear accelerators. The out-of-field neutron spectra in tissue as function of depth were provided by Kry et al. [16]. They simulated the neutron spectra at a distance of 25 cm to the CAX in a $30 \times 30 \times 60$ cm^3 phantom for a Varian 2100 Clinac iX (Varian Medical Systems, Palo Alto, CA), operated at nominal X-ray energy of 18 MV. Using the normalized photoneutron spectra in depth [$\phi^n_{linac}(d, E^n)$] and $\overline{C}$, the response of a TLD600 in a certain depth d [$R^n(d)$] can be expressed by

$$R^n(d) = \overline{C} \cdot N_{linac}(d) \sum_{E^n} \phi^n_{linac}(d, E^n) \cdot r^n(E^n), \tag{9}$$

where $N_{linac}(d)$ [cm^{-2}] is the total number of neutrons per cm^2 in the depth d. The response factors per TLD600 volume $\{r^n(E^n)$ [cm$^2 \cdot (n, \alpha)$-reactions $\cdot\, n^{-1}$/cm^3]$\}$ were calculated by

$$r^n(E^n) = \sigma(E^n) \cdot \rho_{^6\mathrm{Li}}, \tag{10}$$

where $\sigma(E^n)$ [cm$^2 \cdot (n, \alpha)$-reactions $\cdot\, n^{-1}$] is the (n, α)-reaction cross section of ^{6}Li [55] and $\rho_{^6\mathrm{Li}}$ [cm^{-3}] the number of ^{6}Li atoms per TLD600 volume.
The desired quantity for the patient was the neutron dose equivalent. The measured neutron dose equivalent at a certain depth in the phantom [$H^n_m(d)$] could be determined by

$$H^n_m(d) = N_{linac}(d) \sum_{E^n} \phi^n_{linac}(d, E^n) \cdot h^n(E^n) = \overline{C}^{-1} \cdot \frac{\sum_{E^n} \phi^n_{linac}(d, E^n) \cdot h^n(E^n)}{\sum_{E^n} \phi^n_{linac}(d, E^n) \cdot r^n(E^n)} \cdot R^n_m =: K^n(d) \cdot R^n_m, \tag{11}$$

where $N_{linac}(d)$ was substituted from Eq. 9. Hence, the absolute number of neutrons $N_{linac}(d)$ was indirectly measured by the neutron signal of the TLD600 (R^n_m). The flunece to dose equivalent conversion coefficients $\{h^n(E^n)$ [mSv $\cdot$ cm^2]$\}$ were determined by Sibert and Schumacher [56]. They multiplied simulated neutron kerma factors as a function of energy [57] with the corresponding neutron quality factors. $\phi^n_{linac}(d, E^n)$ corresponds to the normalized neutron spectrum in the depth where the neutron signal was measured. $K^n(d)$ [mSv/mGy$_\mathrm{S}$] represents the final neutron signal to dose equivalent conversion coefficient as a function of depth.

3. *Verification calculations and measurements*

Kry et al. [16] simulated the out-of-field photoneutron spectra for a Varian 2100 Clinac operated at nominal X-ray energy of 18 MV. According to Kry et al. [1], the shape of the photoneutron spectra are similar between a 18 MV and a 15 MV irradiation but the photoneutron production is reduced for 15 MV compared to 18 MV. Furthermore, the out-of-field neutron spectra are similar between open and closed fields (MLC and jaws closed) irradiations [1, 11]. Howell et al. [11] measured the neutron spectra in air at a distance of 40 cm to the CAX (SSD = 100 cm) for closed fields of modern linear accelerators. Using these neutron spectra in air, we calculated the personal neutron dose equivalent conversion factor for each spectrum to evaluate the difference between the measured and simulated neutron spectra. Using the normalized measured neutron spectra from [11] [$\phi^n_{linac,air,m}(E^n)$], the personal neutron dose equivalent could be determined by following Eq. 5 with N substituted by Eq. 6,

$$H^n_p(10) = \overline{C}^{-1} \cdot \frac{\sum_{E^n} \phi^n_{linac,air,m}(E^n) \cdot h^n_p(10, E^n)}{\sum_{E^n} \phi^n_{linac,air,m}(E^n) \cdot r^n_{\mathrm{ISO}}(E^n)} \cdot R^n_{m,\mathrm{surface}} =: K^n_p(10, \phi^n_{linac,air,m}) \cdot R^n_{m,\mathrm{surface}}. \tag{12}$$

$K^n_p(10, \phi^n_{linac,air,m})$ [mSv/mGy$_\mathrm{S}$] represents the personal neutron dose equivalent conversion coefficient linking the neutron signal measured at the surface of an ISO water phantom ($R^n_{m,\mathrm{surface}}$) to personal dose equivalent.
Using the simulated neutron spectrum at 10 mm depth in water, the personal dose equivalent could be estimated by

$$H^n_p(10) \approx H^n(10) = K^n(10) \cdot \frac{R^n_c(10\,\mathrm{mm})}{R^n_c(-1\,\mathrm{mm})} \cdot R^n_{m,\mathrm{surface}} =: K^n_p(10, \phi^n_{linac,water,s}) \cdot R^n_{m,\mathrm{surface}}, \tag{13}$$

where $K^n(10)$ is from Eq. 11 and the calculated neutron response of TLD600 [$R^n_c(d)$] is from Eq. 9. $H^n(10)$ was an estimate of $H^n_p(10)$ since Kry et al. simulated the neutron spectra in a phantom which had a different geometry compared to the ISO water-equivalent phantom. To evaluate the difference between measured and simulated neutron spectra, $K^n_p(10, \phi^n_{linac,air,m})$ calculated from the measured spectra of various nominal beam energies and different treatment machines were compared to $K^n_p(10, \phi^n_{linac,water,s})$ which was determined with the MC simulated energy spectrum.
To investigate a change in neutron spectra for different off-axis distances, TLD600 measurements were conducted for different distances to the CAX. Kry et al. [16] simulated the neutron spectra at 25 cm from the CAX in direction towards gun. We measured the neutron response of TLD600 at three distances from the CAX towards gun (15 cm, 25 cm, and 60 cm) for different depths d and compared the results with the theoretical TLD600 response calculated using Eq. 9. For the measurements,

the photoneutrons were produced by a TrueBeam operated at 15 MV with MLCs and jaws closed. A closed field enabled a bigger neutron:photon signal ratio compared to an open field [39].
Lastly, the absolute value of neutron dose equivalent determined with the MC simulated spectra and measured using TLD600 were compared. The absolute neutron spectra for a closed field irradiation in water at 25 cm from the CAX simulated by Kry et al. [16] was converted to neutron dose equivalent using Eq. 11. This represented the neutron dose equivalent for closed jaws and MLCs of a Varian 2100 Clinac operated at nominal X-ray energy of 18 MV. We measured the neutron dose equivalent for a closed field in 0.1 cm depth of a $30 \times 30 \times 30\,\mathrm{cm}^3$ water-equivalent slab phantom (RW3) for a Varian Clinac operated at 18 MV and a TrueBeam operated at 15 MV.

4. Results and discussion: neutron spectrum specific correction

In Table V, the results of the ^{241}AmBe and the ^{252}Cf irradiations can be seen. The deviation was 8 % between the means of the calculated C values from the ^{241}AmBe and the ^{252}Cf irradiations. Although the two neutron sources showed a difference in the fluence-average energy of a factor of two, the determined C values of both irradiations were in good agreement.
From the two irradiations, an average $\overline{C}$ was determined as $2.39 \cdot 10^{-8}\,\frac{\mathrm{mGy_S \cdot cm^3}}{(\mathrm{n},\alpha)\text{-reaction}} \pm 9\,\%$ (type B). The uncertainty was calculated from the variation of the TLD600 signals (including uncertainty in the readout, angle of irradiation, and photon dose correction using Eq. 8) and the uncertainty in $H_p^n(10)$ provided by PSI. It is important to note that the neutron calibration of TLD600 was not in $H_p^n(10)$. $H_p^n(10)$ was used to determine the absolute number of (n, α)-reactions per TLD600 to evaluate $\overline{C}$.
The measured uncertainty of the neutron signal divided by the total signal was below 1 % (type A) (see Table V). Hence, every TLD600 showed the same neutron sensitivity relative to its individual photon sensitivity. Therefore, it was justified to use one general $\overline{C}$ for all 200 TLD600 to measure the neutron dose equivalent of photoneutrons produced by linear accelerators. The measured photon dose contribution from ^{241}AmBe and ^{252}Cf was in agreement with the values reported by PSI [58].

TABLE V. The result from the neutron calibration of TLD600 using ^{241}AmBe and ^{252}Cf with a source to TLD distance of 50 cm. The neutron signal at the surface of TLD600 ($R^n_{m,\mathrm{surface}}$) was determined using Eq. 8, the total signal ($S_{600}^{\gamma+n}$) and the photon signal (S_{600}^{γ}) of a TLD600. Furthermore, the mean photon energies ($\overline{E}_m^{\gamma}$) of the two sources determined with a combination of TLD700 and TLD700H are shown. All uncertainties are given by the type B σ except the measured uncertainty (type A) of the signal ratio.

Source	$\frac{H_p^n(10)}{\overline{R}^n_{m,\mathrm{surface}}}$	$\overline{C}\ [\frac{\mathrm{mGy_S \cdot cm^3}}{(\mathrm{n},\alpha)\text{-reaction}}]$	$\overline{E}_m^{\gamma}$ [MeV]	$\frac{S_{600}^{n}}{S_{600}^{\gamma+n}}$
^{241}AmBe	$2.52\,\frac{\mathrm{mSv}}{\mathrm{mGy_S}} \pm 7\,\%$	2.30×10^{-8}	0.25 ± 0.01	$(84.6 \pm 0.8)\,\%$
^{252}Cf	$1.59\,\frac{\mathrm{mSv}}{\mathrm{mGy_S}} \pm 6\,\%$	2.48×10^{-8}	0.58 ± 0.04	$(92.5 \pm 0.2)\,\%$

The values of the neutron signal to neutron dose equivalent conversion coefficient and the neutron percent depth dose equivalent can be seen in Table VI. The simulated neutron dose equivalent decreased rapidly with increasing penetration depth. In the first 5 cm of tissue, the energy of the fast neutrons was quickly degraded and the thermal neutrons accumulated [16]. This explained the rapid increase of the TLD600 signal in the first 4 cm penetration in tissue. At depths greater than 7-8 cm, equilibrium between the absorption of thermal neutrons and the thermalization of the remaining fast neutrons was achieved. Hence, the shape of the neutron energy spectrum remained nearly constant, but reduced in magnitude with increasing depth. This resulted in a decrease of the TLD600 signal by approximately 10 % per centimeter penetration in tissue for depths greater than 6 cm. Room-scattered neutrons caused the nearly constant TLD600 signal for depths in tissue of 20-30 cm.

The personal neutron dose equivalent conversion coefficients calculated using the measured neutron spectra from Howell et al. [11] (Eq. 12), can be seen in Table VII. Furthermore, the neutron dose equivalent conversion coefficient calculated with the simulated neutron spectra is shown (Eq. 13). In general, the conversion coefficient increased with increasing average neutron energy. Within the uncertainties, all conversion coefficients of the different treatment machines and various nominal X-ray energies showed no significant difference ($\alpha = 0.05$) compared to the conversion coefficient of the simulation. The simulation of the neutron spectra were made for a $10 \times 10\,\mathrm{cm}^2$ field of a Varian Clinac iX operated at 18 MV [16]. For the same machine and nominal X-ray energy, the conversion coefficient of the measured spectrum showed the smallest deviation to the conversion coefficient of the simulated spectra. Hence, it was justified to use the simulated neutron spectra to determine the neutron dose equivalent for a Varian TrueBeam operated at 15 MV.

In Table VIII, we see the deviation between the measured and calculated TLD600 response for different distances to the CAX, depths in the phantom and gantry angles. Over all measurements, the deviation was $(0 \pm 13)\,\%$ (type A). The deviation increased for increasing gradient in the TLD600 response (see Table VI). For a gantry angle of 180 °, the treatment table was located between the phantom and the neutron source (gantry head). The geometry of the table was not included for

TABLE VI. The determined correction factors [$K^n(d)$, Eq. 11] as a function of depth (d) in soft tissue and water. Furthermore, the simulated neutron percent depth dose equivalent [$H^n_{tissue,s}(d)$, Eq. 11] and TLD600 neutron response [$R^n_{tissue,s}(d)$, Eq. 9] as a function of depth in soft tissue. $H^n_{tissue,s}(d)$ and $R^n_{tissue,s}(d)$ were normalized to the maximum value. The spectra used for the calculations were simulated by Kry et al. [16]. d was calculated using a straight line connection the X-ray producing target with the point of interest located in a $30 \times 30 \times 60\,\mathrm{cm}^3$ phantom (SSD = 100 cm).

d [cm]	$K^n_{tissue}(d)$ [$\frac{\mathrm{mSv}}{\mathrm{mGy_S}}$]	$H^n_{tissue,s}(d)$ [%]	$R^n_{tissue,s}(d)$ [%]	$K^n_{water}(d)$ [$\frac{\mathrm{mSv}}{\mathrm{mGy_S}}$]
-0.1	-	-	27	-
0.1	$3.25 \cdot 10^{-1}$	100	33	$3.05 \cdot 10^{-1}$
0.36	$2.39 \cdot 10^{-1}$	97	43	$2.17 \cdot 10^{-1}$
1.0	$1.40 \cdot 10^{-1}$	83	63	$1.23 \cdot 10^{-1}$
2.1	$7.82 \cdot 10^{-2}$	62	85	$6.64 \cdot 10^{-2}$
3.1	$5.01 \cdot 10^{-2}$	45	97	$4.21 \cdot 10^{-2}$
4.1	$3.51 \cdot 10^{-2}$	33	100	$2.93 \cdot 10^{-2}$
5.1	$2.68 \cdot 10^{-2}$	24	97	$2.24 \cdot 10^{-2}$
6.2	$2.18 \cdot 10^{-2}$	18	90	$1.81 \cdot 10^{-2}$
7.2	$1.79 \cdot 10^{-2}$	14	82	$1.15 \cdot 10^{-2}$
8.2	$1.55 \cdot 10^{-2}$	10	72	$1.36 \cdot 10^{-2}$
9.2	$1.36 \cdot 10^{-2}$	8	62	$1.20 \cdot 10^{-2}$
10.3	$1.26 \cdot 10^{-2}$	6	52	$1.09 \cdot 10^{-2}$
15.4	$9.26 \cdot 10^{-3}$	2	20	$9.04 \cdot 10^{-3}$
20.4	$8.07 \cdot 10^{-3}$	1	10	$7.01 \cdot 10^{-3}$
25.5	$7.21 \cdot 10^{-3}$	1	10	$5.83 \cdot 10^{-3}$
30.5	$1.60 \cdot 10^{-2}$	2	12	$1.42 \cdot 10^{-2}$

TABLE VII. The personal neutron dose equivalent conversion coefficients calculated with the measured neutron spectra [$K^n_p(10, \phi^n_{linac,air,m})$, Eq. 12] for different linear accelerators and nominal X-ray energies. The neutron spectra were measured for a closed field [11]. Furthermore, the deviations (Dev) compared to the personal dose equivalent conversion coefficient determined with the MC simulated neutron spectra [$K^n_p(10, \phi^n_{linac,tissue,s}) = (3.09 \pm 0.06) \cdot 10^{-1}\,\frac{\mathrm{mSv}}{\mathrm{mGy_S}}$ (type B), Eq. 13]. The simulation was made for a $10 \times 10\,\mathrm{cm}^2$ field of a Varian Clinac iX operated at 18 MV [16]. The type B standard uncertainties were calculated from the reported error of the measured spectra and the estimated error for the digitalization of the spectra.

Linac	Nominal X-ray energy [MV]	Average neutron energy [11]	$K^n_p(10, \phi^n_{linac,air,m})$ [$\frac{\mathrm{mSv}}{\mathrm{mGy_S}}$]	Dev [%]
Varian 21EX	15	0.23	$(2.72 \pm 0.27) \cdot 10^{-1}$	-12
	18	0.24	$(2.80 \pm 0.28) \cdot 10^{-1}$	-9
	20	0.24	$(2.78 \pm 0.28) \cdot 10^{-1}$	-10
Elekta Precise	15	0.27	$(3.42 \pm 0.34) \cdot 10^{-1}$	11
	18	0.26	$(3.69 \pm 0.37) \cdot 10^{-1}$	19
Siemens ONCOR	15	0.20	$(2.68 \pm 0.27) \cdot 10^{-1}$	-13
	18	0.21	$(2.52 \pm 0.25) \cdot 10^{-1}$	-15

calculating the change in the neutron spectrum. This explained the biggest discrepancies between the measured and the calculated TLD600 neutron response. The neutron spectra in tissue used for calculating the TLD600 response (Eq. 9) were simulated at a distance of 25 cm to the CAX. The small deviation between the calculation and the measurement in the TLD600 response indicated a small variation of the neutron spectra along the MPAX. Hence, we think that it was justified to use the simulated neutron spectra to convert the TLD600 response to neutron dose equivalent independent of the off-axis distance of the measurement location.

The relative deviation between the measured and calculated TLD600 response was used as an indicator of how accurately the neutron spectra at a certain depth was estimated. Using Table VI, a deviation in the conversion factors (Eq. 11) of $(-6 \pm 11)\,\%$ (type B) was calculated by using the relative deviation of the TLD600 neutron response shown in Table VIII. With Gaussian error propagation, a final uncertainty of $\pm 20\,\%$ (type B) in the conversion coefficients (Eq. 11) was calculated by adding the uncertainty in $\overline{C}$. For every measurement, the uncertainty in neutron dose equivalent was calculated from the uncertainty in the conversion coefficient [($\pm 20\,\%$ (type B)] and the uncertainty in the measured TLD600 neutron signal. The uncertainty in the neutron signal was dependent of the photon contamination (see Eq. 8). However, mostly the TLD600 signal from the photon contamination was much lower compared to the signal from the neutron contribution such that the error induced by photon contamination could be neglected.

TABLE VIII. The local difference between the measured and the calculated TLD600 neutron response for different depths, distances to the CAX and gantry angles. The depth was calculated using a straight line connecting the X-ray producing target with the corresponding measurement location in the phantom. The TLD600 response was normalized to a measurement location indicated by "nor". For a gantry angel of 180 °, the treatment table was between the phantom and the neutron producing gantry head.

	Distance from CAX and gantry angle		
Depth parallel to CAX [cm]	15 cm, (0 °,180 °)	25 cm, 0 °	60 cm, 0 °
1	(10 %, 28 %)	5 %	4 %
2	-	3 %	-
3	-	1 %	-
4	nor 0 %	-	nor 0 %
5	-	nor 0 %	-
8	-	−2 %	-
10	(−18 %, −21 %)	-	−4 %
15	-	−4 %	-

The neutron dose equivalent in 0.1 cm water calculated with the simulated absolute neutron spectra was $(1.69 \pm 0.03)\,\frac{\text{mSv}}{100\,\text{MUs}}$ (type B) for a Clinac iX operated at 18 MV (closed jaws and MLCs). We measured $(1.71 \pm 0.34)\,\frac{\text{mSv}}{100\,\text{MUs}}$ (type B) neutron dose equivalent for the same set-up, linear accelerator, and beam energy. The photon contamination (head leakage) was determined as $(0.126 \pm 0.001)\,\frac{\text{mGy}}{100\,\text{MUs}}$ (type B). Hence, the simulated and measured surface neutron dose equivalents were in good agreement. For the TrueBeam operated at 15 MV, the measured neutron dose equivalent $[(0.687 \pm 0.137)\,\frac{\text{mSv}}{100\,\text{MUs}}$ (type B)] was 2.5 times lower compared to the Clinac iX operated at 18 MV. The photon contamination (head leakage) was determined as $(0.0783 \pm 0.0008)\,\frac{\text{mGy}}{100\,\text{MUs}}$ (type B). The task group report 158 [1] states a factor of two decrease in neutron dose of a Clinac iX between 18 MV and 15 MV. Most of the literature reports photoneutrons measured in air [1]. Neutron ambient dose equivalent overestimates the neutron dose equivalent anywhere in the patient [1]. Therefore, it was difficult to compare the measured neutron dose with the literature. Nevertheless, for a Clinac iX an ambient dose equivalent of around $2.0\,\frac{\text{mSv}}{100\,\text{MUs}}$ for 18 MV [1, 11, 12] and of around $1.0\,\frac{\text{mSv}}{100\,\text{MUs}}$ for 15 MV [1, 11] was reported. Maglieri et al. [13] measured an ambient dose equivalent of $0.60\,\frac{\text{mSv}}{100\,\text{MUs}}$ for a TrueBeam operated at 15 MV. Hence, the neutron dose close to the surface measured in this work was in good agreement with the neutron ambient dose equivalent reported in the literature.

Using only one coefficient to convert the TLD600 neutron signal to a neutron dose equivalent leads to a large overestimation of the neutron dose [31]. With the depth-dependent conversion coefficient, neutron signals from the literature can retrospectively be converted to neutron dose equivalents. Wiezorek et al. [9] measured the off-axis neutron signal in various depths for a Siemens Oncor Impression operated at 15 MV. They reported only fictive neutron signals measured with TLD600. At a depth of 0.5 cm in the phantom, they measured a fictive photon dose signal of $2.39\,\frac{\text{mGys}}{100\,\text{MUs}}$, which results in $(0.47 \pm 0.09)\,\frac{\text{mSv}}{100\,\text{MUs}}$ (type B) neutron dose equivalent by using the conversion coefficients in water presented in Table VI. For a Siemens linear accelerator operated at 15 MV, an ambient neutron dose equivalent of $0.52\,\frac{\text{mSv}}{100\,\text{MUs}}$ is reported in the literature [1].

ACKNOWLEDGMENT

The authors would like to express their sincere gratitude to the following people: Stephen F. Kry from MD Anderson Hospital in Texas for providing the simulated neutron spectra used in this work. Furthermore, Philipp Rouven from Paul Scherer Institute in Villigen for the support during the reference neutron fluence calibration and Regina Seiler from the Kantonsspital Luzern for the time spent during the Clinac iX neutron dose equivalent measurement.

This work was funded by the grant KFS-3249-08-2013 from the Swiss Cancer League.

DISCLOSURE

The authors have no relevant conflicts of interest to disclose.

[1] Kry SF, Bednarz B, Howell RM, Dauer L, Followill D, Klein E, Paganetti H, Wang B, Wuu CS, and Xu XG, "AAPM TG 158: measurement and calculation of doses outside the treated volume from external-beam radiation therapy," Medical Physics (2017).

[2] Diallo I, Haddy N, Adjadj E, Samand A, Quiniou E, Chavaudra J, Alziar I, Perret N, Guérin S, Lefkopoulos D, and Vathaire F, "Frequency distribution of second solid cancer locations in relation to the irradiated volume among 115 patients treated for childhood cancer," International Journal of Radiation Oncology • Biology • Physics **74**, 876–883 (2009).

[3] Stovall M, Blackwell CR, Cundiff J, Novack DH, Palta JR, Wagner LK, Webster EW, and Shalek RJ, "Fetal dose from radiotherapy with photon beams: report of AAPM radiation therapy committee Task Group No. 36," Medical Physics **22**, 63–82 (1995).

[4] Takam R, Bezak E, Marcu LG, and Yeoh E, "Out-of-field neutron and leakage photon exposures and the associated risk of second cancers in high-energy photon radiotherapy: current status," Radiation Research **176**, 508–520 (2011).

[5] Sung W, Park JM, Choi CH, Ha SW, and Ye SJ, "The effect of photon energy on intensity-modulated radiation therapy (IMRT) plans for prostate cancer," Radiation Oncology Journal **30**, 27–35 (2012).

[6] Kry SF, Salehpour M, Titt U, White RA, Stovall M, and Followill D, "Monte Carlo study shows no significant difference in second cancer risk between 6- and 18-MV intensity-modulated radiation therapy," Radiotherapy and Oncology **91**, 132–137 (2009).

[7] Ruben JD, Smith R, Lancaster CM, Haynes M, Jones P, and Panettieri V, "Constituent components of out-of-field scatter dose for 18-MV intensity-modulated radiation therapy versus 3-dimensional-conformal radiation therapy: a comparison with 6-MV and implications for carcinogenesis," International Journal of Radiation Oncology • Biology • Physics **90**, 645–653 (2014).

[8] Howell RM, Hertel NE, Wang Z, Hutchinson J, and Fullerton GD, "Calculation of effective dose from measurements of secondary neutron spectra and scattered photon dose from dynamic MLC IMRT for 6 MV, 15 MV, and 18 MV beam energies," Medical Physics **33**, 360–368 (2006).

[9] Wiezorek T, Voigt A, Metzger N, Georg D, Schwedas M, Salz H, and Wendt TG, "Experimental determination of peripheral doses for different IMRT techniques delivered by a Siemens linear accelerator," Strahlentherapie Und Onkologie: Organ Der Deutschen Röntgengesellschaft **184**, 73–79 (2008).

[10] Wiezorek T, Georg D, Schwedas M, Salz H, and Wendt TG, "Experimental determination of peripheral photon dose components for different IMRT techniques and linear accelerators," Zeitschrift für Medizinische Physik **19**, 120–128 (2009).

[11] Howell RM, Kry SF, Burgett E, Hertel NE, and Followill DS, "Secondary neutron spectra from modern Varian, Siemens, and Elekta linacs with multileaf collimators," Medical Physics **36**, 4027–4038 (2009).

[12] Maglieri R, Licea A, Evans M, Seuntjens J, and Kildea J, "Measuring neutron spectra in radiotherapy using the nested neutron spectrometer," Medical Physics **42**, 6162–6169 (2015).

[13] Maglieri R, Liang L, Evans M, Licea A, Dubeau J, Witharana S, DeBlois F, Seuntjens J, and Kildea J, "SU-F-BRE-11: Neutron measurements around the varian TrueBeam linac," Medical Physics **41**, 393–393 (2014).

[14] Murphy MJ, Balter J, Balter S, BenComo JA, Das IJ, Jiang SB, Ma CM, Olivera GH, Rodebaugh RF, Ruchala KJ, Shirato H, and Yin FF, "The management of imaging dose during image-guided radiotherapy: report of the AAPM Task Group 75," Medical Physics **34**, 4041–4063 (2007).

[15] Hauri P, Hälg RA, and Schneider U, "Technical Note: Comparison of peripheral patient dose from MR-guided Co-60 therapy and 6 MV linear accelerator IGRT," Medical Physics **44**, 3788–3793 (2017).

[16] Kry SF, Howell RM, Salehpour M, and Followill DS, "Neutron spectra and dose equivalents calculated in tissue for high-energy radiation therapy," Medical Physics **36**, 1244–1250 (2009).

[17] Hauri P, Hälg RA, Besserer J, and Schneider U, "A general model for stray dose calculation of static and intensity-modulated photon radiation," Medical Physics **43**, 1955–1968 (2016).

[18] Schneider U, Hälg RA, Hartmann M, Mack A, Storelli F, Joosten A, Möckli R, and Besserer J, "Accuracy of out-of-field dose calculation of tomotherapy and cyberknife treatment planning systems: a dosimetric study," Zeitschrift für Medizinische Physik **24**, 211–215 (2014).

[19] Howell RM, Scarboro SB, Kry SF, and Yaldo DZ, "Accuracy of out-of-field dose calculations by a commercial treatment planning system," Physics in Medicine & Biology **55**, 6999 (2010).

[20] Schneider U, Hälg RA, and Besserer J, "Concept for quantifying the dose from image guided radiotherapy," Radiation Oncology **10**, 188 (2015).

[21] Hälg RA, Besserer J, and Schneider U, "Systematic measurements of whole-body dose distributions for various treatment machines and delivery techniques in radiation therapy," Medical Physics **39**, 7662–7676 (2012).

[22] Hauri P and Schneider U, "Whole-body dose and energy measurements in radiotherapy by a combination of LiF:Mg,Cu,P and LiF:Mg,Ti," Zeitschrift für Medizinische Physik (2017).

[23] Hälg RA, Besserer J, and Schneider U, "Systematic measurements of whole-body imaging dose distributions in image-guided radiation therapy," Medical Physics **39**, 7650–7661 (2012).

[24] Davis SD, Ross CK, Mobit PN, Zwan LVd, Chase WJ, and Shortt KR, "The response of LiF thermoluminescence dosemeters to photon beams in the energy range from 30 kV X-rays to Co-60 gamma rays," Radiation Protection Dosimetry **106**, 33–43 (2003).

[25] Schwahofer A, Feist H, Georg H, Häring P, and Schlegel W, "Experimental determination of the photon-energy dependent dose-to-water response of TLD600 and TLD700 (LiF:Mg,Ti) thermoluminescence detectors," Zeitschrift für Medizinische Physik **27**, 13–20 (2017).

[26] Ruben JD, Lancaster CM, Jones P, and Smith RL, "A comparison of out-of-field dose and its constituent components for intensity-modulated radiation therapy versus conformal radiation therapy: implications for carcinogenesis," International Journal of Radiation Oncology • Biology • Physics **81**, 1458–1464 (2011).

[27] Horowitz YS and Shachar BB, "Thermoluminescent LiF:Cu,Mg,P for gamma ray dosimetry in mixed fast neutron-gamma radiation fields," Radiation Protection Dosimetry **23**, 401–404 (1988).

[28] "Report on the Task Group on Reference Man: ICRP Publication 23," (1975).

[29] Hälg RA, Besserer J, Boschung M, Mayer S, Lomax AJ, and Schneider U, "Measurements of the neutron dose equivalent for various radiation qualities, treatment machines and delivery techniques in radiation therapy," Physics in Medicine & Biology **59**, 2457 (2014).

[30] Chibani O and Ma CMC, "Photonuclear dose calculations for high-energy photon beams from Siemens and Varian linacs," Medical Physics **30**, 1990–2000 (2003).

[31] Nedaie HA, Darestani H, Banaee N, Shagholi N, Mohammadi K, Shahvar A, and Bayat E, "Neutron dose measurements of Varian and Elekta linacs by TLD600 and TLD700 dosimeters and comparison with MCNP calculations," Journal of Medical Physics / Association of Medical Physicists of India **39**, 10–17 (2014).

[32] IAEA, "Absorbed dose determination in external beam radiotherapy," (2001).

[33] Hauri P, Hälg RA, and Schneider U, "Technical note: No increase in effective dose from half compared to full rotation pelvis cone beam CT," Journal of Applied Clinical Medical Physics **18**, 364–368 (2017).

[34] Kry SF, Titt U, Pönisch F, Followill D, Vassiliev ON, Allen White R, Mohan R, and Salehpour M, "A Monte Carlo model for calculating out-of-field dose from a Varian 6 MV beam," Medical Physics **33**, 4405–4413 (2006).

[35] Scarboro SB, Followill DS, Howell RM, and Kry SF, "Variations in photon energy spectra of a 6 MV beam and their impact on TLD response," Medical Physics **38**, 2619–2628 (2011).

[36] Sánchez-Nieto B, El-far R, Irazola L, Romero-Expósito M, Lagares JI, Mateo JC, Terrón JA, and Doblado FS, "Analytical model for photon peripheral dose estimation in radiotherapy treatments," Biomedical Physics & Engineering Express **1**, 045205 (2015).

[37] Chofor N, Harder D, Willborn KC, and Poppe B, "Internal scatter, the unavoidable major component of the peripheral dose in photon-beam radiotherapy," Physics in Medicine and Biology **57**, 1733–1743 (2012).

[38] Chofor N, Harder D, Willborn K, Rühmann A, and Poppe B, "Low-energy photons in high-energy photon fields – Monte Carlo generated spectra and a new descriptive parameter," Zeitschrift für Medizinische Physik **21**, 183–197 (2011).

[39] Howell RM, Ferenci MS, Hertel NE, and Fullerton GD, "Investigation of secondary neutron dose for 18 MV dynamic MLC IMRT delivery," Medical Physics **32**, 786–793 (2005).

[40] Wrixon AD, "New ICRP recommendations," Journal of Radiological Protection **28**, 161 (2008).

[41] Kry SF, Followill D, White RA, Stovall M, Kuban DA, and Salehpour M, "Uncertainty of calculated risk estimates for secondary malignancies after radiotherapy," International Journal of Radiation Oncology • Biology • Physics **68**, 1265–1271 (2007).

[42] Palma D, Vollans E, James K, Nakano S, Moiseenko V, Shaffer R, McKenzie M, Morris J, and Otto K, "Volumetric-modulated arc therapy for delivery of prostate radiotherapy: comparison with intensity-modulated radiotherapy and three-dimensional-conformal radiotherapy," International Journal of Radiation Oncology • Biology • Physics **72**, 996–1001 (2008).

[43] Schneider U, Lomax A, Pemler P, Besserer J, Ross D, Lombriser N, and Kaser-Hotz B, "The impact of IMRT and proton radiotherapy on secondary cancer incidence," Strahlentherapie Und Onkologie: Organ Der Deutschen Röntgengesellschaft **182**, 647–652 (2006).

[44] Lonski P, Taylor ML, Franich RD, Harty P, and Kron T, "Assessment of leakage doses around the treatment heads of different linear accelerators," Radiation Protection Dosimetry **152**, 304–312 (2012).

[45] Kry SF, Salehpour M, Followill DS, Stovall M, Kuban DA, White RA, and Rosen II, "The calculated risk of fatal secondary malignancies from intensity-modulated radiation therapy," International Journal of Radiation Oncology • Biology • Physics **62**, 1195–1203 (2005).

[46] Kim S and Alaei P, "Implementation of full/half bowtie filter models in a commercial treatment planning system for kilovoltage cone-beam CT dose estimations," Journal of Applied Clinical Medical Physics **17**, 153–164 (2016).

[47] Kuzmin G, Lee C, Lee C, Pelletier C, and Jung J, "SU-F-T-114: A novel anatomically predictive extension model of computational human phantoms for dose reconstruction in retrospective epidemiological studies of second cancer risks in radiotherapy patients," Medical Physics **43**, 3487–3488 (2016).

[48] Tahmasebi Birgani MJ, Behrooz MA, Shahbazian H, and Shams A, "Determination of the attenuation coefficient for megavoltage photons in the water phantom," International Journal of Radiation Research **9**, 251–255 (2012).

[49] Bedogni R, Esposito A, Angelone M, and Chiti M, "Determination of the response to photons and thermal neutrons of new LiF based TL materials for radiation protection purposes," IEEE Transactions on Nuclear Science **53**, 1367–1370 (2006).

[50] "ISO 4037-1:1996 - X and gamma reference radiation for calibrating dosemeters and doserate meters and for determining their response as a function of photon energy – Part 1: Radiation characteristics and production methods," (1996).

[51] "ISO 4037-2:1997 - X and gamma reference radiation for calibrating dosemeters and doserate meters and for determining their response as a function of photon energy – Part 2: Dosimetry for radiation protection over the energy ranges from 8 keV to 1.3 MeV and 4 MeV to 9 MeV," (1997).

[52] "ISO 4037-3:1999 - X and gamma reference radiation for calibrating dosemeters and doserate meters and for determining their response as a function of photon energy – Part 3: Calibration of area and personal dosemeters and the measurement of their response as a function of energy and angle of incidence," (1999).

[53] IAEA, "Compendium of neutron spectra and detector responses for radiation protection purposes," (2001).

[54] Veinot KG and Hertel NE, "Response of Harshaw neutron thermoluminescence dosemeters in terms of the revised ICRP/ICRU recommendations," Radiation Protection Dosimetry **113**, 442–448 (2005).

[55] "National Nuclear Data Center," (2017).

[56] Siebert BRL and Schuhmacher H, "Quality factors, ambient and personal dose equivalent for neutrons, based on the new ICRU stopping power data for protons and alpha particles," Radiation Protection Dosimetry **58**, 177–183 (1995).

[57] Caswell RS, Coyne JJ, and Randolph ML, "Kerma factors for neutron energies below 30 MeV," Radiation Research **83**, 217–254 (1980).

[58] Hoedlmoser H, Boschung M, Meier K, Stadtmann H, Hranitzky C, Figel M, and Mayer S, "Photon contributions from the Cf-252 and Am-241–Be neutron sources at the PSI Calibration Laboratory," Radiation Measurements **47**, 567–570 (2012).

Appendix A

Comparison of peripheral patient dose from MR-guided ^{60}Co therapy and 6 MV linear accelerator IGRT

Pascal Hauri[1,2], Roger A. Hälg[1,2], and Uwe Schneider[1,2]

[1] Institute for Radiotherapy, Radiotherapie Hirslanden AG, Aarau, Switzerland

[2] Department of Physics, University of Zurich, Zurich, Switzerland

Parts of this appendix were used for the master thesis of the Master of Advanced Studies ETH in Medical Physics.

This chapter was adapted from the original article:

"Technical Note: Comparison of peripheral patient dose from MR-guided ^{60}Co therapy and 6 MV linear accelerator IGRT"

Published in:

Medical Physics 2017, **44(7)**, 3788-3793
doi:10.1002/mp.12293.

Purpose: The use of X-ray imaging in radiation therapy can give a substantial dose to the patient. A Cobalt machine combined with a magnetic resonance imaging (MRI) device was recently introduced to clinical work. One positive aspect of using non-ionizing imaging is the reduction of the patient exposure. The purpose of this study was to quantify the difference in out-of-field dose to the patient between the image guided radiation therapy (IGRT) treatment applied with a linear accelerator with cone beam CT (CBCT) equipment and a Cobalt machine combined with an MRI device.

Methods: The treatment of a rhabdomyosarcoma in the prostate was planned and irradiated using different modalities and radiation therapy machines. The whole-body dose was measured for a 3D-conformal radiation therapy (3DCRT), an intensity-modulated radiation therapy (IMRT), and a volumetric-modulated arc therapy plan applied with a conventional linear accelerator operated at 6 MV beam energy. Additionally, the dose of an IMRT plan applied with a ^{60}Co machine combined with an MRI device was measured. Furthermore, the dose of one CBCT scan using the linear accelerator's on-board imaging system was determined. The 3D dose measurements were performed in an anthropomorphic phantom containing 168 slots for thermoluminescence dosimeters (TLDs). A combination of LiF:Mg,Ti (TLD100) and LiF:Mg,Cu,P (TLD100H) was used to accurately determine the in- and out-of-field dose. The treatments were rescaled to different fractionation schemes (2 Gy, 3 Gy, and 5 Gy fraction dose) and the dose of one CBCT scan was additionally added to the treatment dose per fraction applied with the linear accelerator. The resulting absorbed doses per fraction of the two machines were compared.

Results: In the target region, all measured treatments presented the same magnitude of dose, while the CBCT dose was a factor of 100 smaller. Close to the planned target volume (PTV), the dose from the ^{60}Co machine was a factor of two higher compared with the 3DCRT + CBCT dose. Up to 45 cm from the PTV, the treatment applied with the ^{60}Co sources showed an increased out-of-field dose compared to the linear accelerator + CBCT IGRT treatments. Further away from the PTV in the region where leakage from the gantry head is dominating, the out-of-field dose of the Cobalt machine was smaller compared to the linear accelerator + CBCT.

Conclusion: The peripheral dose of the ^{60}Co machine combined with an MRI device is larger up to 45 cm from the PTV and further away, it is lower than the dose from a linear accelerator + CBCT treatment. The presented fractionation schemes had a marginal impact on the results.

Keywords: Dosimetry, IGRT, MRI, CBCT, Cobalt

I. INTRODUCTION

Combining magnetic resonance imaging (MRI) with radiotherapy devices is currently highly topical in the field of treating cancer [1–4]. The first commercially available MRI–guided radiotherapy system (MRIdian) was introduced by ViewRay [1]. The MRIdian system combines three ^{60}Co sources with a 0.3 T MRI device. One positive aspect of using non-ionizing image modalities is the reduction of the patient dose. A combination of a linear accelerator with an MRI device is not yet clinically available. One reason for this is that the magnetic field of the MRI device disturbs the acceleration of the electrons which produce the photon treatment field. A possible solution is to combine ^{60}Co sources with an MRI device because the magnetic field does not interfere with the radioactive decay.

The use of X-ray imaging modalities can give a substantial dose to the patient [5]. The choice of treatment technique and indication determines the image modality and therefore, the additional amount of dose to the patient. For patient positioning, the imaging dose is justified by the reduction of the margins around the target. A smaller planning target volume (PTV) will lead to a sparing of the organs at risk. Multiple studies of imaging [6–10] and therapeutic dose [11–13] were published. To our knowledge, this is the first attempt to compare the out-of-field dose of two treatment machines, one equipped with an ionizing and one with a non-ionizing imaging device.

With a conventional linear accelerator operated at 6 MV nominal beam energy, the whole-body dose of a 3D-conformal radiation therapy (3DCRT), an intensity-modulated radiation therapy (IMRT), and a volumetric-modulated arc therapy (VMAT) treatment of a rhabdomyosarcoma in the prostate was measured. Additionally, the dose of a full-trajectory cone beam CT (CBCT) was determined with the linear accelerator's on-board imaging system. Furthermore, the dose of an MRIdian IMRT plan for the same treatment intention was determined. The measurements were done in an anthropomorphic phantom containing 168 slots for thermoluminescence dosimeters (TLDs). With a combination of differently doped TLD chips [LiF:Mg,Ti (TLD100) and LiF:Mg,Cu,P(TLD100H)] an accurate dose determination was possible. The measured treatments were rescaled to different fractionation schemes (2 Gy, 3 Gy, and 5 Gy fraction dose). One CBCT dose per fraction was added to the rescaled treatment doses applied with the linear accelerator and compared to the MRIdian dose.

II. METHODS AND MATERIALS

All irradiations and detector readouts were performed by the same person to ensure the consistency of the measurements preformed for this work.

A. Therapy modalities

The radiotherapy modalities used in this work were a ^{60}Co machine combined with an MRI device and a conventional linear accelerator equipped with an on-board imaging system.

The ViewRay system has three ^{60}Co heads mounted on a ring gantry. Every head is equipped with an independent double focused multileaf collimator. A detailed description of the MRIdian system can be found in Mutic et al. [1]. The ViewRay IMRT plan was made and irradiated at Washington University in St. Louis, MO, where the system is in routine clinical use.

The TrueBeam linear accelerator (Varian Medical Systems, Palo Alto, CA) is equipped with an on-board imaging system which is capable of performing CBCT scans. The X-ray source was operated at $125\,\mathrm{kV_p}$, which resulted in a mean photon energy of 64 keV [14]. The irradiations of the 3DCRT, IMRT, and VMAT plans using the 6 MV nominal beam energy, as well as the CBCT measurements were done at Hirslanden Medical Center in Aarau, Switzerland.

B. Treatment intention, planning, and irradiation

The target volume of this study was a rhabdomyosarcoma in the prostate for an adolescent patient. The planning CT of an anthropomorphic phantom (Alderson-Rando, RSD Radiology Support Devices, Long Beach, CA) as well as the contouring of the target structures and organs were preformed at one hospital.

The treatment planning of the 3DCRT (four field box), IMRT (five fields with dynamic MLCs), and VMAT (one arc) plans was done using the Eclipse treatment planning system (TPS) (Varian Medical Systems, Palo Alto, CA). A detailed description of the plans can be found in Hälg et al. [11]. The MRIdian IMRT plan was made with the system's built-in treatment planning and delivery software. The treatment consisted of 16 IMRT fields with a beam on time of 154 s and was planned according to the same protocol as the 6 MV intensity-modulated plans [11]. The magnetic field was switched off virtually for the Monte Carlo (MC) simulation of the dose by the MRIdian TPS. The 3DCRT plan included a sequential boost and the intensity-modulated plans an integrated boost. The diameter of the pelvis CBCT was 46.5 cm with a transversal dimension from isocenter of ±8.75 cm. The CBCT protocol (version 2.5.28.0, half fan type, full trajectory, $125\,\mathrm{kV_p}$, 1080 mAs) was given by the vendor.

The four treatments and the CBCT were irradiated onto the Alderson phantom each time loaded with new TLDs. The phantom was positioned head first suppine. Each measurement location in and on the phantom was equipped with a TLD100H stacked on top of a TLD100 and were distributed in the Alderson phantom according to Hälg et al. [11].

C. TLD dose measurements

The absorbed dose of the various treatments and the CBCT were measured separately with a combination of TLD100 and TLD100H chips. The two TLD types show a different response with radiation energy [15, 16]. Between 1 MeV and 0.1 MeV, TLD100 show an over- and TLD100H an under-response. For the dose measurements, a TLD100H chip was put on top of a TLD100 chip. The doses measured by the TLD100 and TLD100H were evaluated by using single calibration factors determined with a 6 MV nominal beam energy irradiation. The energy correction factor was found by the ratio of the TLD100 divided by the TLD100H dose. A detailed description of the TLD dose and energy measurement is given by Hauri et al. [17].

D. Dose comparison

To compare the final dose for different treatment schemes, the measured treatment dose was rescaled to a fraction dose of 2 Gy, 3 Gy, and 5 Gy. One CBCT dose was added to the rescaled fraction dose of the treatments applied with the linear accelerator resulting in a total dose of 3DCRT + CBCT, IMRT + CBCT and VMAT + CBCT. In these scenarios, the 2 Gy fraction dose represents the worst case regarding additional dose to the patient. Hence, the patient is positioned and/or checked at each treatment day with a CBCT.

The comparison of the dose was preformed in three regions (A)-(C) which can be seen in Fig. 1. (A) contained the PTV with four TLD measurement points. (B) included the transversal Alderson slab located 5 cm from the isocenter. This corresponded to a distance of 1 cm from the PTV and contained 13 measurement locations. (C) was located between 7.5 cm to 82.5 cm from the isocenter with 151 measurement locations well distributed in the Alderson phantom [11].

The treatment and imaging doses were graphically compared along the medial patient axis (MPAX, see Fig. 1). Schneider et al. [18] showed that the dose on the MPAX is representative for the average dose in each Alderson slice. Hence, the MPAX dose is a good measure of the average dose per area resulting from a coplanar treatment or a full trajectory CBCT. Additionally, a 3D dose comparison of the various measurement locations in the Alderson phantom was performed.

To verify the TLD-measured treatment doses, the dose in the PTV region was compared to the TPS-calculated dose. Additionally, the TPS-simulated in- and out-of-field dose was compared to the measured dose for the MRIdian system.

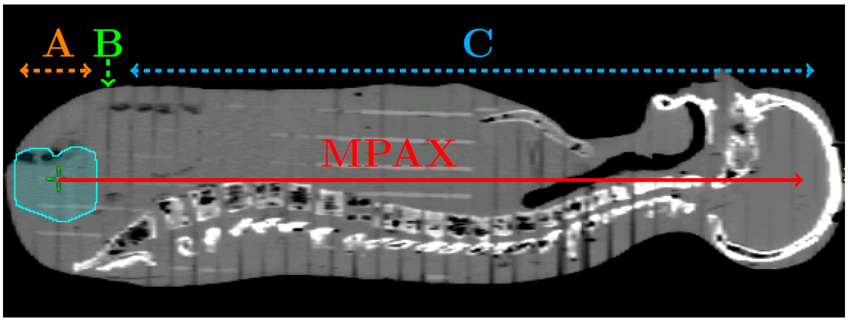

FIG. 1. CT of the Alderson phantom geometry. The phantom consist of 35 slabs in-between which the TLDs could be distributed. The solid arrow represent the medial patient axis (MPAX) origin from the isocenter. The dashed lines indicate the ranges along the MPAX in which the dose is discussed in this manuscript. The outline in the hip region indicate the PTV of the rhabdomyosarcoma. All measured treatments were co-planar irradiations.

III. RESULTS

The experimentally determined uncertainties at the level of two standard deviations (2σ), and thus the 95 % confidence interval for the TLD measurements of the treatments and the CBCT, was ±5 % and ±10 %, respectively. A detailed error analysis can be found in Hauri et al. [17].

The dose along the MPAX for the treatments (2 Gy fraction dose) and the CBCT can be seen in Fig. 2(a). The dose of the CBCT was consistently lower than all treatment doses. In region (A), all therapeutic doses were similar. In region (B), the MRIdian showed the highest out-of-field dose followed by the 3DCRT dose. The VMAT presented the smallest peripheral dose in region (B) out of all treatments. The MRIdian showed the highest out-of-field dose in region (C) up to around 50 cm from the isocenter. Far from the isocenter (> 50 cm), the dose of the conventional linear accelerator was higher. The TPS of the MRIdian simulated the dose in good agreement to the measured dose up to 18 cm from the PTV. Further away from the PTV, the TPS underestimated the out-of-field dose by more than 50 %. The underestimation of the stray dose by the MRIdian TPS increased linearly with increasing distance to the PTV.

In the Figs. 2(b)-(d), the dose of the VMAT + CBCT, IMRT + CBCT, MRIdian, and the CBCT relative to the 3DCRT + CBCT for different fraction doses is compared. It can be noticed that in region (B), the dose of the MRIdian treatment was more than two times higher than the 3DCRT + CBCT. In the region (C), the MRIdian dose increased to a maximum of three times the 3DCRT + CBCT dose. The maximum was located at 37.5 cm from the isocenter. From the differences between the Figs. 2(b)-(d), it can be concluded that the fraction scheme had a small impact on the dose difference between the TrueBeam treatment + CBCT and the MRIdian treatment.

In region (A), the CBCT dose was 100 times smaller than the 3DCRT treatment dose for a fractionation scheme of 2 Gy (Table I). In region (B), the CBCT doses rose up to 1/10 of the therapeutic dose. Further away from the isocenter, the out-of-field dose of the CBCT was on average 1/5 of the 3DCRT treatment. The maximum dose of the CBCT scan relative to the 3DCRT treatment dose was located near the surface of the phantom at a distance of 7.5 cm from the isocenter (3.3 cm from the PTV along the MPAX). At this distance, the 3DCRT treatment showed a 3.5 times higher dose at the center of the phantom than at the surface, while the CBCT dose was nearly homogeneous (±10 %) over the transversal dose plane. The maximum dose of the CBCT corresponded to 93 % of the 3DCRT treatment dose.

The comparison of the TrueBeam treatment + CBCT (2 Gy fraction scheme) with the MRIdian (Table I) indicated that the measured points in the PTV of the MRIdian treatment received $5 - 8$ % more dose. For all treatments, the measured dose in the PTV was between ±10 % of the prescribed dose. The TPS calculated dose in the PTV was compared to the TLD determined dose by evaluating the mean and 2σ. The discrepancies were $1.8\,\% \pm 2.2\,\%$, $2.2\,\% \pm 2.3\,\%$, $3.9\,\% \pm 2.7\,\%$ and $4.1\,\% \pm 6.7\,\%$ for the MRIdian, the 3DCRT, the IMRT, and the VMAT plan, respectively.

The VMAT + CBCT and the IMRT + CBCT showed on average more than a factor of three reduced dose in region (B) compared to MRIdian treatment. The absorbed dose of the 3DCRT + CBCT was two times less than the MRIdian dose in region (B).

In region (C), the median and average relative dose of the MRIdian were higher than the dose of the TrueBeam image guided radiation therapy (IGRT) treatments. The biggest difference was observed for the 3DCRT + CBCT irradiation. Out of all TrueBeam plans, the 3DCRT used the least amount of monitor units (MUs) to apply the treatment dose.

IV. DISCUSSION AND CONCLUSION

The therapeutic dose of three different linear accelerator treatment techniques (3DCRT, IMRT, and VMAT), the imaging dose of a CBCT, and the dose of a treatment applied with a ^{60}Co machine combined with an MRI device (MRIdian) were measured. The measurements were done with an anthropomorphic phantom containing 168 slots for TLDs. The treatments were rescaled to three different treatment schemes (2 Gy, 3 Gy, and 5 Gy fraction dose). To each rescaled linear accelerator

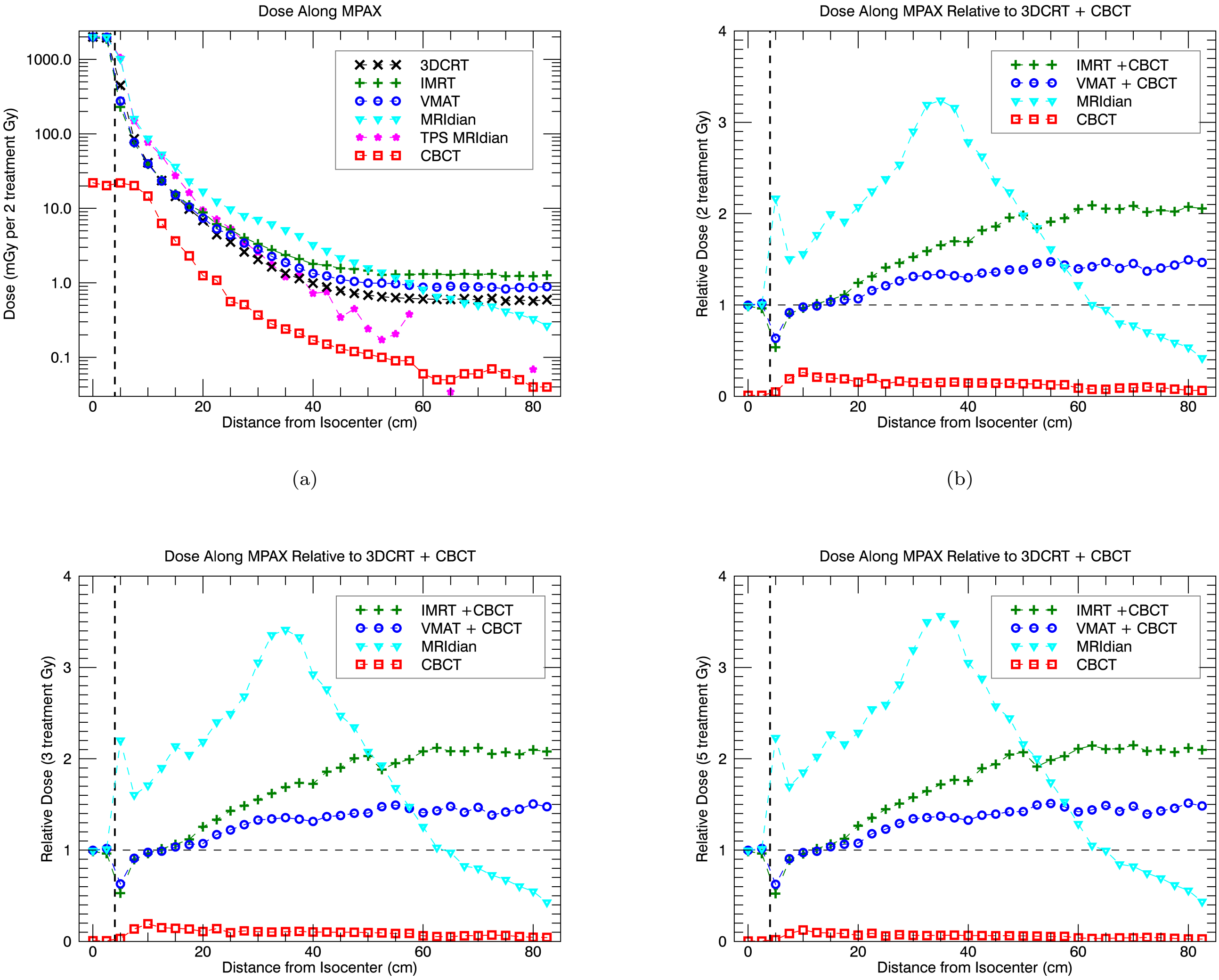

(a)

(b)

(c)

(d)

FIG. 2. (a) Measured dose along the MPAX for the CBCT and the single treatments per 2 Gy fraction dose. Additionally, the MRIdian TPS-simulated treatment dose. For a fraction dose of (b) 2 Gy, (c) 3 Gy, and (d) 5 Gy, the dose along the MPAX for the IMRT + CBCT, the VMAT + CBCT, the MRIdian, and the CBCT divided by the 3DCRT + CBCT dose. The vertical dashed line indicates the PTV edge.

TABLE I. The dose of the CBCT divided by the 3DCRT dose. Furthermore, the dose of the MRIdian divided by the 3DCRT + CBCT, IMRT + CBCT or VMAT + CBCT dose. All therapeutic doses are rescaled to a 2 Gy fraction dose. The regions (A)-(C) are defined in Fig. 1

	Region (A)		Region (B)		Region (C)	
	median; average	min; max	median; average	min; max	median; average	min; max
CBCT/3DCRT	0.01; 0.01	0.01; 0.01	0.05; 0.09	0.04; 0.24	0.20; 0.21	0.06; 0.93
MRIdian/(3DCRT+CBCT)	1.04; 1.05	0.99; 1.12	1.85; 1.84	0.91; 3.24	2.09; 2.07	0.42; 3.52
MRIdian/(IMRT+CBCT)	1.07; 1.08	1.00; 1.17	3.66; 3.63	2.49; 4.78	1.55; 1.33	0.21; 2.12
MRIdian/(VMAT+CBCT)	1.04; 1.06	0.99; 1.18	3.20; 3.02	1.15; 4.52	1.78; 1.60	0.29; 2.47

dose, the dose from one CBCT was added representing the dose of the different fraction schemes. The resulting therapeutic doses + CBCT were compared to the MRIdian dose. It can be concluded that the peripheral dose of the MRIdian is larger up to 45 cm from the PTV and further away, it is lower than a linear accelerator + CBCT treatment. Potential explanations for the deviations in the out-of-field dose could be the different gantry head designs and beam properties of the MRIdian compared to the TrueBeam. The presented fractionation schemes had a marginal impact on the results.

The TPS-calculated/-simulated and the measured treatment doses in the PTV were in satisfying agreement. Multiple studies showed that the MRIdian system can produce highly conformal IMRT treatments similar to linear accelerator IMRT plans [3, 4].

The MC-based TPS of the ViewRay machine underestimated the out-of-field dose far from the PTV. This is in line with the results of other TPS, which are underestimating the out-of-field dose [19, 20]. A detailed discussion of the accuracy of the Eclipse TPS in the specific case of the TrueBeam treatments presented in this study can be found in [21].

Close to the PTV and the surface of the phantom, the CBCT reached dose levels comparable to the out-of-field dose of a 2 Gy 3DCRT treatment fraction. For a 6 MV treatment, photons scattered in the phantom (patient scatter) are the dominant source of the out-of-field dose close to the field edge [21–26]. The magnitude of patient scatter increases towards the center of the phantom [21]. Hence, the therapeutic dose near the surface is reduced compared to the center, while the full trajectory CBCT dose is more or less uniform in a transversal slice [5, 18]. Further away from the field edge, the dose from a treatment machine is more homogeneously distributed in a transversal phantom slice, since the stray dose origins from external scatter contributions (mostly from the gantry head).

Far from the PTV, a clear difference in the out-of-field dose between the 3DCRT, the IMRT, and the VMAT treatment was noticed. Head leakage (photons produced in the target and leaking through the gantry head's shielding) is the dominating out-of-field dose contribution far from the isocenter [21, 22]. The magnitude of leakage is directly proportional to the applied MUs. Hence, the systematic difference of the stray dose can be explained by the difference in the MUs needed to apply the treatments. The MRIdian displayed a smaller out-of-field dose compared to the TrueBeam treatments in the region where leakage is dominant. As ^{60}Co machines exhibit excellent shielding for the retracted source, the leakage dose is in general much lower compared to linear accelerators.

Mesbahi et al. [12] estimated the organ doses from scattered photons for ^{60}Co, 6 MV, and 9 MV irradiations. In agreement with our findings, the ^{60}Co machine showed the highest out-of-field dose.

One limitation of this study is that only one treatment indication was used for the comparison of the different IGRT treatments. However, a rhabdomyosarcoma in the prostate was a relatively small PTV and the analyzed imaging dose of a pelvis CBCT was relatively large compared to the therapeutic dose. This study therefore represents a conservative imaging dose estimation.

ACKNOWLEDGMENT

The authors would like to express their sincere gratitude to Dr. Olga Green and Vivian Rodriguez from the Washington University School of Medicine for the treatment planning and the support of the MRIdian irradiation.

The traveling expenses and the transport cost for the Alderson phantom to the Washington University in St. Louis were covered by ViewRay.

This work was funded by the grant KFS-3249-08-2013 from the Swiss Cancer League.

DISCLOSURE

The authors have no relevant conflicts of interest to disclose.

[1] Mutic S and Dempsey JF, "The ViewRay system: magnetic resonance–guided and controlled radiotherapy," Seminars in Radiation Oncology Magnetic Resonance Imaging in Radiation Oncology, **24**, 196–199 (2014).

[2] Li HH, Rodriguez VL, Green OL, Hu Y, Kashani R, Wooten HO, Yang D, and Mutic S, "Patient-specific quality assurance for the delivery of Co-60 intensity modulated radiation therapy subject to a 0.35-T lateral magnetic field," International Journal of Radiation Oncology • Biology • Physics **91**, 65–72 (2015).

[3] Kishan AU, Cao M, Mikaeilian AG, Low DA, Kupelian PA, Steinberg ML, and Kamrava M, "Dosimetric feasibility of magnetic resonance imaging-guided tri-Cobalt-60 preoperative intensity modulated radiation therapy for soft tissue sarcomas of the extremity," Practical Radiation Oncology **5**, 350–356 (2015).

[4] Wooten HO, Green O, Yang M, DeWees T, Kashani R, Olsen J, Michalski J, Yang D, Tanderup K, Hu Y, Li HH, and Mutic S, "Quality of intensity-modulated radiation therapy treatment plans using a Co-60 magnetic resonance image guidance radiation therapy system," International Journal of Radiation Oncology • Biology • Physics **92**, 771–778 (2015).

[5] Murphy MJ, Balter J, Balter S, BenComo Jr. AJ, Das IJ, Jiang SB, Ma CM, Olivera GH, Rodebaugh RF, Ruchala KJ, Shirato H, and Yin FF, "The management of imaging dose during image-guided radiotherapy: report of the AAPM Task Group 75," Medical Physics **34**, 4041–4063 (2007).

[6] Hälg RA, Besserer J, and Schneider U, “Systematic measurements of whole-body imaging dose distributions in image-guided radiation therapy,” Medical Physics **39**, 7650–7661 (2012).

[7] Alaei P and Spezi E, “Imaging dose from cone beam computed tomography in radiation therapy,” Physica Medica **31**, 647–658 (2015).

[8] Ding GX, Duggan DM, and Coffey CW, “Accurate patient dosimetry of kilovoltage cone-beam CT in radiation therapy,” Medical Physics **35**, 1135–1144 (2008).

[9] Ding GX and Coffey CW, “Radiation dose from kilovoltage cone beam computed tomography in an image-guided radiotherapy procedure,” International Journal of Radiation Oncology • Biology • Physics **73**, 610–617 (2009).

[10] Walter C, Boda-Heggemann J, Wertz H, Loeb I, Rahn A, Lohr F, and Wenz F, “Phantom and in-vivo measurements of dose exposure by image-guided radiotherapy (IGRT): MV portal images vs. kV portal images vs. cone-beam CT,” Radiotherapy and Oncology: Journal of the European Society for Therapeutic Radiology and Oncology **85**, 418–423 (2007).

[11] Hälg RA, Besserer J, and Schneider U, “Systematic measurements of whole-body dose distributions for various treatment machines and delivery techniques in radiation therapy,” Medical Physics **39**, 7662–7676 (2012).

[12] Mesbahi A, Seyednejad F, and Gasemi-Jangjoo A, “Estimation of organs doses and radiation-induced secondary cancer risk from scattered photons for conventional radiation therapy of nasopharynx: a Monte Carlo study,” Japanese Journal of Radiology **28**, 398–403 (2010).

[13] Lamb J, Agazaryan N, Cao M, Low D, Thomas D, and Yang Y, “SU-E-J-198: Out-of-field dose and surface dose measurements of MRI-guided Cobalt-60 radiotherapy,” Medical Physics **42**, 3310–3311 (2015).

[14] Abuhaimed A, Martin CJ, Sankaralingam M, Gentle DJ, and McJury M, “An assessment of the efficiency of methods for measurement of the computed tomography dose index (CTDI) for cone beam (CBCT) dosimetry by Monte Carlo simulation,” Physics in Medicine and Biology **59**, 6307 (2014).

[15] Davis SD, Ross CK, Mobit PN, Van der Zwan L, Chase WJ, and Shortt KR, “The response of lif thermoluminescence dosemeters to photon beams in the energy range from 30 kV X-rays to Co-60 gamma rays,” Radiation Protection Dosimetry **106**, 33–43 (2003).

[16] Schwahofer A, Feist H, Georg H, Häring P, and Schlegel W, “Experimental determination of the photon-energy dependent dose-to-water response of TLD600 and TLD700 (LiF:Mg,Ti) thermoluminescence detectors,” Zeitschrift für Medizinische Physik **27**, 13–20 (2017).

[17] Hauri P and Schneider U, “Whole-body dose and energy measurements in radiotherapy by a combination of LiF:Mg,Cu,P and LiF:Mg,Ti,” Zeitschrift Für Medizinische Physik (2017).

[18] Schneider U, Hälg RA, and Besserer J, “Concept for quantifying the dose from image guided radiotherapy,” Radiation Oncology (London, England) **10**, 188 (2015).

[19] Howell RM, Scarboro SB, Kry SF, and Yaldo DZ, “Accuracy of out-of-field dose calculations by a commercial treatment planning system,” Physics in Medicine and Biology **55**, 6999 (2010).

[20] Schneider U, Hälg RA, Hartmann M, Mack A, Storelli F, Joosten A, Möckli R, and Besserer J, “Accuracy of out-of-field dose calculation of tomotherapy and cyberknife treatment planning systems: a dosimetric study,” Zeitschrift für Medizinische Physik **24**, 211–215 (2014).

[21] Hauri P, Hälg RA, Besserer J, and Schneider U, “A general model for stray dose calculation of static and intensity-modulated photon radiation,” Medical Physics **43**, 1955–1968 (2016).

[22] Ruben JD, Lancaster CM, Jones P, and Smith RL, “A comparison of out-of-field dose and its constituent components for intensity-modulated radiation therapy versus conformal radiation therapy: implications for carcinogenesis,” International Journal of Radiation Oncology • Biology • Physics **81**, 1458–1464 (2011).

[23] Chofor N, Harder D, Willborn KC, and Poppe B, “Internal scatter, the unavoidable major component of the peripheral dose in photon-beam radiotherapy,” Physics in Medicine and Biology **57**, 1733–1743 (2012).

[24] Lillicrap SC, Morgan HM, and Shakeshaft JT, “X-ray leakage during radiotherapy,” The British Journal of Radiology **73**, 793–794 (2000).

[25] Kase KR, Svensson GK, Wolbarst AB, and Marks MA, “Measurements of dose from secondary radiation outside a treatment field,” International Journal of Radiation Oncology • Biology • Physics **9**, 1177–1183 (1983).

[26] Jagetic LJ and Newhauser WD, “A simple and fast physics-based analytical method to calculate therapeutic and stray doses from external beam, megavoltage X-ray therapy,” Physics in Medicine and Biology **60**, 4753–4775 (2015).

Summary and outlook

This dissertation addressed the assessment of the individual whole-body dose for a radiotherapy patient. Analytical dose models were developed to calculate the photon and neutron dose of radiotherapy treatments. To verify the analytical models, photon and neutron out-of-field dose measurement methods were improved.

In chapter 1, a general model for stray dose calculation was developed to determine the whole-body dose of a patient receiving a 6 MV radiotherapy treatment applied with a conventional linear accelerator. The stray dose was calculated by the sum of the three major out-of-field dose components, which are patient scatter, collimator scatter, and head leakage. Patient scatter represented the main out-of-field dose contribution close to the treated volume and was mechanistically modeled. The development of a comprehensive model for patient scatter was important since close to the treated volume, the largest out-of-field dose gradients are found. For collimator scatter and head leakage, simple empirical models were introduced based on extended training measurements using an ionization chamber. The out-of-field dose of a treatment was calculated with the general stray dose model and fused with the TPS-calculated dose. The model was tested by comparing the fused dose to independent whole-body measurements of a treatment for a rhabdomyosarcoma in the prostate. The measurements were conducted with LiF TLDs distributed in an anthropomorphic phantom representing a real patient geometry. The results suggested that the model was accurate, fast and could be used for 3D-conformal and intensity-modulated treatments.

To more accurately verify the developed model of stray dose calculation from chapter 1, the peripheral photon dose measurement had to be improved. One of the main challenges to determine the dose was the changing photon energy spectrum outside the primary beam, which affected the response of the TLDs. In chapter 2, a novel dosimeter consisting of two differently doped LiF TLDs was introduced. This double-TLD unit automatically corrected for the response with radiation energy by determining the mean photon energy of a measurement. Compared to an ionization chamber, the double-TLD unit showed a mean and type A standard deviation of $-1\,\% \pm 1\,\%$ for in- and out-of-field dose measurements in a radiotherapy environment. The extended measurements of the mean energy for stray radiation in radiotherapy, brachytherapy, and X-ray imaging were in good agreement with MC simulations from the literature. Furthermore, the measurement of the mean energies for external beam radiotherapy revealed changing photon energies in the out-of-field region as a function of therapy modality and location in the patient. With the presented double-TLD unit, an accuracy in dose aimed for in radiotherapy was achieved. In chapter 3 and appendix A, applications of the double-TLD unit were presented.

The whole-body doses resulting from a half and full rotation CBCT were measured and compared in chapter 3. Within the measurement uncertainties, the determined effective doses of both CBCT protocols showed no significant difference at the 5 % level. By using the half rotation protocol, critical points in the patient could be spared. However, this came at the cost of depositing the spared radiation energy to other volumes. The full rotation CBCT dose was nearly homogeneously distributed between the left and the right side of the patient body. Using the double-TLD unit presented in chapter 2, the most accurate whole-body CBCT dose measurements up to date could be conducted. This led to a firm conclusion that the full instead of the half rotation CBCT protocol should be used in daily clinical work.

The investigation in appendix A revealed that, up to 50 cm from the isocenter, 6 MV linear accelerator treatments using CBCT for patient positioning showed a lower out-of-field dose than a Cobalt treatment using MRI for positioning. The treatment and CBCT whole-body doses were measured by the double-TLD unit introduced in chapter 2. A daily CBCT dose was added to the linear accelerator treatment doses per session. The resulting IGRT treatment doses applied with different modalities were compared to the $^{60}\mathbf{Co}$ treatment dose. Although the CBCT reached dose levels comparable to the scatter dose of the linear accelerator treatments, the $^{60}\mathbf{Co}$ treatment using non-ionizing radiation for positioning was inferior regarding patient protection.

In chapter 4, the whole-body dose equivalents resulting from 6 MV and 15 MV treatments, applied with different modalities, were compared. A simple neutron dose model was developed to calculate the neutron contribution resulting from photon radiotherapy. The model used the neutron dose equivalent close to the surface, which was measured in a simple geometry, to calculate the neutron dose resulting from a treatment. The calculation showed a mean and type A standard deviation of 20 % ± 30 % compared to independent whole-body neutron dose measurements. The neutron dose was measured by converting the detected neutron fluence to a dose equivalent using MC-simulated neutron spectra from the literature. The general model for photon stray dose calculation introduced in chapter 1, was improved and adapted for 15 MV. The calculated stray dose was in good agreement (±20 % type A standard deviation) with independent photon dose measurements. The 15 MV out-of-field dose measurements conducted with LiF TLDs were corrected for the response with photon radiation energy. For this, the mean photon energy for every point in the patient was calculated. A CBCT 3D dose distribution was added to the photon and neutron dose of a treatment session resulting in a whole-body dose equivalent. In contrast to previous findings reported in the literature, 15 MV IGRT treatments showed no increase in dose equivalent compared to 6 MV IGRT treatments. However, regarding patient protection, there were clear differences in the whole-body dose between different modalities favoring treatments with a short beam-on time.

The presented models for the whole-body dose equivalent calculation are generally applicable for any tumor location, patient geometry and photon producing linear accelerator. In a further project, it is planned to include the findings of this dissertation into the Varian Eclipse TPS to make the whole-body dose resulting from a radiotherapy treatment clinically available. The sizes of the planning CT is usually linked to the treatment volume. Hence, for an automatic integration of the whole-body dose calculation into the TPS, the patient CT has to be fused with a phantom CT containing the contours of critical tissue. However, such a feature is not jet clinically available.

The calculated whole-body dose can be used for treatment planning optimization. For this, appropriate cancer risk models have to be applied. A method to measure and calculate the mean energy of the single scatter contributions was introduced in chapter 2 and 4, respectively. With a decrease in the mean photon energy compared to the primary beam, an increase in the relative biological effectiveness (RBE) is expected. Hence, based on the findings of this dissertation, more accurate risk models should be developed including RBE.

At the moment, large scale epidemiological studies about second tumor induction are conducted. For these case control studies, the point dose at the location in the patient where the second primary tumor developed has to be retrospectively estimated. The estimation is based on extended measurements in simple geometries. This leads to a large error in the estimated point dose for multiple reasons. One of the reasons is the simple dose reconstruction methods the investigators use, another one is the to a great extend unknown patient geometry at the tumor induction site. The inclusion of the whole-body dose calculation into a TPS represents an investment in the future since the dose can be accurately calculated at any point in the patient.

Zusammenfassung

Die vorliegende Dissertation befasst sich mit der Ganzkörperdosis für Patienten der Strahlentherapie. Für die Berechnung der Photonen- und Neutronendosis wurden analytische Modelle entwickelt. Um die Modelle zu prüfen, wurden die bestehenden Dosismessmethoden für Photonen und Neutronen verbessert.

Ein allgemeines Modell zur Berechnung der Streudosis wurde in Kapitel 1 eingeführt. Das Modell berechnet die Ganzkörperdosis für Patienten und Patientinnen, die mit Radiotherapie behandelt wurden. Dazu wurde ein Linearbeschleuniger, betrieben bei einer nominellen Strahlenenergie von 6 MV, verwendet. Die Streudosis wurde durch die Addition der drei Hauptanteile ermittelt. Es handelt sich um Photonenstreuung im Patienten, Streuung an den Kollimatoren und Durchdringstrahlung des Beschleuningerkopfs. Der grösste Dosisanteil nahe am behandelten Therapievolumen wird durch die Photonenstreuung im Patienten verursacht. Dieser Streuanteil wurde mechanistisch modelliert, da nahe am Zielvolumen die grössten Dosisgradienten auftreten. Die Dosis, welche durch die Kollimatorstreuung und die Durchdringstrahlung des Beschleunigerkopfes verursacht wird, wurde mithilfe empirischer Modelle berechnet. Diese Modelle basierten auf umfangreichen Messungen mit einer Ionisationskammer. Die mit dem oben erwähnten allgemeinen Modell berechnete Streudosis wurde mit der Dosisverteilung des Planungssystems zusammengefügt. Dies resultierte in einer Ganzkörperdosis für eine Radiotherapiebehandlung. Die berechneten Dosen für die Bestrahlung eines Rhabdomyosarkomas in der Prostata wurden mit Ganzkörperdosismessungen verglichen. Diese Messungen wurden mithilfe von Thermolumineszenzdosimetern (TLDs) und einem anthropomorphen Phantom, welches den Patienten repräsentiert, durchgeführt. Die Evaluation zeigte, dass das Modell die Dosis von 3D-konformen und intensitäts-modulierten Bestrahlungen exakt und schnell berechnete.

Um das in Kapitel 1 vorgestellte allgemeine Modell zur Berechnung von Streudosen genauer prüfen zu können, musste eine Methode entwickelt werden, die die periphere Messung von Photonendosen verbessert. Die Veränderung des Photonenenergiespektrums ausserhalb des Zentralstrahls beeinflusst die TLD-Strahlungssensitivität. Ein neuer Dosimeter, der aus zwei verschieden dotierten TLD-Arten besteht, wurde in Kapitel 2 vorgestellt. Diese Doppel-TLD-Einheit misst die mittlere Energie eines Photonenspektrums und korrigiert damit automatisch für die Energieabhängigkeit der TLD-Strahlungssensitivität. Für die perkutane Strahlentherapie zeigte der vorgestellte Dosimeter eine mittlere und relative Typ A-Standardabweichung von $-1\,\% \pm 1\,\%$ verglichen mit einer Ionisationskammer. Die experimentell gemessenen mittleren Energien von Brachytherapiequellen, der Streustrahlung eines Linearbeschleunigers und der CBCT-Bildgebung deckten sich mit publizierten Simulationswerten. Die mittlere Streustrahlungsenergie der mit dem Alderson-Phantom gemessenen Therapiepläne veränderte sich mit zunehmendem Abstand vom Isozentrum. Mit der Doppel-TLD-Einheit wurde eine Genauigkeit in der Ganzkörperdosismessung erzielt, die in der Radiotherapie angestrebt wird. Zwei Anwendungen der Doppel-TLD-Einheit wurden in Kapitel 3 und Appendix A vorgestellt.

In Kapitel 3 wurden die Ganzkörperdosen eines Voll- und eines Halbrotations-CBCT gemessen

und anschliessend verglichen. Innerhalb der Messgenauigkeit konnte kein signifikanter Unterschied ($\alpha = 5\,\%$) zwischen den effektiven Dosen der beiden Protokolle festgestellt werden. Mit dem Halbrotations-CBCT konnten kritische Patientenbereiche geschont werden, wobei die dadurch vermiedene Strahlendosis in andere Volumen verteilt wurde. Die Dosis für das Vollrotations-CBCT war homogen verteilt in einem transversalen Schnitt des Phantoms. Die Ganzkörperdosen wurden mittels Doppel-TLD-Einheiten gemessen und stellen somit die genausten je gemessenen CBCT-Dosen dar. Aus Kapitel 3 folgt, dass für die Patientenpositionierung ein Vollrotations-CBCT einem Halbrotations-CBCT klar vorzuziehen ist.

Appendix A verglich die peripheren Dosen eines Linearbeschleunigers und CBCT mit denjenigen eines Kobaltgerätes. Der Linearbeschleuniger positionierte den Patienten mittels CBCT, das Kobaltgerät mithilfe eines MRI. Die Resultate zeigten, dass bis zu 50 cm vom Isozentrum die peripheren Dosen eines Linearbeschleunigers plus CBCT kleiner sind als diejenigen eines Kobaltgerätes. Die Ganzkörperdosen der verschiedenen Behandlungsarten und des CBCT wurden mit der Doppel-TLD-Einheit gemessen. Zur Ganzkörperdosis einer Behandlung mit dem Linearbeschleuniger wurde die CBCT-Dosis dazugerechnet. Die daraus resultierenden Dosen verschiedener Bestrahlungstechniken wurden mit der durch Kobaltbestrahlung verursachten Ganzkörperdosis verglichen. Obwohl die Dosis der CBCT-Bildgebung teilweise gleiche Werte erreichte wie die Streudosis des Linearbeschleunigers, war die Bestrahlung mit dem Kobalt-MRI-Gerät dosisintensiver für den Patienten.

In Kapitel 4 wurden die Ganzkörper-Äquivalentdosen, die aus verschiedenen 6 MV und 15 MV-Radiotherapiebehandlungen resultieren, verglichen. Ein simples Modell wurde entwickelt, um die aus der Photonenstrahlentherapie resultierende Neutronendosis zu berechnen. Die Neutronenäquivalentdosis wurde nahe der Oberfläche eines Plattenphantoms gemessen und mittels des Modelles in den Patienten projiziert. Diese Berechnung der Ganzkörper-Äquivalentdosis zeigte eine mittlere und Typ A-Standardabweichung von $20\,\% \pm 30\,\%$ verglichen mit unabhängigen Neutronendosismessungen. Für die Messung wurde die detektierte Neutronenfluenz mithilfe von MC-simulierten Neutronenspektren in Äquivalentdosis umgewandelt. Dabei wurden die MC-Simulationen der Literatur entnommen. Das in Kapitel 1 vorgestellte allgemeine Modell zur Berechnung von Streudosen wurde verbessert und gleichzeitig für 15 MV angepasst. Die berechnete Streudosis stimmte mit unabhängigen Photonendosismessungen überein ($\pm 20\,\%$ Typ A-Standardabweichung). Die Messungen ausserhalb des Zielvolumens mussten aufgrund der veränderte Strahlungssensitivität der TLDs korrigiert werden. Dazu wurde die mittlere Photonenenergie für jeden Punkt im Patienten berechnet und anschliessend in lokale TLD-Korrekturfaktoren umgewandelt. Um die Ganzkörper-Äquivalentdosis einer Strahlentherapiebehandlung zu bestimmen, wurde zur Photonen- und Neutronendosis eine CBCT-Dosis addiert. 15 MV-Radiotherapiebehandlungen zeigten keine höheren Äquivalentdosen als 6 MV-Behandlungen. Dies is im Widerspruch zu andere Studien, die eine erhöhte Äquivalentdosis für 15 MV-Radiotherapiebehandlungen dokumentieren. Für verschiedene Bestrahlungsarten wurden klare Unterschiede in der Ganzkörperdosis gefunden, wobei eine kürzere Bestrahlungszeit die periphere Dosis reduziert.

Acknowledgment

I would like to express my sincere gratitude to Prof. Dr. Uwe Schneider for supervising this doctoral thesis. I enjoyed doing this project with you so much. I am genuinely grateful for your trust and the encouragement while realizing our ideas. I have learned so much from you, thank you for the great time.

My sincere thanks also go to Dr. Roger Antoine Hälg. His extensive preparatory work has given me an easy entry in this project – especially by entrusting me with the Alderson phantom, which he himself spent so much time with. Thank you for always having an open ear for my questions and for improving my work.

Moreover, I would like to give my thanks to Beat Keller, Jürgen Besserer and Dr. Martin Staudacher for their support during the measurements. They always had the right answers and found practical solutions for the numerous problems I was faced with.

Thank you Dr. Matthias Hartmann, Felix Schordt and Fabrizio Storelli for the technical support during the process of my thesis.

I also wish to thank Prof. Dr. Jürg Osterwalder, Prof. Dr. Antony John Lomax and Prof. Dr. Ueli Straumann for being a part of my doctoral committee, the time spent during meetings and the at all times insightful feedback.

A big thank you goes to Philippe Hasler and Subas Scheibler, who I had the pleasure to supervise. It was fun to work with you on follow-up ideas resulting from my dissertation, which gave me a better understanding of my work.

Another thank you goes to PD Dr. Andreas Mack and my fellow students Fabiano Vasi and Marina Ernst for the lively discussions we had and which, eventually, made my work better.

Furthermore, I would like to thank the teams at the Radiotherapy Hirslanden in Aarau and Zurich for their support. Although we often did not share the same working hours, they always greeted me with a warm ”hello”.

A lot of people contributed to the work presented in this dissertation. I am grateful to everyone who helped realizing this work and is not mentioned personally.

For the financial support, I thank the Swiss Cancer League and Klinik Hirslanden.

From the bottom of my heart, I would like to thank Jasmin Gisiger for the countless hours spent proofreading my work. You are the love of my life.

I particularly wish to thank my mother for the unconditional support in all life situations. Thanks to you, I am able to follow my dreams. A huge thank you goes to the rest of my family, including their beautiful offspring. I am so grateful to have all of you in my life. Last but not least, I would like to thank my friends, you guys are my work-life balance.

Curriculum Vitæ

Family Name	Hauri
First Name	Pascal
Date of birth	13th February 1984
Nationality	Swiss
Education	
Since March 2014	Ph.D-Student, Physics University of Zurich, Zurich, Switzerland
September 2014 - March 2017	Master of Advanced Studies ETH in Medical Physics ETH Zurich, Zurich, Switzerland
September 2012 - February 2014	Master of Science in Physics ETH Zurich, Zurich, Switzerland • Master's thesis: *Adaptive Proton Radiotherapy*
September 2009 - August 2013	Bachelor of Science in Physics ETH Zurich, Zurich, Switzerland
August 2007 - August 2008	Passerelle Aargauische Maturitätsschule für Erwachsene, Aarau, Switzerland
August 2003 - July 2004	Technical Diploma Allgemeine Gewerbeschule Basel, Basel, Switzerland
Augusgt 2000 - July 2003	Apprenticeship as Chemical Laboratory Worker F. Hoffmann-La Roche, Basel, Switzerland